UNIVERSITÄT SIEGEN

KeJia Xing

Experiments and Simulation in Structural Health Monitoring Systems Using the E/M Impedance and Cross Transfer Function Methods

Schriftenreihe der Arbeitsgruppe
für Technische Mechanik
im Institut für Mechanik und Regelungs-
technik - Mechatronik

Herausgeber: Claus-Peter Fritzen

Band 9

Impressum
Prof. Dr.-Ing. Claus-Peter Fritzen
Arbeitsgruppe für Technische Mechanik
Institut für Mechanik und Regelungstechnik - Mechatronik
Universität Siegen
57068 Siegen
ISSN 2191-5601
URN urn:nbn:de:hbz:467-10055
Zugl.: Dissertation, Universität Siegen, 2015

EXPERIMENTS AND SIMULATION IN STRUCTURAL HEALTH MONITORING SYSTEMS USING THE E/M IMPEDANCE AND CROSS TRANSFER FUNCTION METHODS

DISSERTATION

zur Erlangung des Grades eines Doktors

der Ingenieurwissenschaften

vorgelegt von

MSc. KeJia Xing

Erstgutachter: Prof. Dr.-Ing. Claus-Peter Fritzen

Zweitgutachter: Prof. Dr. Alfredo Guemes

Universidad Politécnica de Madrid

Tag der mündlichen Prüfung

13. Nov. 2015

Preface

The following research was carried out as a research associate at the Institute of Mechanics and Control Engineering- Mechatronics of the Department of Mechanical Engineering at the University of Siegen.

I would like to thank Prof. Dr.-Ing. Claus-Peter Fritzen for his encouragement and support during the time that I worked in his group and to thank Prof. Alfredo Güemes as the second reviewer.

I also would like to thank Mr. Gerhard Dietrich and Dipl.-Ing. Wolfgang Richter for the tremendous support they gave me with all my experiments. Many thanks are also due to my former colleague, Dr.-Ing. Rolf T. Schulte for his cooperation and encouragement, and to my colleagues, Mrs. Gisela Thomas, Dr.-Ing. Philipp Köster, Dipl.-Ing. Martin Kübbeler, MSc. Inka Müller and MSc. Henning Jung who were always supportive.

I also wish to thank my father (ZiYan Xing) and my late mother (BinZhen Liu) for their unswerving support. And last but not least, I want to thank my family, Thorsten and Jonas who have put up with me during the trying time while I undertook this research project.

Siegen, in August. 2015 KeJia Xing

Table of Contents

Nomenclature

a_n	Weight factor
a_q	Coefficients of interpolation polynomial
A_g	Symmetry strain
A_i	*i*-th antisymmetric mode
C_p	Capacitor of piezoelectric element
$\boldsymbol{C}$	Damping matrix of structure
c	Velocity of wave propagation
c_p	Phase velocity
c_g	Group velocity
d_c	Damping coefficient
d_{kij}	Piezoelectric coupling
d_p	Piezoelectric strain coefficient
d	Distance between the piezoelectric elements in phased array
D_x	Array span in *x* direction
$D_{x,j}$	The distance between the *J* piezoelectric element and the *jth* piezoelectric element in *x* direction
D_y	Array span in *y* direction
$D_{y,n}$	The distance between the *Jth* piezoelectric element and the *(J+n)th* piezoelectric element in the *y* direction
D_j	Electrical displacement
$\boldsymbol{H_D}$	Matrix of transfer functions in the damaged state
E	Applied electric field
E_k	Electrical field
e_{31}	Piezoelectric coupling coefficient
e_{32}	Piezoelectric coupling coefficient
f	Frequency
$\boldsymbol{F}$	Matrix of force and moments
g	Frequency interval decided by the sample frequency during data transfer from time to frequency domain

h_p	Thickness of the piezoelectric element
$\boldsymbol{H}$	Matrix of transfer functions no phase delay in the undamaged state
$\boldsymbol{H_D}$	Matrix of transfer functions no phase delay in the damaged state
I	Current
$\boldsymbol{Im}$	Importance of eigenvalue $\boldsymbol{\Lambda_n}$
J	Number of piezoelectric elements in phased array
k	Wave number
$\boldsymbol{K}$	Stiffness matrix of structure
K_p	Static stiffness of the piezoelectric element
l_p	Length of the piezoelectric element
L	Coefficient in the Dolph-Chebyshev distribution
$\boldsymbol{M}$	Matrix of mass
M^{pzt}	Produced moments in the bonded PZT
m	Number of measurements
N^{pzt}	Produced forces in the bonded PZT
N	The number of piezoelectric elements in y direction in a 2-D array
$\boldsymbol{P}$	Matrix of principal components
$\boldsymbol{p}_j$	Eigenvectors of the covariance of $\boldsymbol{X}$
P_p	Piezoelectric polarization vector
P_{ref}	Matrix of principal components from the reference data
Q	Output charge of the piezoelectric element
$\boldsymbol{q}$	Vector of coefficient of polynomial degree
R	Resistance
R_{far}	Far-field definition, is the estimated distance between the estimated damage and the reference piezoelectric element in the array
R_{near}	Near-field definition, is the estimated distance between the estimated damage and the reference piezoelectric element in the array
R_p	Proportional limit stress
r_j	Distance between the estimated damage and reference piezoelectric element
S_{ij}	Mechanical strain
S_i	i-th Symmetric mode

$\boldsymbol{S}$	Phase delay matrix to implement beamforming
s	Interpolation polynomials
t	Time
$\boldsymbol{T}$	Matrix of transfer functions with phase delay in the undamaged state
$\boldsymbol{T_D}$	Matrix of transfer functions with phase delay in the damaged state
T_p	Stress exerted upon the piezoelectric element
T_{kl}	Mechanical stress
$\boldsymbol{T_R}$	Reduced matrix from $\boldsymbol{X}$ which is the matrix of the measured features
u_0	Displacement of each mode in the plane
u	Coefficient in the Dolph-Chebyshev distribution
V	Applied voltage of the circuit for measuring EMIs
$\boldsymbol{v}$	Applied voltage vector in the cross transfer method
V_{Out}	Output voltage of the circuit for measuring EMIs
$\boldsymbol{v_{Out}}$	Output voltage vector with phased delay in undamaged state in the cross transfer method
$\boldsymbol{v_{Out,D}}$	Output voltage vector with phased delay in damaged state in the cross transfer method
v_0	Displacement of each mode in the plane
v_p	Poisson's ratio of the piezoelectric element
w	Out of plane displacement of each mode
$\boldsymbol{w_m}$	Vector of weight factors in phased array
w_p	Width of the piezoelectric element
$\boldsymbol{X}$	Matrix consists of features for self-diagnosis
$\boldsymbol{X_{COV}}$	Covariance matrix of $\boldsymbol{X}$
x	Parameter of normal function in self-diagnosis investigation
Y	Electro-mechanical admittance
$\widehat{Y}_p^E$	Young's modulus of piezoelectric element
Z	Coupled electro-mechanical impedance
Z_s	Mechanical impedance of the structure
Z_p	Mechanical impedance of the piezoelectric element
$Z_{g,1}$	Coupled electro-mechanical impedance in undamaged state
$Z_{g,2}$	Coupled electro-mechanical impedance in damaged state

Greek Letters

ρ	Density of the piezoelectric element
ω	Angular frequency
ω_n	Resonant frequency
η	Mechanical loss factor of piezoelectric element
ε_{33}^{T}	Dielectric constant
ε_x	Normal strain at *x* direction
δ	Dielectric loss tangent
τ	Correlation coefficient
σ	Standard deviation
σ_{bw}	Bending fatigue strength
σ_x	Normal stress at *x* direction
λ	Wavelength
θ	Steering angle
φ	Phase unit
$\boldsymbol{\Lambda_j}$	Eigenvalue of the covariance matrix $\boldsymbol{X}$

Abbreviation

Adm	Admittance
BEM	Boundary Element Method
CC	Covariance Coefficient
CT	Cross Transfer
DMC	Direct Maintenance Costs
DM	Damage Metrics
DI	Damage Indicator
EMI	Electro-Mechanical Impedance
FDM	Finite Difference Method
FEM	Finite Element Method
GLL	Gauss-Lobatto-Legendre
Imag	Imaginary Part
MAPD	Mean Absolute Percent Deviation
NDE	Non-Destructive Evaluation

PCA	Principal Component Analysis
PSM	Pseudospectral Method
PZT	Lead-Zirconate-Titannate
PVDF	Polyvinylidene Fluoride
RMSD	Root Mean Square Deviation
SEM	Spectral Element Method
SHM	Structural Health Monitoring
SMD	Spring-Mass-Damping
TUL	Threshold Upper Line

Abstract

In the modern world, there is an ever increasing need within industry for low cost, reliable and efficient mechanical structures. Within most industries maintenance costs make up a significant proportion of overall expenditure and offer the greatest potential for cost-saving. There is an opportunity, for example, to reduce the Direct Maintenance Costs (DMC) in the aerospace industry and the maintenance costs of turbines and blades in the wind-power sector.

As an enabling technology, Structural Health Monitoring (SHM) assesses the state of mechanical structures in real time in order to prevent accidents or disasters during the structures' operational lifetime. According to basic principles, several methods in SHM techniques can be defined e.g. mechanical, electric, electro-mechanical and electro-magnetic methods.

The focus of this work is on the Electro-Mechanical Impedance method (EMI) and Cross Transfer Function method (CTF). In both these methods, the data evaluation is in the frequency domain, using active-sensing piezoelectric elements which are bonded to the detected structures. It should be noted that the EMI method has been particularly cost-effective in SHM and has been used successfully in aeronautics, space technology, the wind power industry, the pipeline industry and architecture.

In this work, the EMI method is further developed for three different fields of application: self-diagnosis of bonded piezoelectric elements, their sensing ability and their use for damage detection in fatigue experiments.

Self-diagnosis is used to monitor whether the bonded piezoelectric elements either used as actuators or as sensors can continue to measure or function properly in SHM. During this process, the effects of temperature changes is included in data processing analysis. When using principal components analysis, the original data is simplified so that the more important information can be identified and used for further data analysis.

In the investigation of the sensing ability of piezoelectric elements, it is shown how the damage positions and the different frequency ranges of the input signals influence the element measurements using EMI spectrum. EMI methodology is applied in both experimental and numerical methods. The Spectral Element Method (SEM) as numerical methodology is ap-

plied in combination with EMI. EMI spectra comparison, involving both experimental and SEM methodology, shows a fairly good correlation. This proves that SEM combined with EMI is an efficient and effective method of data evaluation in SHM. In the last part of the work, EMI methodology is used to monitor the start of the crack in a vibrating aluminium plate in a fatigue experiment. Here, both dynamic and static measurements are taken. After the data obtained has been evaluated, the fatigue crack that has been identified in the plate can undergo inspection.

Another focus of this work lies on a better localization of damage using phased array techniques. Such arrays consist of several piezoelectric elements arranged in a certain geometric way. By controlling the phase shift of the input signal between each piezoelectric element and the superposition of all outputs, a wave propagation with a desired direction is obtained, where the direction of propagation is determined by the phase shift. The proposed technique works in the frequency domain and is based on the Cross Transfer Function method which uses the transfer functions between different actuator-sensors permutations of the array. In the frequency domain, the phase shifts are implemented numerically after the experimental determination of the transfer functions using a computer algorithm. This can be seen as a big advantage of the Cross Transfer Function method which makes it more flexible and efficient. The results show that the damage indicators are especially large in those directions where the damage is located.

1 Introduction

1.1 Motivation & the Concept of Structural Health Monitoring

Safety, costs and performance issues and usage monitoring are important to industry. In order to prevent catastrophic failures of a structure early damage detection is essential. However, this can only be achieved by improving the diagnostic methods used for damage detection.

To reduce expenditure it is important to minimize down-time, reduce inspection and maintenance costs, and prolong the service life of the structures. Structural Health Monitoring (SHM) provides a means to significantly eliminate down-time inspection, minimize inspection complexity and provide accurate diagnostics.

The process of implementing a damage-identification strategy for the aerospace, civil and mechanical engineering industries is referred to as SHM. It involves the observation and assessment of a given system over time using periodically sampled measurements obtained from permanently installed sensors. The extraction of damage-sensitive features from these measurements and the statistical analysis of these features is then used to determine the current state of health of the system.

The following are examples of catastrophe incidents that could have been prevented:

- On 1. April, 2011 a commercial aircraft operated by Southwest Airlines suffered rapid depressurization at a height of 10485 meters, leading to an emergency landing. Fortunately, this incident caused only minor injuries to two of 123 passengers and crew on board. The depressurization occurred because a 1.83 metre hole suddenly appeared in the top of the fuselage. The subsequent investigation revealed evidence of fatigue in the aircraft's structure.
- On 1 August, 2007, the I-35W Mississippi River bridge suddenly collapsed during the evening rush hour, killing 13 people and injuring 145. This bridge, which had been opened in 1967, was a steel truss arch structure. Extraordinary weight and structural cracking contributed to the catastrophic failure.
- The Space Shuttle *Columbia* disintegrated during re-entry into the earth's atmosphere on 1 Feb, 2003, resulting in the death of all seven crew members. This disaster occurred as a result of damage sustained during launch just over two weeks earlier, when a large piece of foam insulation broke off from the external tank of the space shuttle

and struck its wing shortly. The damage caused by this impact was not detected at the time.

- A high-speed train accident in Eschede, Germany on 3. June, 1998, caused the deaths of 101 people. The accident was the result of fatigue cracks in one of the wheels. A post-accident investigation showed that an efficient structural health monitoring system could have prevented this disaster from occurring by providing on-line information which could have a alerted maintenance crews to the problem. An advanced system could even have identified the location and extent of the structural damage.

All the examples cited above highlight the need for SHM. Not surprisingly, the field of SHM has recently received attention not only from the academic community but also from industry. In fact, SHM has become an essential element of modern structural components and is especially important where critical high performance is required, such as in the wind power and aerospace industries. In [Ostachowicz, 2013], SHM of aircraft structures, vibration-based damage diagnosis and monitoring of external loads in wind power are introduced. The accessibility of the critical components concerned is limited using traditional Non-Destructive Evaluation (NDE).

The overall process of SHM can be demonstrated in Figure 1.1. The sensor outputs data (y_1, y_2,.. y_n) is collected and transmitted to a computer so that data processing can occur. Data can then be evaluated by various methods, e.g. the model-based methods, neural networks or pattern recognition which includes feature extraction, classification and statistical analysis, see Figure 1.1. Using these processes it is possible to determine the state of the structure under review.

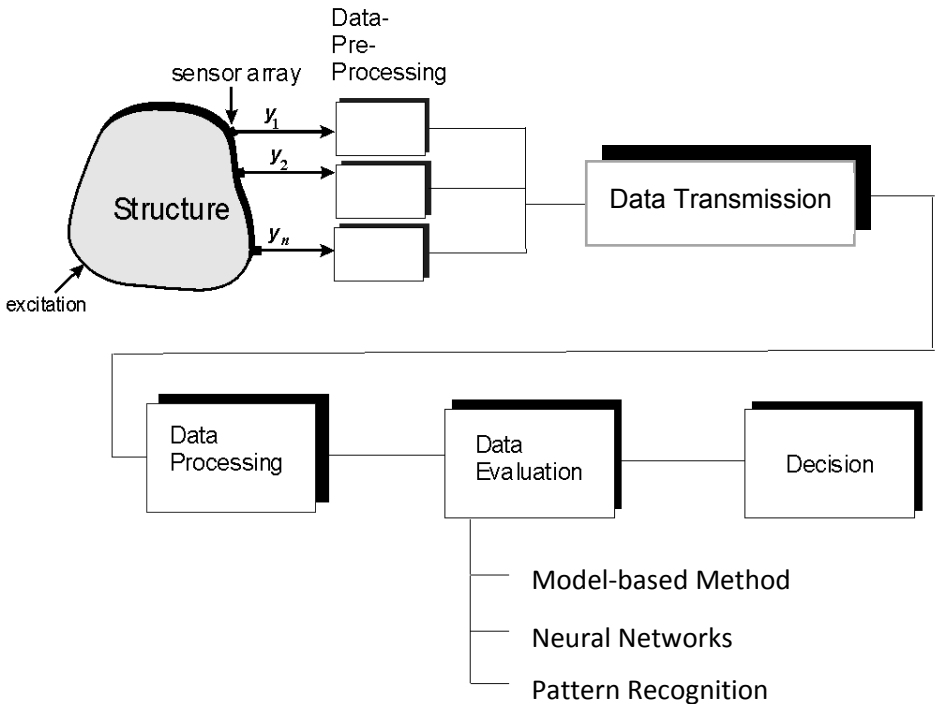

Figure 1.1 SHM Process Chain

To better understand the basic idea of the SHM system, several analogies between SHM and biomimetics have been mentioned in various articles. For example, a strong similarity exists between SHM and the bio-medical, bio-chemical activities of human beings. The structure which is bonded with various sensors in the SHM system is often compared to living skin, [Gandhi 1992]. Another often used analogy compares SHM to the human nervous system. Like the nervous system and brain in human beings, in the SHM system, after damage is detected by the sensors bonded to the structure, the control part of the SHM system can build a diagnosis and prognosis and decide if the current state of the structure is in a dangerous situation, [Beral 2003].

1.2 Classification of Structural Health Monitoring

Various SHM techniques can be defined in different ways. According to [Rytter 1993], SHM is divided into four levels, see Figure 1.2.

Level I detects if damage has occurred in any part of the structure. Level II tells where the damage is located. Level III shows the degree of the damage and Level IV gives the life prognosis , that is how long the structure in question can remain operational.

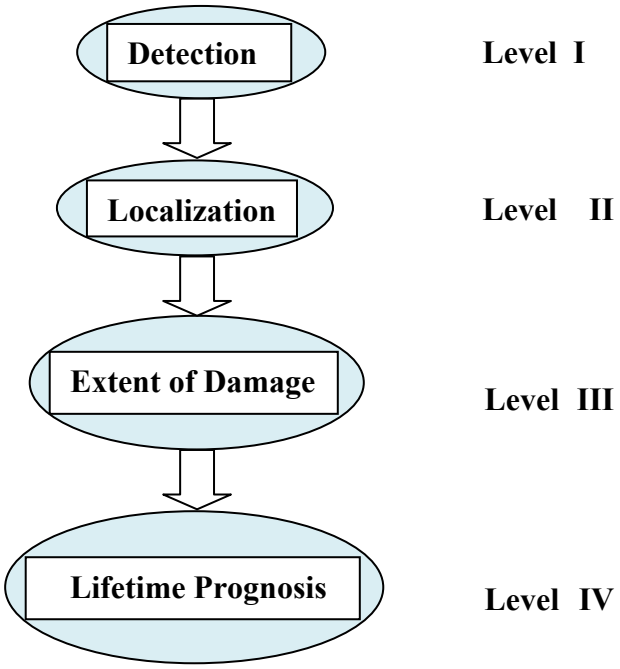

Figure 1.2 Classification of SHM

In 2004, [Worden 2004] added a fifth Level: the monitoring of damage type.

SHM techniques can also be classified as "global" and "local". The "global" method monitors the whole structure using a rough sensor network, normally operating at a lower frequency, which is less sensitive to minor damage. The wave length in a "global" method is approximately equal to the dimensions of the structure or component. Normally the frequency would be lower than *500Hz*. However, in certain applications like bridges or wind power, the frequency may be even lower than *50Hz*, [Bohle 2005], [Kraemer 2007]. It has been proved that the "global" method does not require special excitation signals. This is because the results are analysed by using the loads obtained from the structures while in operation or the excitation direct from environments, [Schulte 2010].

The "local" method monitors specific parts of the structure using a dense sensor network operating at higher frequencies, which is sensitive to minor damage. The impedance method developed by [Liang 1996] is an example of a "local" method. This method is further developed by using Electro-Mechanical Impedance (EMI) where a unique piezoelectric element works as both sensor and actuator. Recently, the EMI method has been applied successfully in several works, [Giurgiutiu 1997], [Park 2003], [Peairs 2006] and [Xing 2006].

"Local" methods can be defined as both "passive" and "active". "Passive monitoring" occurs where the structure is embedded with sensors that only monitor its evolution. For example, when using acoustic emission techniques any damage-progression in a loaded structure, or the occurrence of an impact, can be detected and localized by analysing the elastic waves measured by the sensors, [Staszewski 1999].

If the system is embedded with both sensors and actuators, the actuators generate the excitation signal in the structure and any feedback is then monitored by the sensors. This process is called "active monitoring". Using this type of system, the actuator and the sensor can be different or identical in nature.

There are two kinds of active system, the pitch-catch method and the pulse-echo method. In the pitch-catch method a pair of actuators and sensors is used in the SHM system. The actuators are used to transmit the energy from exciting signal into the structure while the sensors receive the reflected signal from the damage. In [Ihn 2008], the pitch-catch method, combined with an imaging method is used to find the location and extent of the damage. In the pulse-echo method, one actuator sends the exciting signal to the structure and receives the reflected signal from the damage. This means that an actuator/sensor is used concurrently in the system. It should be noted that this is also an important advantage of the EMI method. Figure 1.3 shows the principles of the pitch-catch and pulse-echo methods.

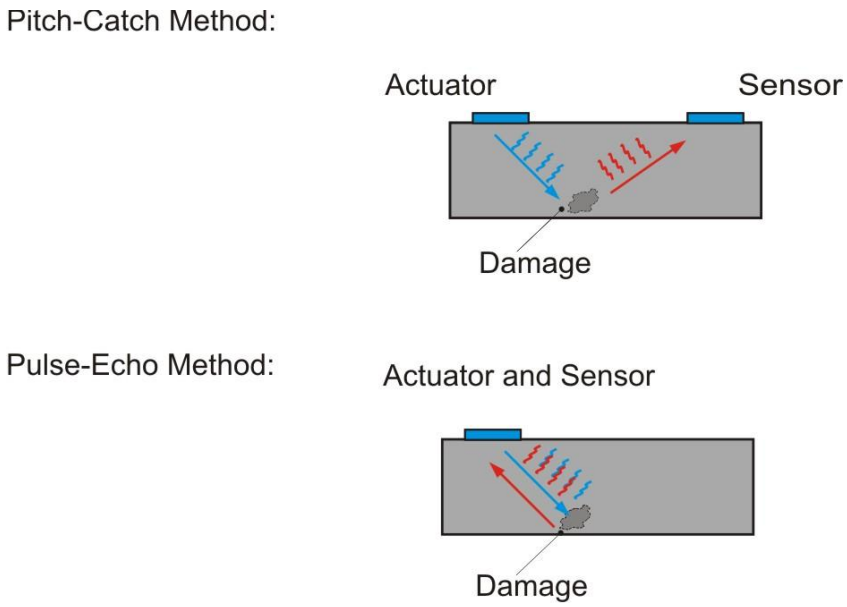

Figure 1.3 Two kinds of active systems

For damage detection in thin-walled structures, Guided Waves, which propagate in the wall of the structures, are primarily used. (Guided Waves can be subdivided into Lamb Waves and Shear-horizontal Waves. The Guided Wave interacts strongly with material inhomogeneity due to its propagation mechanisms, making it suitable for many types of Structural Health Monitoring. The Guided Wave, which is excited by a piezoelectric actuator in the SHM system, was first developed by Chang, [Chang 1995]. Further, an analysis algorithm, as a damage indicator based on the difference of output signals, is defined to determine changes in the structure, [Park and Chang 2003]. A comprehensive overview of the theory and application of Guided Waves is given in [Giurgiutiu 2007].

Where measurement is concerned, an SHM system can be based upon mechanical methods (using vibration measurements, static measurements and stress wave measurements), electric resistance, electro-mechanical and electro-magnetic methods. A classification of SHM methods is given in detail in [Balageas 2006], [Adams 2007] as well as [Giurgiutiu 2007].

1.3 Objectives and Outline of the Work

The objective of this work is to develop an economical and effective local method of SHM system. Two main methods are presented in this work, namely the Electro-mechanical Impedance (EMI) method, and the Cross Transfer Function method using a phased array in the frequency domain.

The idea of the EMI method is applied in both experiments and simulations. As an efficient simulation method, the spectral element method (SEM) is used here to set up models, on the basis of which some findings can be obtained prior to experiments. In the phased array method, SEM is used to simulate wave propagation in different phased array models. This results in an optimization of the experimental setup.

Chapter 1 is the introductory part of this work, in which the motivation and basic idea of SHM are introduced, explained and classified.

Chapter 2 outlines the fundamental principles that are applied in this work. In section 2.1, principles of piezoelectric elements, piezoelectric effects and the related formulations are further explained. In section 2.2, the background, basic concept and principle of the EMI method

are introduced. In addition, the applications of the EMI method in simulations and experiments are described in detail. In sections 2.3, 2.4 and 2.5, the fundamental concepts of wave propagation, phased arrays and Spectral Element Method are introduced respectively. The time-delay equations for both near- and far-field cases are given. Beamforming is implemented by superposition of the outputs of each piezoelectric element with a time-delay. In this way, wave propagation is reinforced in the desired direction.

In Chapter 3, the capability of group piezoelectric elements is investigated using the Cross Transfer Function method using the concept of the phased array. The superposition of the outputs of each piezoelectric element in the phased array are used in the cross-transfer functions in the frequency domain. By varying the steering vector in the cross-transfer functions, the direction of wave propagation is restricted to a chosen angle, which is the process of beamforming. To assess whether or not the beamforming effects are well-directed, the results of experiments are shown in polar plot. The results of simulations are shown using snapshots of wave propagation.

Chapter 4 describes the self-diagnosis of piezoelectric elements by using the EMI method. Before the SHM process is carried out the normal functioning of the piezoelectric elements bonded to the structure must be confirmed. This procedure is called self-diagnosis. Its basic principle is to analyse changes in the slope of the imaginary part of electro-mechanical admittance of bonded piezoelectric elements. If fractures, degradation or bonding defects occur in the elements, the slope will be shifted. It is by analysing these shifts that the properties of the elements can be monitored. As mentioned in 2.1, the properties of piezoelectric elements may be influenced significantly by environmental factors. To distinguish between changes in the element itself compared to those caused by the environmental factors, feature extraction and principal component analysis are used in data processing.

In Chapter 5, the investigation of the sensing area of one piezoelectric element using the EMI method is demonstrated. In this investigation both experimental and numerical methods are used to understand the sensing ability of one piezoelectric element bonded to the structure. The Spectral Element Method is applied as the numerical method in order to obtain the EMIs of the piezoelectric element. As mentioned in 2.5, the comparison between experimental and simulated results shows a good correlation. This validates the view that SEM is able to reflect the reality of the situation. Therefore, SEM appears to be a promising approach that can be

used to analyse the influence of parameters on EMI spectra, and it allows the efficient simulation of wave propagation phenomena. This method of simulation shows that the sensing ability is distinctly different in the whole structure with higher damping. For this reason, the experiments were also carried out into the effects of higher damping in the structure.

The damage indicators are analysed in three different cases, namely angles, distances and input signals. From the results of these experiments it has been established that the sensing area of a piezoelectric element is influenced strongly, not only by its position in the structure, but also by the input frequency range .

In Chapter 6, the EMI method is used in fatigue experiments to detect the initial cracks in a structure. The experiment in question uses an aluminium plate which is excited by a shaker to maintain vibration and the condition of the plate is monitored by the piezoelectric elements bonded to its surface. To avoid damage to the bonded elements during the vibration, the boundary of the bonding position for the piezoelectric elements is estimated by using deflection functions as well as the strain/stress curve of aluminium. In the experiments, damage indicators are calculated at different times by using both dynamic and static measurements.

It should be noted that there has been very limited research in which the EMI method is used in fatigue experiments of the kind described above. The research in this work will show, however, that fatigue cracks can be detected using the EMI method. The extent to which the EMI method can be used to map the dynamic changes of the growing cracks will also be presented.

Chapter 7 summarises the findings of this research and includes a discussion of the experimental methods used and the results obtained. The benefits and limitations of the methods in question are also discussed, as are the potential applications of the EMI method and areas of interest for further investigation.

2 Fundamentals

In the experiments described in this work, piezoelectric elements are used as sensors/actuators in the structures under review.

The basic principle of piezoelectric elements is introduced in 2.1. Because the electro-mechanical impedance method is one of the main approaches used in this work, the main idea and calculations of coupled E/M impedance in simulation and experiments are outlined in 2.2. The following sections introduce the principal theories.

2.1 Piezoelectric Elements

There are various types of transducers, such as piezoelectric, electro-dynamic, laser and capacitance transducers. Piezoelectric elements are the most widely used sensors for damage detection. The two commonly used materials are lead-zirconate-titanate mixed ceramics (PZT) and polyvinylidene fluoride (PVDF). The former is a ceramic and the latter a polymer-film. Piezoelectric ceramics are of particular importance for piezoelectric elements and are attractive for integrated damage detection in a structure because they exhibit simultaneous actuator and sensor behaviour, [Staszewski 2003]. PZT has number of advantages: it is light and small and has effective dynamic output performance. It can generate or receive signals with great efficiency over a wide frequency range and provide large signal amplitudes. Because of its high sensitivity, PZT, has been successfully used in SHM systems as a bonded piezoelectric element patch in the structure using the E/M impedance method.

The basic principle of the piezoelectric element used in the EMI method is the piezoelectric effect. The direct piezoelectric effect occurs when a small mechanical deformation of the piezoelectric element produces a proportional change in the electric polarization of that material, i.e. an electric charge appears on certain opposite faces of the piezoelectric material when it is mechanically loaded. This effect was discovered by the brothers Pierre and Jacques Curie and first published on 2. August 1880, [Gautschi 2002].

The relationship between piezoelectric polarization and stress can be formulated as follows:

$$P_p = d_p T_p \tag{2.1}$$

P_p is the piezoelectric polarization vector,

d_p is the piezoelectric strain coefficient,

T_p is the stress exerted upon the piezoelectric element, [Arnau 2004].

The existence of a converse piezoelectric effect was predicted by Lippmann in 1881, who mentioned that an electric field applied between the electrodes of a piezoelectric element would induce mechanical stress in it, [Gautschi 2002].

Figure 2.1 shows the direct piezoelectric effect and converse piezoelectric effect where F is the exerted force on piezoelectric element, P_p is the piezoelectric polarization and V_{Out} is the voltage because of P_p. E is the applied electric field in the converse piezoelectric effect, producing the strain and deformation of the piezoelectric element.

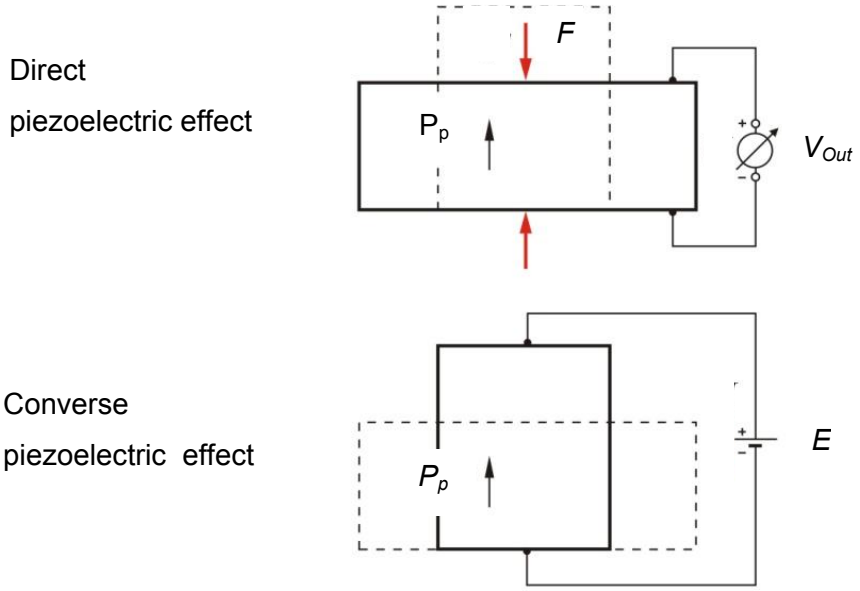

Figure 2.1 Direct and converse piezoelectric effects

The general constitutive equations of linear piezoelectric element behaviour describe a tensorial relationship between mechanical strain S_{ij} of an arbitrary surface, mechanical stress T_{kl}, the electrical field E_k and the electrical displacement D_j as described below:

$$S_{ij} = s^E_{ijkl} T_{kl} + d_{kij} E_k \tag{2.2}$$

$$D_j = d_{jkl} T_{kl} + \varepsilon^T_{jk} E_k \tag{2.3}$$

s^E_{ijkl} is the mechanical compliance of the material measured when E is equal to 0, ε^T_{jk} is the dielectric permittivity measured when T is equal to 0, and d_{jkl} is the piezoelectric coupling between the electrical and mechanical variables. In the equations above, i, j, k and l take the

values 1, 2, 3. In general, there are 21 independent mechanical compliances, 18 independent piezoelectric couplings and 6 independent dielectric permittivities, [IEEE 1987].

2.2 E/M Impedance Method (EMI Method)

Since the late 1970's, the Mechanical Impedance Method has been investigated in non-destructive tests to detect a variety of structural defects such as disbonds in adhesive joints and delaminations or voids in laminated structures. In 1978 Lange [Lange 1978] investigated the influence of the contact between a transducer and the structure using the Mechanical Impedance Method and how to improve inspection sensitivity. Using theoretical and experimental investigations, Cawley [Cawley 1984] described how defects influenced the mechanical impedance of a structure.

The work of Lange and Cawley proved that mechanical impedance can be used to identify structural changes. However, the sensitivity of the Mechanical Impedance Method is accurate only when the transducer is above the structure, the defect is thin and the inspected structure is relatively stiff. The Mechanical Impedance Method measures the mechanical quantities (force, velocity and acceleration) and calculates mechanical impedance indirectly. Moreover, it is almost impossible to implement real time monitoring in complex structures using the Mechanical Impedance Method. Because of the limitations of this method, the EMI method has been developed and successfully used in SHM.

Electro-mechanical (E/M) impedance is measured directly as an electrical quantity in the EMI method. Piezoelectric elements are commonly employed as sensors/actuators which are bonded to the structures under analysis. Each piezoelectric element actuates and senses the structure system concurrently. As a result of the inverse piezoelectric effect, input voltage excites the piezoelectric element and produces forces and moments. And since the element is bonded to the structure, these forces and moments are exerted onto only the local area of the structure. This causes the structure to deform and produces displacements in the local area. This deformation results in an electrical response that is measured as output voltages. In this way, the EMI spectrum can be obtained. In [Stepinski 2013], EMI is also introduced in Chapter 6. Due to the fact that the EMI is directly related to the mechanical impedance of the structure, changes in the EMI spectrum reflect the state of the structure in the local area.

2.2.1 Mathematical modelling of EMI

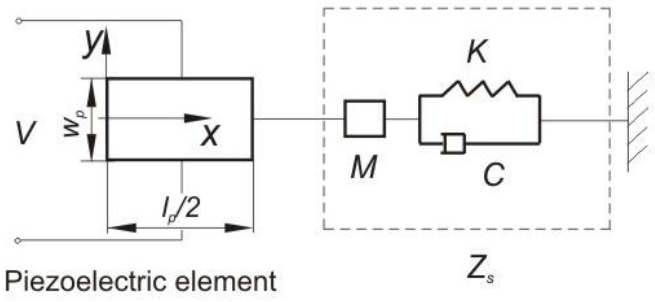

Figure 2.2 A schematic illustration of electro-mechanical coupling between a piezoelectric element and the structure, [Liang 1994]

In [Liang 1993a] and [Liang 1993b], the modelling of piezoelectric elements is based on the impedance method. In Liang's work, the dynamic response of the piezoelectric element is analysed to investigate the interactions between the piezoelectric element and the structure. Figure 2.2 shows this dynamic interaction, which is determined by coupling the constitutive relations between the piezoelectric element and the structure. In Figure 2.2, w_p is the width of the piezoelectric element, l_p is its length, V is the applied voltage to the piezoelectric element and Z_s is the mechanical impedance of the structure. By using the constitutive relationship of the piezoelectric element (see Eq. 2.2, the electric field E is applied in the y direction in Figure 2.2, $V=Eh_p$), the motion for a piezoelectric element vibrating in x direction, see Eq. 2.2 and Eq. 2.3 and the equilibrium and compatibility relationship between the structure and the piezoelectric element, the coupled electro-mechanical admittance (EMA, $Y=I/V$) is found as Eq. 2.4, [Liang 1994]:

$$Y = i\omega \frac{w_p l_p}{h_p} (\varepsilon_{33}^T (1 - i\delta) - d_{31}^2 \hat{Y}_p^E + \frac{Z_p}{Z_p + Z_s} d_{31}^2 \hat{Y}_p^E (\frac{\tan kl_p}{kl_p})) \tag{2.4}$$

In Eq.2.4, $d_{31}(N/ms^{-1})$ is the piezoelectric coupling constant, and w_p, l_p and h_p are the width, length and thickness of the piezoelectric element, i is $(-1)^{1/2}$, $\hat{Y}_p^E$ (N/m^2) is the complex Young's modulus of piezoelectric element at electric field $E=0$ v/m. ε_{33}^T is the dielectric constant at $T=0$ N/m^2, and δ is the dielectric loss factor, [Liang 1994].

$$\rho \frac{\partial^2 v}{\partial t^2} = \hat{Y}_p^E \frac{\partial^2 v}{\partial x^2} \tag{2.5}$$

ρ is the density of the piezoelectric element,

v is the displacement in the x direction,

$$k = \omega \sqrt{\frac{\rho}{\hat{Y}_p^E}} \tag{2.6}$$

Eq. 2.6 defines the wave number k, which is the wave number of the piezoelectric element.

$$Z_p = \frac{K_p(1+\eta i)}{\omega} i \tag{2.7}$$

In Eq. 2.7, Z_p is the mechanical impedance of piezoelectric element, K_p is the static stiffness, η is the mechanical loss factor of the piezoelectric element and ω is the excitation frequency.

$$Z_s = d_c + m\frac{\omega^2 - \omega_n^2}{\omega} i \tag{2.8}$$

In Eq.2.8, Z_s is the impedance of structure, d_c is the damping coefficient, m is the mass and ω_n is the resonant frequency of the spring-mass-damping (SMD) system which is determined by the spring constant and the mass of the system.

Because $tan(kl_p)/kl_p$ is close to one in most applications of intelligent materials, Eq. 2.4 may be further simplified as:

$$Y = i\omega \frac{w_p l_p}{h_p}(\varepsilon_{33}^T(1-i\delta) - \frac{Z_s}{Z_p + Z_s} d_{31}^2 \overline{Y}_p^E) \tag{2.9}$$

Eq. 2.9 is the simplified coupled electro-mechanical admittance (EMA) derived by Eq. 2.8. The first term is the capacitance admittance of a free piezoelectric element and the second term is the result of the electro-mechanical interaction of the element with the structure. From Eq. 2.9, it can be seen that Y is related by the mechanic impedance, geometrical constants, the electrical properties of the piezoelectric element, and the mechanical properties of the structure.

It was found that the imaginary part of Y increased sharply and reached its maximum at the system's resonant frequency. The sharp increase physically represented the increase of the reactive mechanical energy of the system, [Liang 1994]

In the work of [Sun 1995], Eq. 2.9 is rewritten as:

$$Y = \omega \frac{w_p l_p}{h_p}(\delta\varepsilon_{33}^T - y_r) + i\omega \frac{w_p l_p}{h_p}(\varepsilon_{33}^T + y_i) \tag{2.10}$$

in which y_r and y_i consist of the real and imaginary parts of Z_s or Z_p. Eq. 2.10 demonstrates that both the real and imaginary parts of Y are positive linear functions of frequency ω. How-

ever, the slope of the imaginary part, $\frac{w_p l_p}{h_p}\varepsilon_{33}^T$ is much larger than that of the real part, $\frac{w_p l_p}{h_p}\delta\varepsilon_{33}^T$, because δ is usually less than 1%. With the same extent of the change of y_r and y_i, the imaginary part of admittance fluctuates much less than the real part. This is illustrated in experiments carried out by Sun. Therefore, the real part of admittance was employed.

EMI is influenced by several factors, such as the frequency of the exciting signal, the properties of the structure, the adhesive properties, the temperature, and the integrity of the piezoelectric element itself. Generally, the real part of the EMI reflects the state or condition of the detected structure in a local area. The imaginary part of EMA can be used to confirm the integrity of the bonded piezoelectric element itself, [Zagrai 2001].

During the 1990s the EMI method contributed significantly in several areas of research. For example, [Zhou 1995] investigated actuator dynamic output, energy conversion efficiency and mechanical stress behaviour for two-dimensional structures using the coupled EMI model.

In the past 10 years, increasing attention has been paid to the EMI method which has been developed as a promising tool for real-time structural damage assessment. [Junior 2000] used the EMI method and artificial neural networks on the model of a steel bridge section and a space truss structure to estimate the location and severity of damage. EMI was also tested at NASA Glenn Research Center, which is the initial steps for the application of this technique to the aeronautical and space fields. In the test, the coupled EMI, see Eq. 2.11, is measured using a piezoelectric element and the real part is used in damage metrics, [Gyekenyesi 2005].

$$Z = 1/Y \tag{2.11}$$

In [Park 2003] and [Bhalla 2003], Eq. 2.9 provided the groundwork for using piezoelectric elements for EMI based SHM applications. This work shows that if the parameters (w_p, l_p, h_p, $\hat{Y}_p^E$, δ, ε_{33}^T,d_{31}) of the piezoelectric element are changed, they influence distinctly the imaginary part of the coupled admittance Y. Therefore, the state of a piezoelectric element (breakage or the degradations) can be identified by monitoring the imaginary part of Y. Experiments using the EMI method can also be found in papers published by [Ayres 1998], [Giurgiutiu 2000], [Park 2000], [Park 2001] and [Zagrai 2001], etc..

2.2.2 EMI method in experiments

Having explained the mathematic modelling of EMI, the following section describes how this idea is implemented in damage detection experiments. To set up the experiment, a PZT patch is used as the piezoelectric element and is bonded to the surface of the inspected structure. Devices such as a wave generator and an oscilloscope, are used to give the excitation signal to the PZT (at this point, PZT works as an actuator) and to receive the output signal from the same PZT (at this point, it works as a sensor). The circuit, see Figure 2.3, is used to connect the bonded PZT to the devices and to conduct the experiments. The bonded PZT is considered as a capacitor C_p. R is an auxiliary resister. V is the applied voltage, sweep is used as the input signal at a certain frequency range. Because of the converse piezoelectric effect, the bonded piezoelectric element is deformed causing stress to occur in the structure. Due to the direct piezoelectric effect (see section 2.1), the output voltage V_{Out} from the same PZT is produced and measured.

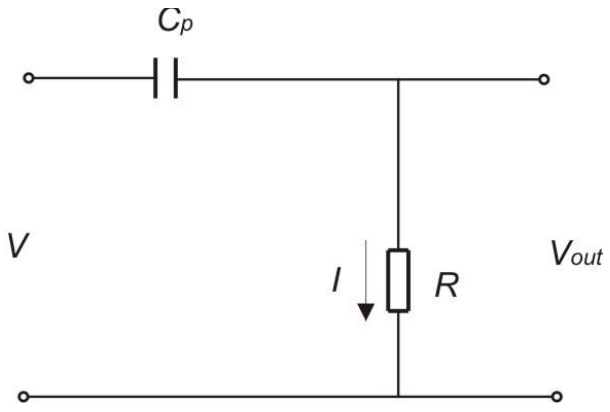

Figure 2.3 Circuit for measuring EMIs, [Peairs 2007]

In the experiment, the admittance Y is generated by taking the ratio (see Eq. 2.12 and Eq. 2.13)

$$I = \frac{V_{Out}}{R} \tag{2.12}$$

$$Y = \frac{I}{V} = \frac{V_{Out}}{RV} \tag{2.13}$$

where V_{Out} is output of resistance R, I is the current, V is the applied voltage.

Two simple examples using the EMI method are shown below. The first example describes an aluminium beam bonded with one PZT. The input sweep signal frequency is from 10kHz to 20kHz applied over a period of 10 seconds. The input and output signals in the time domain are shown in Figures 2.4 and 2.5. The horizontal coordinate is the data length determined by

the frequency range of the input signal, the signal's duration and the sample frequency of the oscilloscope. The vertical coordinate is the voltage. Figure 2.5 shows that the amplitudes of output voltages grow with the frequency of the input signals. This can be explained through the property of the capacitor, see Figure 2.3. The higher the frequency of V, the greater the current I through the capacitor C_p, the higher the output voltage, V_{Out}.

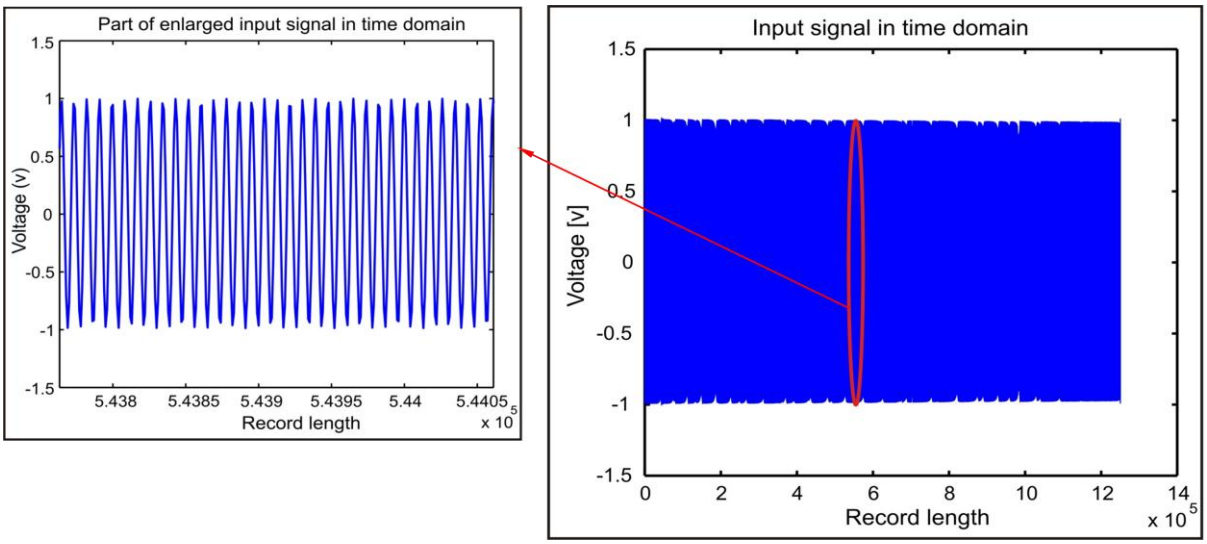

Figure 2.4 Input signal in time domain

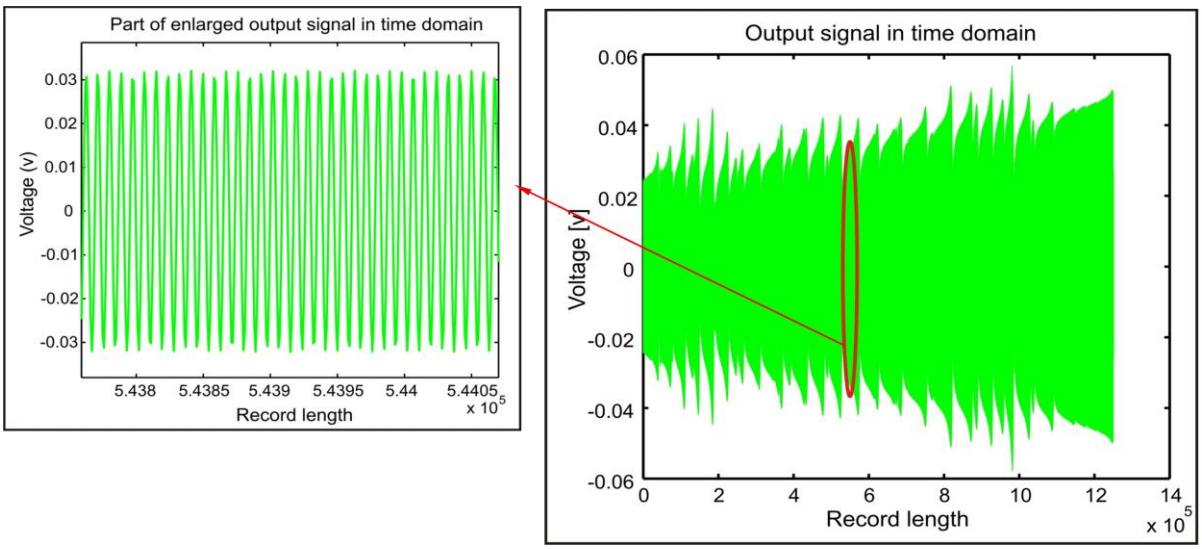

Figure 2.5 Corresponding output voltage in time domain

Using the EMI method, the measured data in the time domain is transferred to the frequency domain and the EMI spectra are obtained.

Figure 2.6 shows the spectrum of the real part of EMI. The blue line is the spectrum measured in an undamaged state. When damage appears in the aluminium beam, the spectrum shifts. The red line is the spectrum in a damaged state.

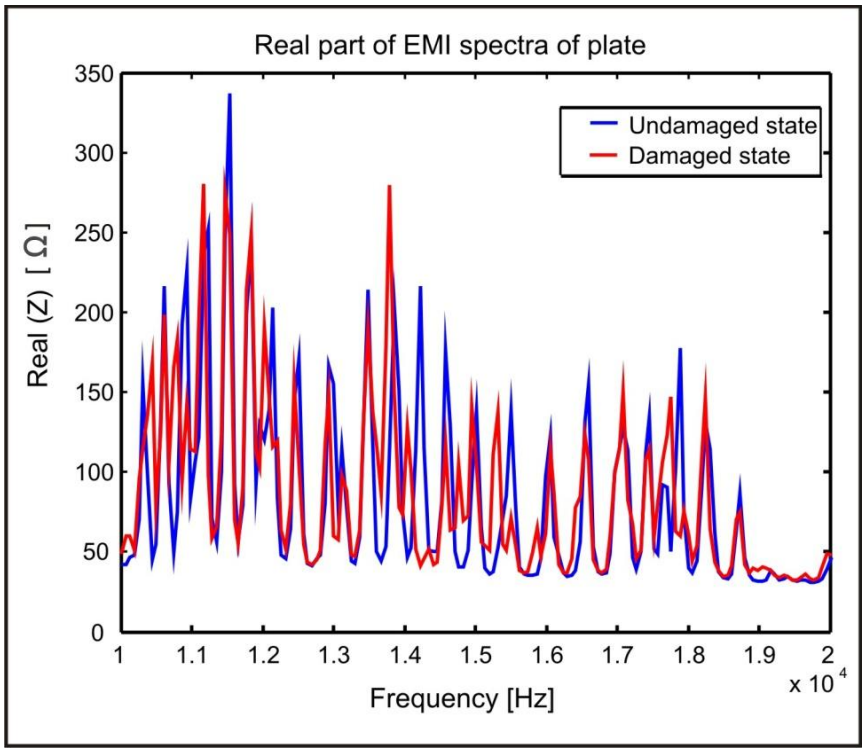

Figure 2.6 The spectra of EMI in the aluminium beam

The EMI method can be implemented not only in metal structures but also in carbon-fiber-reinforced-polymer (CFRP) which is being used increasingly in aircraft structures because of its impressive strength to weight and stiffness to weight ratios.

The second example shows a CFRP plate, 400mm long, 200mm wide and 2m thick, in which two PZT are bonded, see Figure 2.7. The same circuit is used as in Figure 2.3 for each PZT. The input signal frequency is from 20 to 30kHz in 10seconds. The input and output signals in the time domain are similar as in Figures 2.4 and 2.5. The data is measured in both undamaged and damaged states. In this case, the damage is produced by 10J impact on the carbon-fiber-reinforced polymer (CFRP) plate.

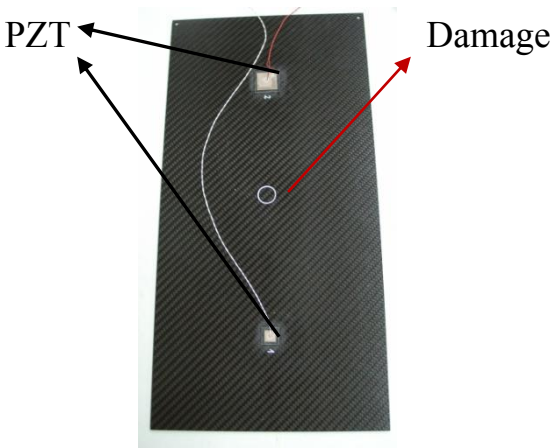

Figure 2.7 CFRP plate with two bonded PZTs

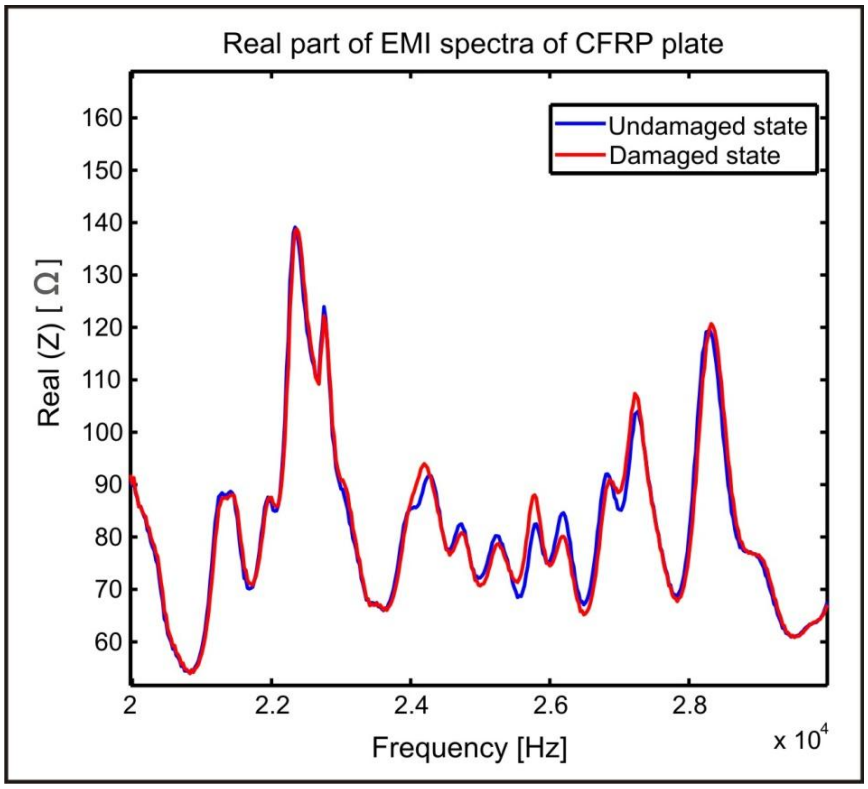

Figure 2.8 The spectra of EM impedance in the CFRP

Figure 2.8 shows the spectra of the real part of EMI in undamaged and damaged states between 20kHz and 30kHz. The blue line is the spectrum in the undamaged state. The red line is the spectrum after impact. It can be seen that the shift of the real part of EMI reflects the change of property in the CFRP plate.

2.2.3 Damage metrics and feature extraction

In SHM, in order to show the extent of the difference between the results in undamaged and damaged states, to define the distance between two states, Damage Metrics (DM) are used. There are several statistical methods to arrive at the damage metrics. For the EMI method, the following four algorithms have proved valid in other papers: Mean Absolute Percent Deviation (MAPD) [Park 2000], Root Mean Square Deviation (RMSD) method [Park 2000] and [Peairs 2006]. Covariance Coefficient (CC) and Difference Damage Metrics method are used in [Peairs 2002].

- *Difference Damage Metrics Method*

$$DM = \sum_{g=1}^{n} \left[\mathrm{Re}(Z_{g,1}) - \mathrm{Re}(Z_{g,2}) \right]^2 \tag{2.14}$$

Where *DM* represents the damage metrics,
$Z_{g,1}$ is the EMI in an undamaged state (also called the 'baseline'),
$Z_{g,2}$ is the EMI in a damaged state
g is the frequency interval which depends on the sample frequency during data transfer from time to frequency domain.

The two columns of EMI ($Z_{g,1}$ and $Z_{g,2}$) are compared at frequency interval *g*. At the end, Eq. 2.14 gives one quantity as a result to show the extent of the difference between the two EMI spectra.

- *Correlation Coefficient Method (CC Method)*

Correlation is a statistical technique which shows the relationship between a pair of variables. The value of the correlation is called the Correlation Coefficient. It ranges from –1.0 to +1.0. If the Correlation Coefficient is closer to +1 or –1, the two variables are related more closely. If the Correlation Coefficient is 0, it means there is no relationship between the pair of variables.

The Correlation Coefficient method is used to interpret and quantify the information from two different data columns (Z_1 and Z_2). The DM using the CC method is expressed as Eq. 2.15, [Peairs 2002]:

$$DM = (1-\tau)^2 \tag{2.15}$$

$$\tau = \frac{\mathrm{cov}(Z_1 Z_2)}{\sigma(Z_1)\sigma(Z_2)} \tag{2.16}$$

Z_1 and Z_2 are the EMI in undamaged and damaged states,
τ represents the correlation coefficient concerning Z_1, and Z_2,
cov(Z_1Z_2) means covariance matrix between Z_1 and Z_2, which can be calculated in Matlab
$\sigma(Z_1)$ and $\sigma(Z_2)$ are the standard deviations of Z_1 and Z_2.

- *Root Mean Square Deviation (RMSD) Method*

$$DM = \sqrt{\sum_{g=1}^{n} \frac{[\mathrm{Re}(Z_{g,1}) - \mathrm{Re}(Z_{g,2})]^2}{[\mathrm{Re}(Z_{g,1})]^2}} \tag{2.17}$$

$Z_{g,1}$ and $Z_{g,2}$ are the same as in Eq. 2.14.

For example, the real parts of EMI spectra in the experiment with CFRP (see Figure 2.7) are further utilized to establish *DM*. There are 10 instances of measurements in total (five in an undamaged state and five in a damaged states). The real parts of EMI from each measurement are compared with the same EMI measured in one undamaged state. Using the Difference Damage Metrics method (see Eq. 2.14) 10 DMs are obtained (see Figure 2.9). This indicates that there are major differences between the real part of EMI in a damaged state and an undamaged state. From this information it can be ascertained that there is damage in the structure. In each experiment, DMs are calculated using the three methods respectively, according to the best outcome. For each case the most effective method is chosen to be used.

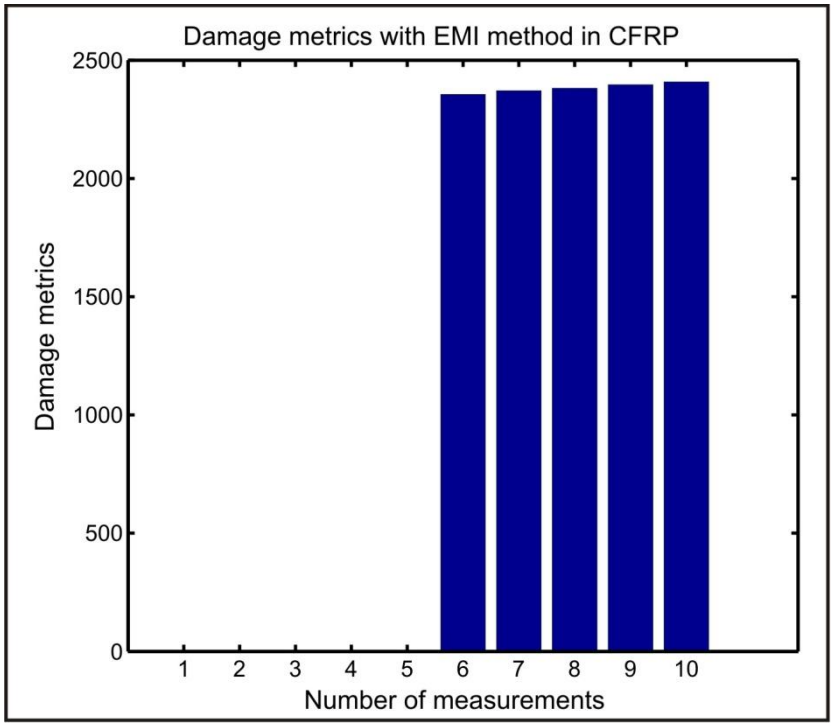

Figure 2.9 Damage metrics with E/M impedance method

The theory and experiments above have shown that the real part of the EMI spectrum can be directly affected by changes in the structure. The application of this technique has been proved in various engineering fields, e.g. aerospace structures, bolted joints, spot-welded joints and pipeline systems.

As mentioned in Chapter 1, data evaluation is a very important step in the SHM process. Pattern recognition is one of the most common methods used to provide a reasonable analysis of

a large amount of measured data. In pattern recognition, feature extraction is the approach to data dimension reduction.

In Chapter 4 the self-diagnosis of piezoelectric elements, feature extraction is used to transform E/M admittance data from high to lower dimensions, while still describing the important data information with sufficient accuracy. For dimension reduction, Principal Component Analysis (PCA) is the main technique used.

In this work, PCA is used to reduce the given data to a lower dimension by constructing a correlation matrix and computing the eigenvectors of the matrix. Following on from this, the eigenvectors corresponding to the largest eigenvalues are used to reconstruct data with a lower dimension. The principal components describe the reconstructed data with new variables which have two fundamental properties: 1) The relationship between two components is uncorrelated. 2) Each component is derived from an empirical orthogonal variable and maximal data variance, [Ehrendorfer 1987]. The complete process to reconstruct the matrix is described in the self-diagnosis experiment, see sections 4.1 and 4.2.

2.3 Wave Propagation

In the EMI and Cross Transfer Function methods, a bonded piezoelectric element excited by an input signal provides the energy of wave propagation in the structure. To get the exact output voltage of a piezoelectric element using a numerical method, the velocity, direction and mode of wave propagation and the relationship between wave propagation and the structure have to be considered. Therefore, an extensive knowledge of wave propagation is required.

In the wave theory of solid media, the particles of the media are infinitesimally small mass elements. Vibrations from these elements can radiate in all directions. Depending upon the direction of the vibration of the particles and the direction of wave propagation, two types of wave can be generated, longitudinal and transversal.

In a longitudinal wave, the vibration of the particles occur in the same direction as wave propagation. A one-dimensional longitudinal wave is like the vibration occurring in a simple spring. The particles of the spring simply oscillate back and forth. The displacement of each particle is parallel to the velocity of the vibration. In a transverse wave, particles move perpendicular to the direction of the wave propagation. For example, waves in water involve a

combination of both longitudinal and transverse motions. Usually, the velocity of the longitudinal wave is larger than that of the transverse wave. Propagating waves are additionally scattered (or reflected) and absorbed by different material boundaries. As a result, the amplitude of propagating waves is attenuated. When a wave passes between different media, the velocity of the propagation changes. Additionally, various mode conversions can occur. For damage detection in an SHM system, ultrasonic testing utilises wave attenuation, reflection and refraction, [Staszewski 2003].

In this work, aluminium is mainly used as material of the structure under investigation. Therefore, the properties of wave propagation in isotropic solid media is described in the following theory. Eq. 2.18 and Eq. 2.19 are basic equations of wave propagation.

$$c = \lambda f \tag{2.18}$$

$$k = \frac{\omega}{c} = \frac{2\pi f}{f\lambda} = \frac{2\pi}{\lambda} \tag{2.19}$$

where λ is wavelength, f is the wave frequency, c is the velocity of wave propagation and k is the wave number. c depends on the coupling among the particles of the media. If the coupling is stiffer, wave propagation is faster. The wave number k indicates how many wavelengths per 2π of unit distance. ω is the circular frequency. In wave propagation, phase velocity c_p and group velocity c_g have to be distinguished for dispersive waves. They are defined by Eq. 2.20 and Eq. 2.21.

The phase velocity is the rate at which the phase of the wave propagates, see Eq. 2.18

$$c_p = \frac{\lambda}{T} = \frac{\omega}{k} \tag{2.20}$$

The velocity at which the overall shape of the wave's amplitudes occurs is the group velocity,

$$c_g = \frac{\partial\omega}{\partial k} \tag{2.21}$$

ω and k are mentioned in Eq.2.19.

As it can be seen in Eq. 2.20, if ω is directly proportional to k, then the group velocity is exactly equal to the phase velocity. c_g is the speed of energy transport in the system. Figure 2.10 explains group velocity and phase velocity with the same wave in a state of constant phase between time t_0 and t_1, [Schulte 2010]. The red point at the zero-crossing has shifted exactly one mean wavelength to the right. However, the wave group has moved only a small dis-

placement, as illustrated by the blue arrow at the maximum of the envelope in Figure 2.10. The dotted unfilled arrow in the blow diagram of Figure 2.10 corresponds to the position of the filled gray arrow in the figure above ($t=t_0$). For the purposes of damage detection in SHM, group velocity can be used as the signal velocity, at which energy is transported through the solid media.

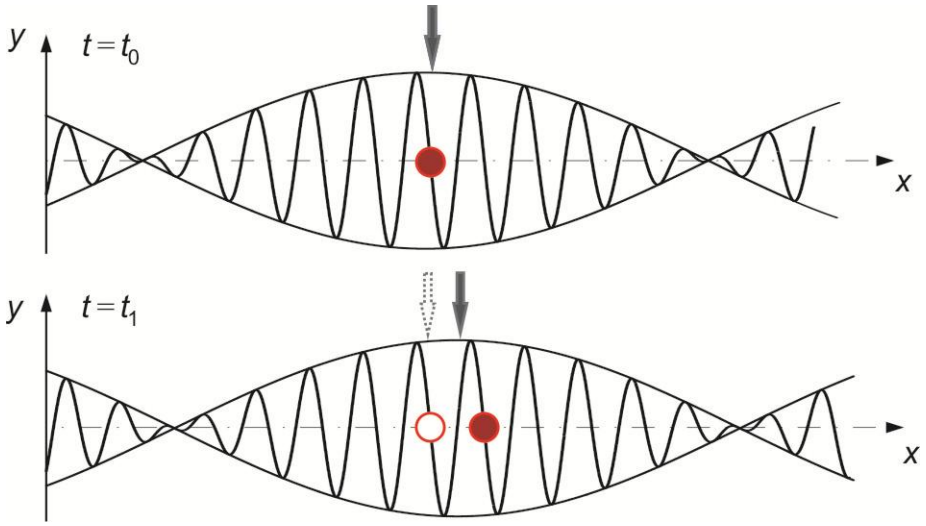

Figure 2.10 The difference between phase velocity and group velocity

As mentioned previously, after the solid media is excited by an input signal, both longitudinal and transversal waves occur. The waves propagating at interfacial or free surfaces could be reflected partially as well as converted partially into other types of waves, for example, longitudinal waves could be converted into transversal waves.

After a certain distance, longitudinal and vertical shear waves result in different wave packets, which are known as "guided waves". This is due to the superposition of the initial waves. The exact wave shape depends on the thickness of the solid media, the input signal and the angle of incident. This kind of wave is called a Lamb wave.

In 1917, the English mathematician Horace Lamb published his class analysis and description of the characteristics of waves propagation in plates, [Lamb 1917]. Essentially, Lamb waves can exhibit two waveforms, one in a symmetric mode S_i, the other in an antisymmetric mode A_i. When i is equal to 0, S_0 and A_0 are zero-order modes. These waves exist at all frequencies and in most cases, carry more energy than the higher-order modes. The velocity of the A_0 mode is lower than that of the S_0 mode and it leads to a smaller wavelength, which means it is more sensitive to small changes in the structure. For this reason, the A_0 mode is chosen in this study. As the frequency increases, the number of wave modes also increases. The higher-

order wave modes appear in addition to the zero-order modes. The frequency of each mode is decided by *i*, the wave velocity and the thickness of the plate.

Figure 2.11 shows the shapes of the first three modes of the symmetric (S_0, S_1 and S_2) and antisymmetric (A_0, A_1 and A_2) Lamb wave modes in a plate, h is the thickness of the plate, [Schulte 2010].

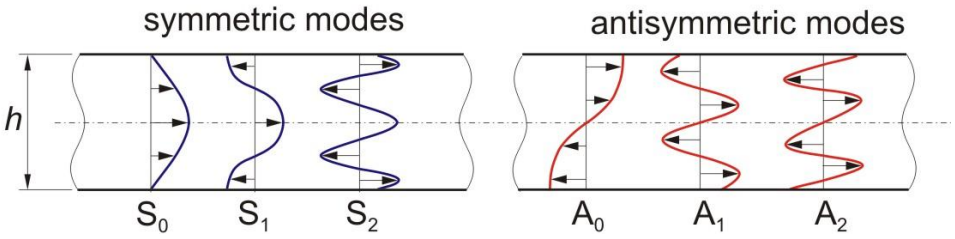

Figure 2.11 Symmetric and antisymmetric Lamb wave modes

Since the 1990s, the understanding and application of Lamb waves has progressed greatly in the field of nondestructive testing. Today, the analysis of Lamb wave propagation provides a very useful support to the successful SHM system. The simulation of Lamb waves propagation is used to set up and optimize the experimental system. In this work, Lamb wave modes are used in a numerical method to indicate the wave propagation in the aluminium plate bonded with piezoelectric elements.

2.4 Spectral Element Method (SEM)

There are a variety of numerical methods used for the modelling of wave propagation, such as the Pseudo-spectral Method (PSM), the Finite Difference Method (FDM), the Finite Element Method (FEM) and the Boundary Element Method (BEM). They are also called model-based methods. Among all these methods, the Finite Element Method (FEM) and the Spectral Element Method (SEM) are often used in SHM.

Figure 2.12 indicates the relationship between element nodes using three different numerical methods, namely, the Global Pseudo-spectral Method, the Finite Element Method and the Spectral Element Method respectively. The red points are the element nodes, and the black nodes illustrate the displacements. The first diagram explains the global pseudo-spectral method. It can be seen that displacement of each node is related to many other nodes, which makes the calculation complicated and inefficient. The second diagram shows the finite ele-

ment method, which shows that the displacement of each node is directly related to a few nodes only. The third diagram indicates the spectral element method, showing that each nodal displacement is related to multiple nodes with a reasonable small number. The Spectral Element Method combines the accuracy of the Global Pseudo-spectral Method with the flexibility of the Finite Element Method, but is much more efficient.

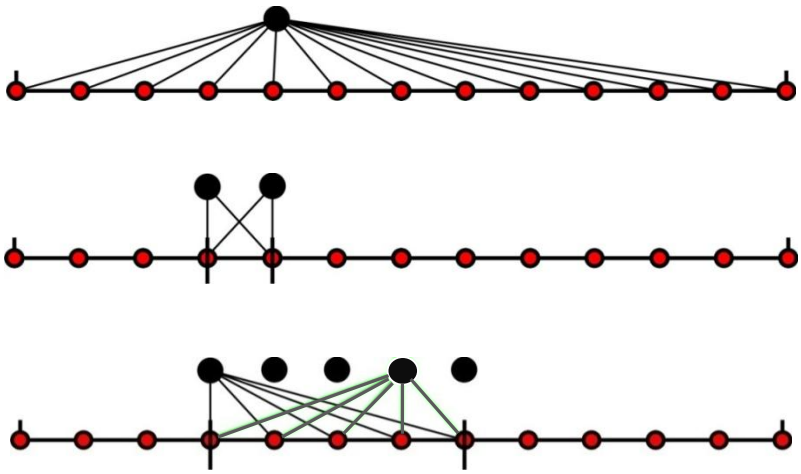

Figure 2.12 Global pseudo-spectral method, finite element method and spectral element method

Because of the high frequency excitation that occurs when applying the EMI method, a very dense finite element mesh is required for accurate simulation of wave propagation, hence, the SEM is chosen as model-based method. SEM was first proposed as a promising method, by [Patera 1984]. Kudela presented the results of the simulation of the propagation of transverse elastic waves in a composite plate with SEM, [Kudela 2007]. In [Schulte 2009], the formulation of a plane shell spectral element and the model of the E/M coupling of piezoelectric elements are given in detail. Comparisons of EMI spectra in both experiments and simulation are also shown.

SEM is used to simulate wave propagation in the aluminium plate with one bonded piezoelectric element and with a group of bonded piezoelectric elements in Chapter 3 and Chapter 5. Furthermore, in Chapter 5, the EMI spectra is calculated with SEM, by which the parameters of the aluminium plate influencing the EMI are investigated.

In this work, the formulation of a plane shell spectral element is used. The Gauss-Lobatto-Legendre (GLL) spectral element discretization is used and the spectral shell element is based on Mindlin's theory for plates.

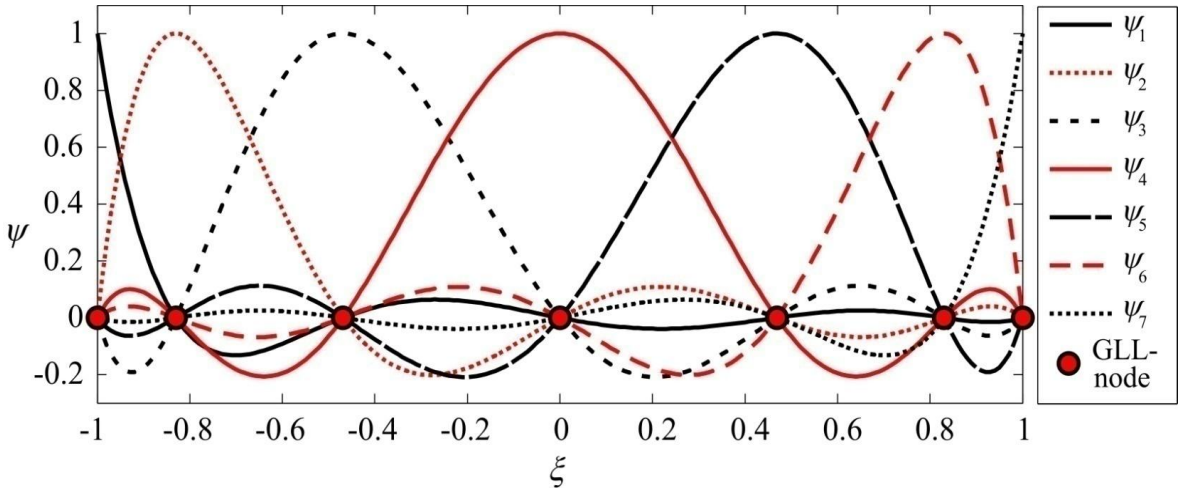

Figure 2.13 Lagrange interpolation polynomials through seven Gauss-Lobatto-Legendre (GLL) nodes in the reference interval [-1,1], [Schulte 2010]

The out-of-plane displacement, the two independent rotations and the two in-plane displacements, together five quantities are expressed in one form, [Schulte 2009]. In matrix notation the ordinary differential equations that can be written as:

$$\boldsymbol{M}\ddot{\boldsymbol{q}} + \boldsymbol{C}\dot{\boldsymbol{q}} + \boldsymbol{K}\boldsymbol{q} = \boldsymbol{F} \tag{2.22}$$

Where $\boldsymbol{M}$, $\boldsymbol{K}$ and $\boldsymbol{C}$ are the mass, stiffness and damping matrices of the structure, $\boldsymbol{q}$ is the vector of displacements and two rotational degrees of freedom. $\boldsymbol{F}$ includes normal force and moments.

In the simulation of the EMI method, the coupling of piezoelectric elements is also included Those elements contribute to the mass, stiffness and damping matrices of the structure, but the sensing equations of elements coupling the electrical and mechanical quantities have to be considered as well. Assuming isotropic piezoelectric elements, the magnitude of the induced line forces and moments at the edges of a piezoelectric element bonded onto the surface of a plate structure can be expressed as Eq. 2.23 and Eq. 2.24, [Banks 1996]:

$$N_x^{pzt} = N_y^{pzt} = \frac{-E_p h_p}{1-\nu_p}\frac{d_{31}}{h_p}V \tag{2.23}$$

$$M_x^{pzt} = M_y^{pzt} = -\frac{1}{8}\frac{E_p}{1-\nu_p}\left(4\left(\frac{h}{2}+h_p\right)^2 - h^2\right)\frac{d_{31}}{h_p}V \tag{2.24}$$

Here, h denotes the plate thickness, h_p is the thickness of the piezoelectric element, d_{31} is the piezoelectric element strain constant, E_p and ν_p are Young's modulus and Poisson's ratio of the piezoelectric element and V denotes the applied voltage. Eq. 2.25 is developed from the equations of [Lee 1990] to determine the output charges, [Yang 1999].

$$Q(t) = -\iint_S (F + \varepsilon_{33}^X E_3) dxdy + z_k \iint_S G dxdy \tag{2.25}$$

Q(t) is the output charge of the piezoelectric element, which depends on the strain occurring within the piezoelectric element, which can be seen in Eq. 2.26 and Eq. 2.27.

$$F(x,y) = e_{31}^x \frac{\partial u_0}{\partial x} + e_{32}^x \frac{\partial v_0}{\partial y} \tag{2.26}$$

u_0 and v_0 are the plane displacements.

$$G(x,y) = e_{31}^x \frac{\partial^2 w}{\partial x^2} + e_{32}^x \frac{\partial^2 w}{\partial y^2} \tag{2.27}$$

e_{31} and e_{32} are coupling coefficients, w is the out of plane displacement. Vector $\boldsymbol{q}$ in Eq. 2.22 includes w, u_0 and v_0.

The above equations show that it is possible to incorporate the electro-mechanical coupling and that it is not necessary to add further degrees of freedom. It is a straight forward to compute the forces and moments (Eq. 2.23 and Eq. 2.24) and add them to Eq. 2.22.

How to obtain the coupled EMI of piezoelectric elements by SEM can be illustrated in Figure 2.14.

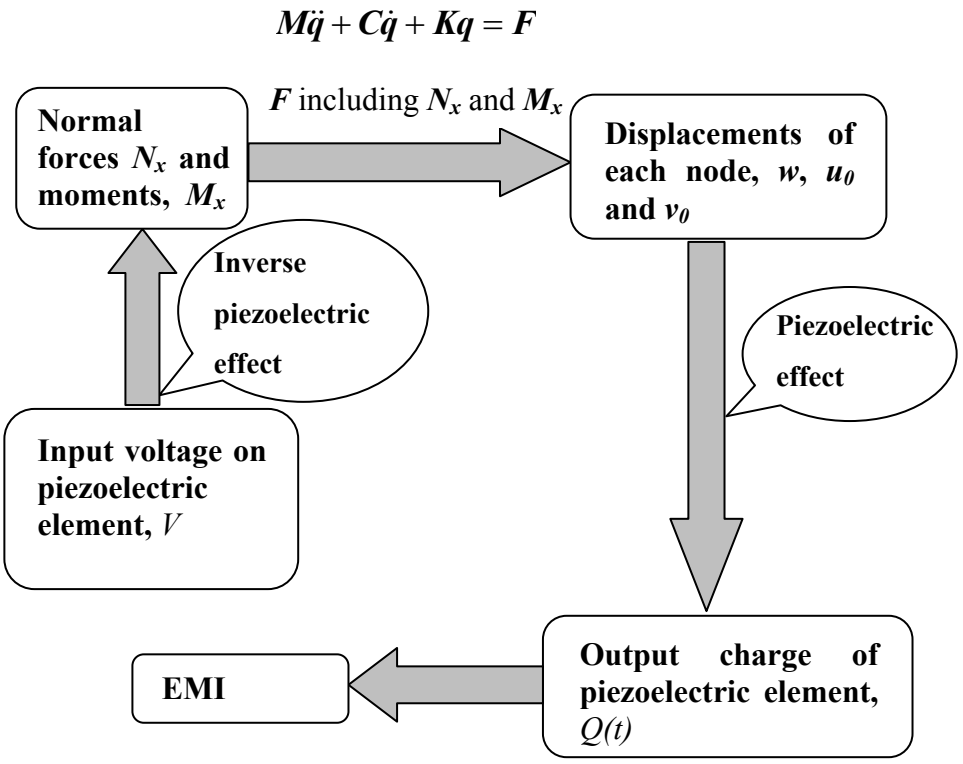

Figure 2.14 Determination of the SEM method using the E/M impedance

The input voltage (V) excites the bonded piezoelectric element and produces forces and moments (N and M), see Eq. 2.23 and Eq. 2.24, [Lee 1990], because of the inverse piezoelectric effect. The piezoelectric element forces and moments exert on the local area of the plate, from which the displacements (w, u_0, v_0) of each node of the plate can be calculated using a system of ordinary differential equations. From the deformation in the area of the plate under analysis, F and G can be obtained, see Eq. 2.26 and Eq. 2.27. The output charge of the piezoelectric element depends on the strains within the piezoelectric element, see Eq. 2.25. The output voltage, V_{Out}, is known from $Q(t)$, and Eq. 2.13 is used to obtain the coupled EMI admittance Y and impedance, $Z=1/Y$.

Using the SEM simulation approach, the efficiency of the EMI method can be clearly improved, mainly with respect to the determination of the experimental setup. In addition, this method allows the simulation of wave propagation not only in simple plates but also in complex shaped structures, e.g. a stiffened shell. In this work, the applications of SEM are described in the cross transfer function method (Chapter 3) and in the sensing area of bonded piezoelectric elements, (Chapter 5).

2.5 Phased Arrays

Damage detection, based on the phased array concept, has been developed in recent years. This concept is used extensively in radar systems where the radar dish sweeps the space with a focused ray and searches for targets. In Chapter 3, the sensing effect of a group of piezoelectric elements is investigated using the cross transfer function method. This investigation applies the concept of the phased array, by which the wave front can be focused in a certain point or steered in a specific direction and can be achieved without physically manipulating the piezoelectric elements.

Phased arrays are made up of several piezoelectric elements, identical in size and arranged along a line, bonded closely together to the structure. The distance d between the piezoelectric elements must conform to the requirement of $d/\lambda \leq 0.5$ in order to satisfy the spatial sampling theorem and to prevent grating lobes from appearing, [Giurgiutiu 2008]) and causing the superposition of waves generated by each piezoelectric element. By sequentially exciting the individual elements at slightly different times, the wave propagation can be steered in a certain direction, [Giurgiutiu 2004]. This process is called beamforming. To implement beamforming, the electronic system gives an input signal to each piezoelectric element with individual time delays. Alternatively, a computer algorithm can be used during data processing.

As mentioned above, beamforming can be achieved by giving suitable time delays to the array elements in order to control the steering angle of wave propagation. Beamforming is implemented using a phased array. Figures 2.14 and 2.15 show beamforming in near-field and far-field with a one- dimensional space linear array (1-D array). In the near field, a triangular algorithm has to be used. In the far-field, parallel rays are used.

Beamforming at certain angle is based on the principles of constructive interference. Figure 2.15 shows beamforming with J piezoelectric elements in the near-field. To get the steering angle θ, the j-th array element should be excited with a time delay t_j relative to the reference element. According to the concepts of antenna theory, [Balanis 1982], we define the ***near-field*** as the region in which

$$0.62\sqrt{D_x^3/\lambda} \leq R_{near} \leq 2D_x^2/\lambda \tag{2.28}$$

D_x is the array span, $(J-1)d$, J is the number of the piezoelectric elements in the array.

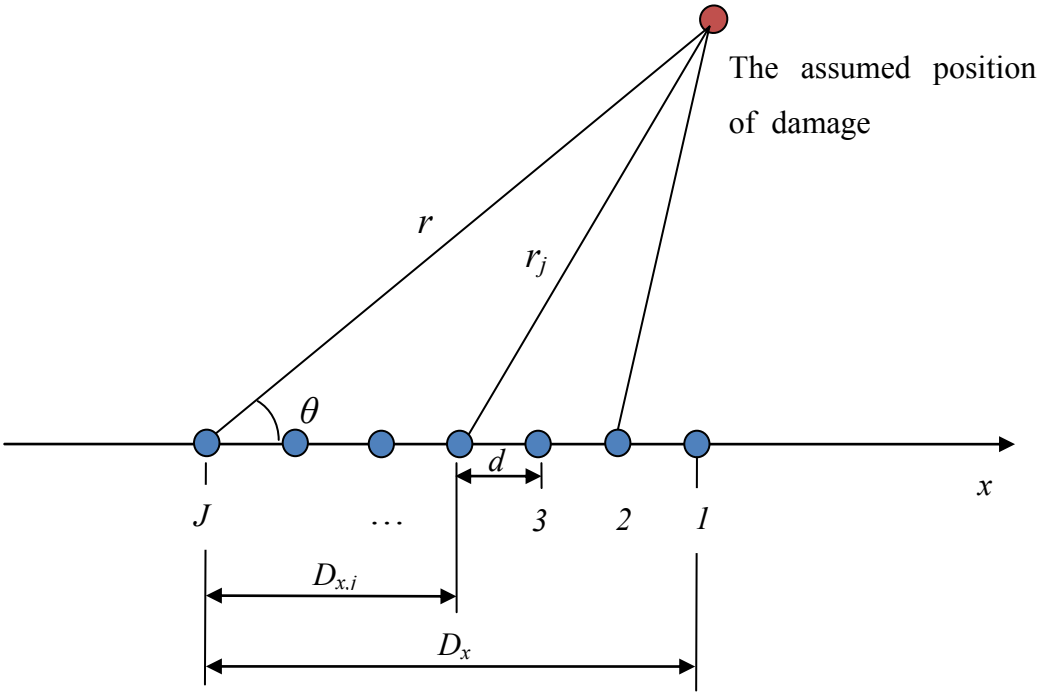

Figure 2.15 Beamforming in a 1-D array in the near-field case

$$D_{x,j} = (J - j)d \tag{2.29}$$

R_{near} is the estimated distance between the damage and the reference piezoelectric element in the array,

$D_{x,j}$ is the distance between the center of the J piezoelectric element (reference element) and that of the *jth* piezoelectric element, $j=1,2,..,J$.

In Figure 2.15, the blue points are the piezoelectric elements in the 1-D array, the red point is the assumed position of damage. If the J element is used as reference, θ as the steering angle, c is velocity of wave propagation, so the time delay t_j between element j and the reference element J should be:

$$t_j = \frac{\left|\sqrt{r^2 + D_{x,j}{}^2 - 2rD_{x,j}\cos\theta} - r\right|}{c} \tag{2.30}$$

For single frequency, c is phase velocity, c_p. However, for sweep as input signal, c is group velocity c_g.

The ***Far-field*** is defined as the region where

$$R_{far} > 2D_x{}^2/\lambda \tag{2.31}$$

The time delay t_j is given by Eq. 2.32, see Figure 2.16,

$$t_j = \frac{D_{x,j}\cos\theta}{c} \tag{2.32}$$

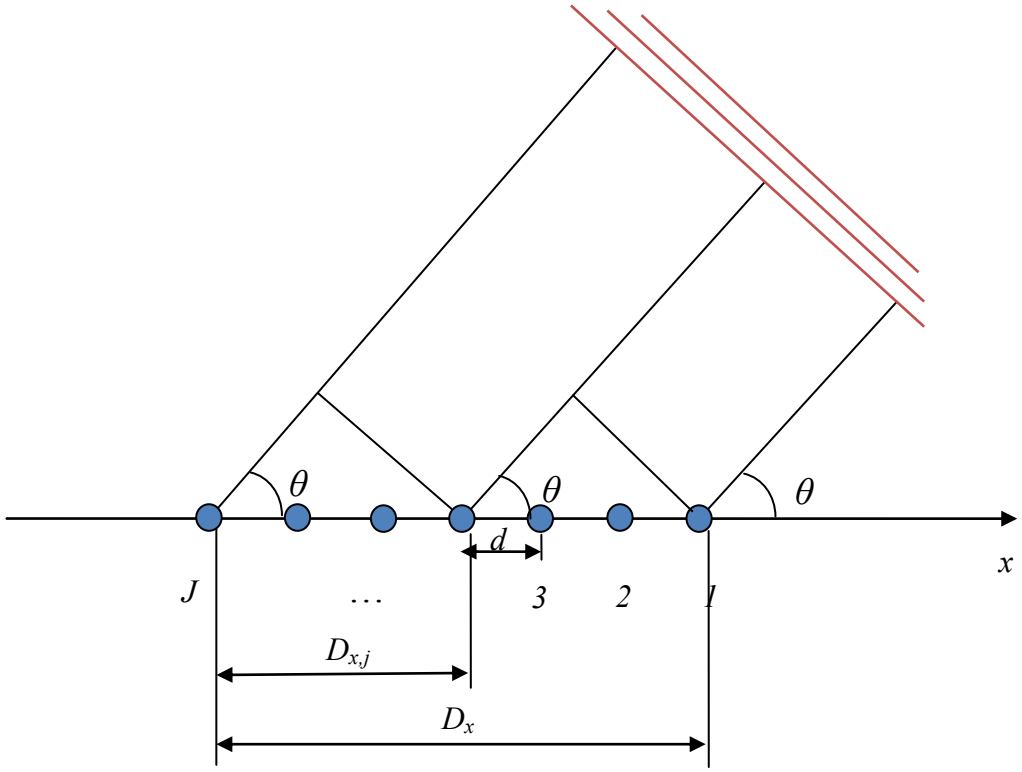

Figure 2.16 Beamforming in a 1-D array in the far-field case

From Eq. 2.32, it can be seen that beamforming takes place in two symmetrical directions, both in θ and -θ angles. There are several factors that affect beamforming, such as the location of damage, d/λ, the number of piezoelectric elements in the array, J, the steering angles, θ plus the weighting factors. In the work of [Yu 2006], an investigation into the influence of various parameters in the phased array is presented.

Beamforming can be implemented in a two- dimensional space linear array (2-D array) also. In [Malinowski 2007] and [Giurgiutiu 2008], different forms of 2-D arrays are presented, such as rectangular, crossing and circular arrays. In these works, the cross transfer function method was investigated in a T-array. It assumed that there are J piezoelectric elements in x direction and N elements in y direction, see Figure 2.17. As in a 1-D array, there are two types of beamforming of a 2-D array. One is near-field calculated with a triangularization algorithm, the other is far-field calculated with a parallel algorithm.

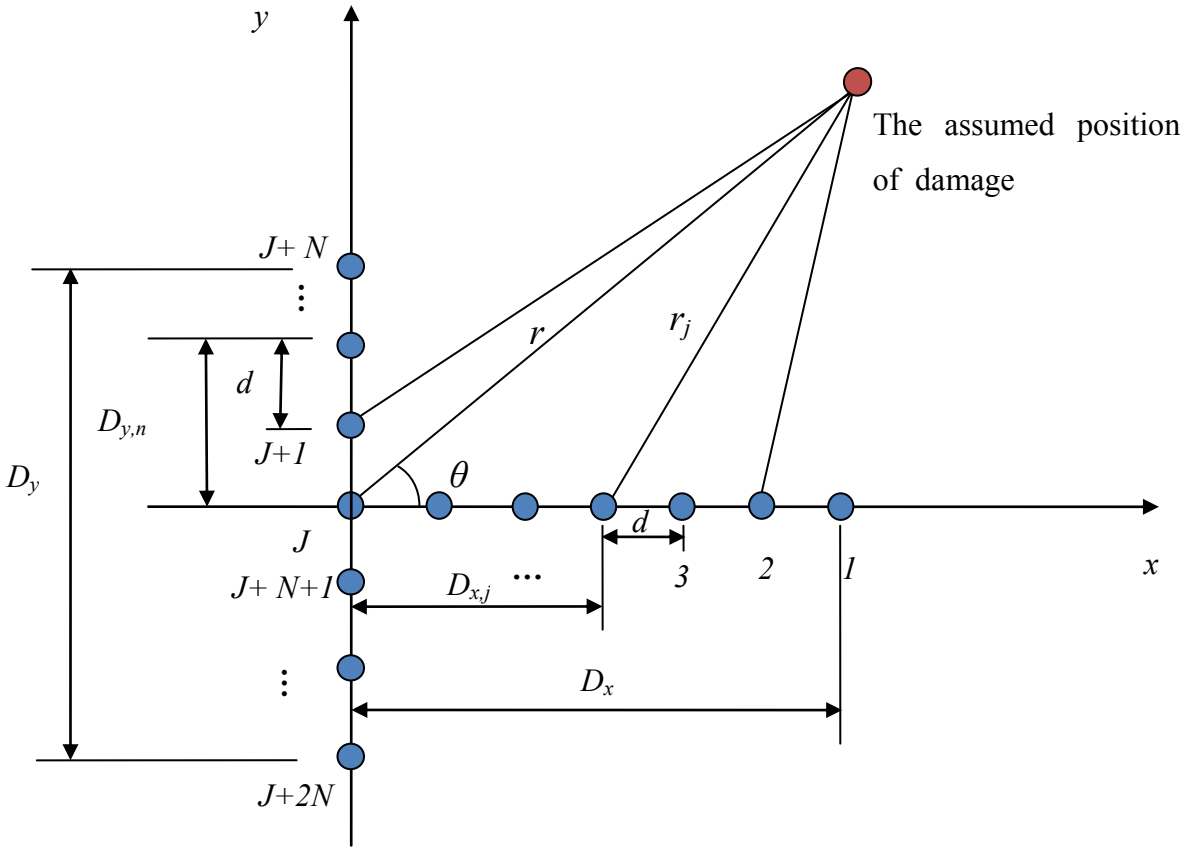

Figure 2.17 Beamforming in a T-array in the near-field case

Figure 2.17 shows beamforming in the near-field. J is as reference element. The red point is the assumed position of damage. Similar as in Eq.2.30, using θ and the assumed distance r to get the distance r_j and the distance between r and r_j, Eq. 2.33 is the time delay t_j between the input signal of one element and that of the next element. In this case, each piezoelectric element in the x array is excited consecutively, the *J-th* element first, the *(J-1)th* element second, ... ,
and the first element last.

$$t_j = \frac{\left|\sqrt{r^2 + {D_{x,j}}^2 - 2rD_{x,j}\cos\theta} - r\right|}{c} \tag{2.33}$$

$D_{x,j}$ is the distance between the center of the J piezoelectric element and that of the *jth* piezoelectric element, $j=1,2,..,J$, see Eq. 2.29.

For the y-array, J element is as reference element, the time delay t_n to reference element is:

$$t_n = \frac{\left|\sqrt{r^2 + {D_{y,n}}^2 - 2rD_{y,n}\cos(\frac{\pi}{2} - \theta)} - r\right|}{c} \tag{2.34}$$

$$D_y = 2N \cdot d \tag{2.35}$$

$$D_{y,n} = nd \tag{2.36}$$

D_y is the array span in the *y* direction, $D_{y,n}$ the distance between the *Jth* piezoelectric element and the *(J+n)th* piezoelectric element in the *y* direction, *n=1,2..,N*.

In a ***far-field*** case, see Figure 2.18, *J* piezoelectric element is used as the reference element. For the *x*-array,

$$t_j = \frac{D_{x,j} \cdot \cos\theta}{c} \tag{2.37}$$

$D_{x,j}$ is the distance between the center of the *J* piezoelectric element and the center of the *jth* piezoelectric element, see Eq. 2.29.

For the *y*- array, t_n depends on the order of exciting input signals,

$$t_n = \frac{D_{y,n} \cdot \cos(\frac{\pi}{2} - \theta)}{c} \tag{2.38}$$

$D_{y,n}$ is the distance between the *Jth* piezoelectric element and the *(J+n)th* piezoelectric element in the *y* direction, see Eq. 2.36.

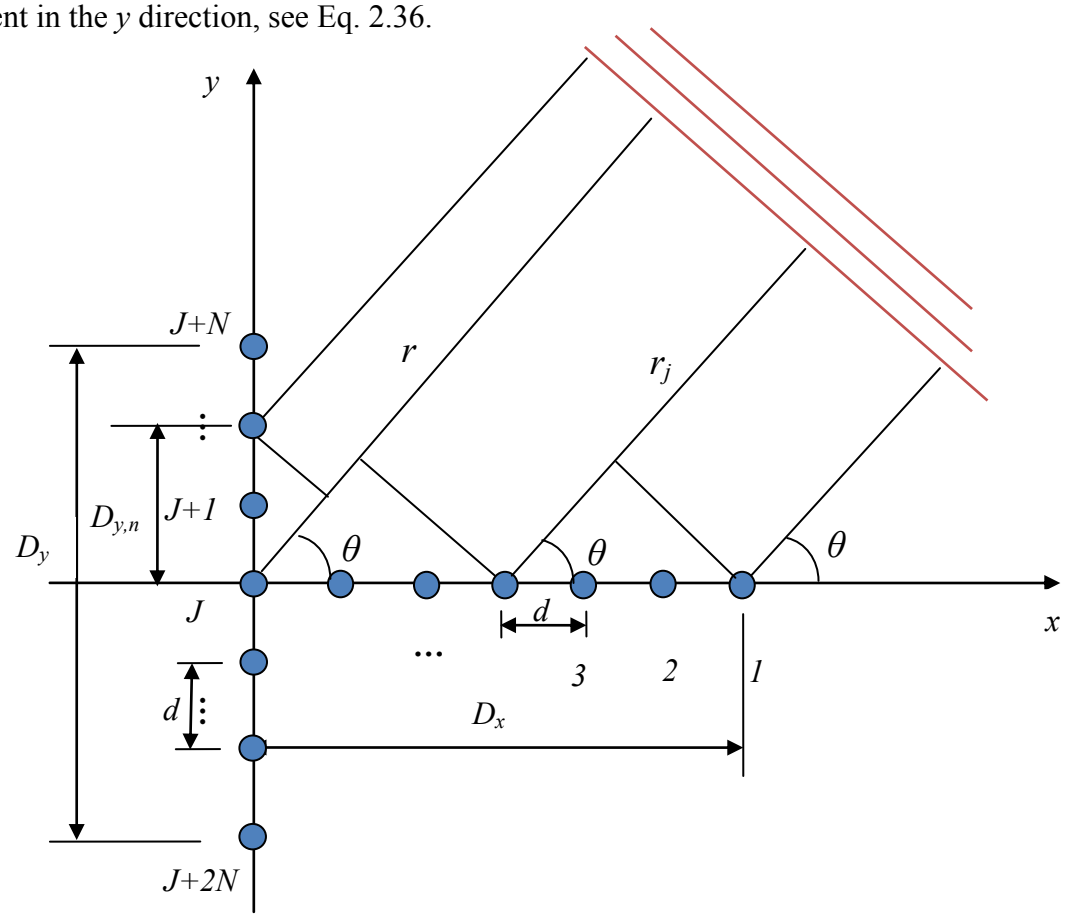

Figure 2.18 Beamforming in T-array in far-field case

In the investigation of the cross transfer method (see Chapter 3), the piezoelectric elements are positioned close to each other in both the 1-D array and the T-array, thus meeting the requirement of $d/\lambda \leq 0.5$. Furthermore, any discontinuity causing wave reflection is far enough from the array to have no impact on the analysis. To determine if the phased arrays used in the investigation of the cross transfer method belong to the far-field, the wave length is obtained by using a model of wave velocity and Eq. 2.33. This procedure is shown in section 3.3.1.

There are two methods to implement a time delay in beamforming. One is by using a hardware solution whereby the electronic system gives an input signal to each piezoelectric element with individual time delays. The other method is by using a software solution. In this work, a software solution is chosen as the beamforming method. Data evaluation is implemented in the frequency domain leading to a cross transfer function method. The time delay is implemented by a computer algorithm using a post processing after the data acquisition.

3 Cross Transfer Function Method for the Phased Array

To carry out damage detection using group piezoelectric elements, a phased array is used in SHM. This concept is analogous to radar technology. As mentioned in 2.5, when beamforming, the waves scan omni-directionally rather like radar. When damage occurs in the structure the property of the structure is changed and the output information obtained from the piezoelectric elements is different from that obtained when the structure is undamaged. Using data evaluation the state of the structure can be further analysed.

The phased array was applied in an SHM system by [Giurgiutiu 2002]. Until now, in most applications, data evaluation has been implemented in the time domain. Beamforming in a phased array is implemented with electronic hardware and software solution. In this work, a computer algorithm is used when applying the cross transfer method for beamforming, and the data is evaluated in the frequency domain. In [Boychuk 2014], similar phased array technique is applied in CFRP material.

3.1 The Theory of the Cross Transfer Function Method

To describe the cross transfer function method, a 1-D phased array is considered. Because it is considered to have a more uniform dispersion, a round lead zirconate titanate (PZT) is chosen. It is assumed that there are J PZTs located in the center of the plate, see Figure 3.1. According to the far-field definition, see Eq. 2.32, in this example, beamforming is implemented in the far-field, which means that the wave propagation rays are parallel. An explanation of this example is given in the simulation of phased array by using the Spectral Element Method (SEM), 3.3.1.

To implement a software-based beamforming, measurements are taken during the experiment. One of the PZTs is excited by an input signal, while the outputs of all other PZTs are measured synchronously. The excited PZT acts as an actuator, while the others act as passive sensors. In the same way, each PZT acts as an actuator consecutively, while the others act as sensors.

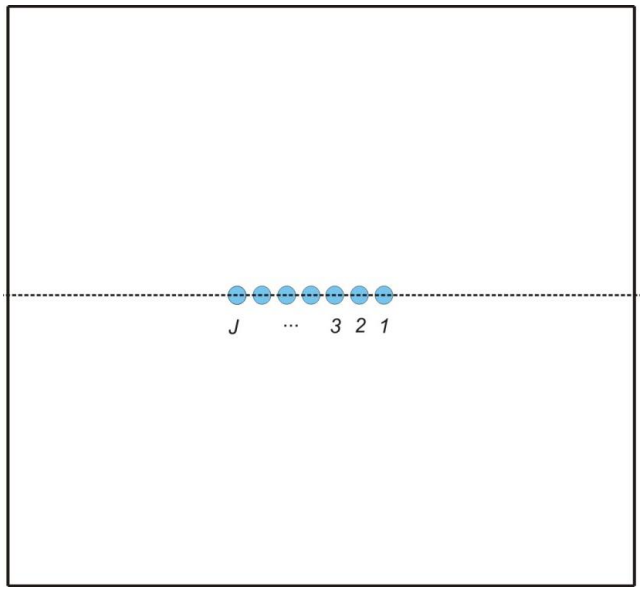

Figure 3.1 Schematic diagram of the plate with 1-D array

In the experiment, input voltage V is given to the one of the PZTs, at the same time the output voltage V_{Out} of the rest PZTs is measured. Following on from this, the measured data are used to get the cross transfer functions in the frequency domain according to the following steps:

Step1. Using the measurements, we obtain the transfer function, ***H***.

Eq. 3.1, Eq. 3.2 and Eq. 3.3 show the transfer functions when P1 functions as an actuator ($j=1$) The transfer function $h_{k1}(i\omega)$ is a vector. The number of elements in the vector is determined by the sample frequency during the transfer from the time domain to the frequency domain. k is the number of output voltages (PZTs act as sensors at that moment), $k=1,2,...,J$.

$$h_{21}(i\omega)=\frac{V_{Out2}(i\omega)}{V_1(i\omega)}, \tag{3.1}$$

$$h_{31}(i\omega)=\frac{V_{Out3}(i\omega)}{V_1(i\omega)}, \tag{3.2}$$

….

$$h_{k1}(i\omega)=\frac{V_{Outk}(i\omega)}{V_1(i\omega)}, \tag{3.3}$$

When each actuator PZT receives an input signal, square matrices are created from cross transfer functions , see Eq. 3.4.

$$\boldsymbol{H} = \begin{bmatrix} 0 & h_{12} & h_{13} & . & . & . & h_{1J} \\ h_{21} & 0 & h_{23} & . & . & . & h_{2J} \\ h_{31} & h_{32} & 0 & . & . & . & h_{3J} \\ . & . & . & 0 & . & . & . \\ . & . & . & . & 0 & . & . \\ h_{(k-1)1} & h_{(k-1)2} & . & . & . & 0 & h_{(k-1)J} \\ h_{k1} & h_{k2} & . & . & . & . & 0 \end{bmatrix} \tag{3.4}$$

Theoretically, $h_{kj}(i\omega)$ should be identical to $h_{jk}(i\omega)$. This means that the transferred results are the same when the *jth* acts as actuator and the *kth* acts as passive sensor or vice-versa. This is proven by the Correlation Coefficient (CC). The CC results of both vectors are close to +1 or –1, which means that $h_{kj}(i\omega)$ and $h_{jk}(i\omega)$ are almost identical. For example, Figure 3.2 shows the spectrum of $h_{17}(i\omega)$ and $h_{71}(i\omega)$.

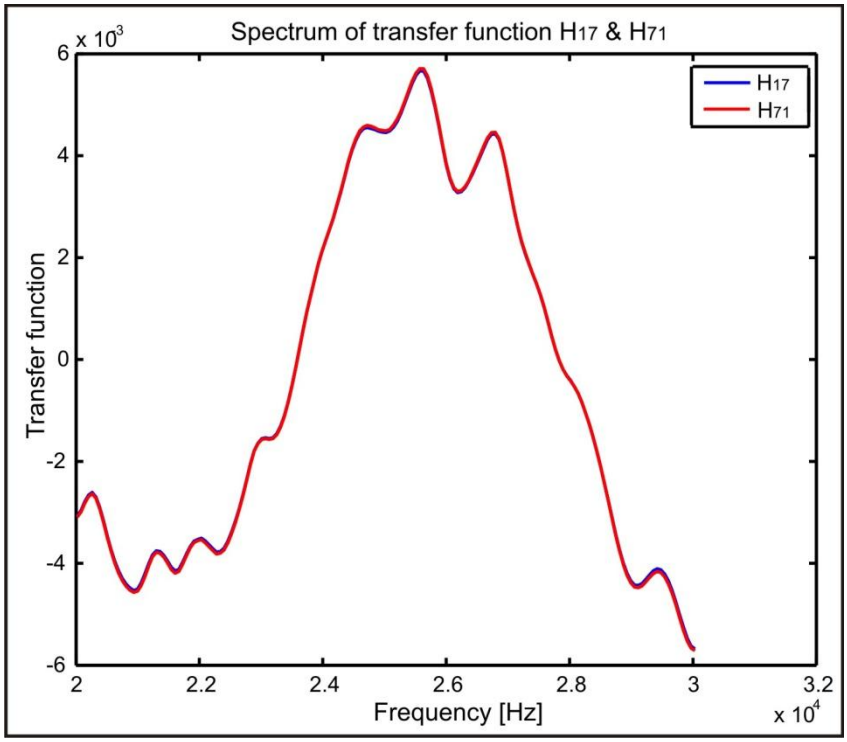

Figure 3.2 The spectrum of H_{17} and H_{71}

From Eq. 3.1, Eq. 3.2 and Eq. 3.3, so the total outputs of *kth* PZT is $h_{k1}(i\omega)V_1+h_{k2}(i\omega)V_2+...+h_{kj}(i\omega)V_j$, V_j is the input voltage given to the *jth* PZT (as actuator). The different excitations ($j=1,2,...,J$) can be done separately. And the output voltage at *kth* PZT with excitations at different PZT, V_j, can be superimposed afterwards due to the linearity of the system.

To get the certain steering angle of the wave front (beamforming mentioned in section 2.5), the time delay of the input signals need to be used. Beamforming result from the process of superimposing the outputs of each PZT in the array. Here a computer algorithm can implement the time delay instead of physically manipulating the piezoelectric elements. And also the superimposition of outputs is achieved. Using Fourier-transform the input time delay can be transformed to phase shift in frequency domain.

Step2. To implement beamforming by using phased delay, transfer function matrix with delay without damage, $\boldsymbol{T}$, output voltage with delay, $v_{\boldsymbol{Out}}$.

$e^{-i\cdot\varphi}$ is used to generate phase shift to the input signal, where φ is the phase unit between two input signals. The output voltage of the *kth* PZT is the superimposition of all the voltages which are produced by the input signal at different PZTs ($V_1, V_2, ..., V_j$) with different phase shifts, see Eq. 3.5.

$$V_{Out,k}=h_{k1}(i\omega)V_1\, e^{-i0\varphi}+h_{k2}(i\omega)V_2\, e^{-i\varphi}+...+h_{kj}(i\omega)V_j\, e^{-i(j-1)\varphi} \tag{3.5}$$

We can write

$$v_{\boldsymbol{Out}} = \boldsymbol{H}\,\boldsymbol{S}\,\boldsymbol{v} = \boldsymbol{T}\boldsymbol{v} \tag{3.6}$$

$\boldsymbol{H}$ is the transfer function matrix, see Eq. 3.4

$$\boldsymbol{S} = \begin{bmatrix} e^{-i0\varphi} & 0 & 0 & . & . & . & 0 \\ 0 & e^{-i\varphi} & 0 & . & . & . & 0 \\ 0 & 0 & e^{-i2\varphi} & . & . & . & 0 \\ . & . & . & ... & . & . & . \\ . & . & . & . & ... & . & . \\ 0 & 0 & . & . & . & e^{-i(j-2)\varphi} & 0 \\ 0 & 0 & . & . & 0 & 0 & e^{-i(j-1)\varphi} \end{bmatrix} \tag{3.7}$$

$$\boldsymbol{v} = \begin{bmatrix} V_1 \\ V_2 \\ \vdots \\ V_j \end{bmatrix} = \begin{bmatrix} w_{m,1} \\ w_{m,2} \\ \vdots \\ w_{m,j} \end{bmatrix} \cdot V \tag{3.8}$$

Where $w_{m,j}$ is the weighting factor. For uniform phased array $w_{m,j}=1$, the input signal of each PZT are identical. However for nonuniform phased array $w_{m,j} \neq 1$, the input signal of each PZT are not identical.

Using the definitions of far-field, see Eq. 2.32, as well as the input frequency,

$$\varphi = \omega \cdot t_j = \frac{\omega D_x \cos\theta}{c} \tag{3.9}$$

ω is the frequency of the input signal,

t_j is the time delay of the input signal between consecutively excited PZTs, [Malinowski 2007]. Eq. 3.9 shows the relationship between phase unit φ and the steering angle θ.

From above, we get the transfer function and output voltages with delay,

$$\boldsymbol{T} = \boldsymbol{H}\boldsymbol{S} \tag{3.10}$$

$$\boldsymbol{v}_{Out} = \boldsymbol{T}\boldsymbol{v} \tag{3.11}$$

Step 3. The transfer function matrix for the damaged state, $\boldsymbol{H}_D$

Returning to the experiment, the output of each PZT is measured respectively in the damaged state of the structure,

$$\boldsymbol{H}_D = \begin{bmatrix} 0 & h_{D12} & h_{D13} & . & . & . & h_{D1j} \\ h_{D21} & 0 & h_{D23} & . & . & . & h_{D2j} \\ h_{D31} & h_{D32} & 0 & . & . & . & h_{D3j} \\ . & . & . & 0 & . & . & . \\ . & . & . & . & 0 & . & . \\ h_{D(k-1)1} & h_{D(k-1)2} & . & . & . & 0 & h_{D(k-1)j} \\ h_{Dk1} & h_{Dk2} & . & . & . & . & 0 \end{bmatrix} \tag{3.12}$$

Step 4. To implement beamforming in the matrix of damaged state, $\boldsymbol{T}_D$ (Transfer function matrix with delay with damage)

$$\boldsymbol{T}_D = \boldsymbol{H}_D \boldsymbol{S} \tag{3.13}$$

$$v_{Out,D} = \boldsymbol{T}_D \, \boldsymbol{v} \tag{3.14}$$

Step 5. The matrices including cross transfer functions and the steering angles are obtained, see Eq. 3.11 and Eq. 3.14. From superposition with delay, see Eq. 3.5, we get a beamforming effect. From Eq. 3.9 it can be seen that steering angle θ corresponds to phase unit φ, which depends on the time delay. If the damage appears in the lobe of the steering angle, we expect a strong change of output voltage.

Similar to the EMI method, to know how strong the difference of outputs before and after damage, $\boldsymbol{v}_{Out,D}$ and $\boldsymbol{v}_{Out}$ are compared. When the spectrum of the vector at the same angle, is

shifted it means that the property of the structure has changed. Therefore, Damage Metrics (DMs) (see section 2.2.3) are used in the cross transfer function method as well. The DMs at different steering angles are calculated and compared. If the DM at one angle or between two angles is distinctly larger than other DMs, the large possibility is that damage has occurred in that area. The data evaluation of the cross transfer function method using DM will be shown in detail in section 3.3.

3.2 Nonuniform Phased Array with Dolph-Chebyshev Distribution

If a phased array consists of identical PZTs excited by an identical amplitude input signal, it is referred to as a uniform array. In a nonuniform phased array, either the function of each PZT is different, or the amplitude of the input signal is different. Using a nonuniform phased array may coincide more with the reality where different weighting factors are given for each PZT in the phased array.

There are two widely used distributions, the binominal distribution and the Dolph-Chebyshev distribution. In [Giurgiutiu 2008], the former was used indicating that binomial distribution has less directional wave propagation when compared to the directivity of the uniform array. In addition, the binomial distribution loses its zero-sidelobe advantage as the direction of the beamforming moves away from 90°. This is why the Dolph-Chebyshev array is introduced and used in the phased array when using the cross transfer method: it utilizes the principle of Chebyshev distribution and its excitation coefficients are related to Chebyshev polynomials.

The appropriate weight in a Dolph-Chebyshev distribution is selected by:

$$(AF)_{2L} = \sum_{n=1}^{L} a_n \cos[(2n-1)u] \tag{3.15}$$

$$(AF)_{2L+1} = \sum_{n=1}^{L+1} a_n \cos[2(n-1)u] \tag{3.16}$$

Where AF is the weight polynomial in a Dolph-Chebyshev distribution.

$$u = \frac{\pi d}{\lambda} \cos\theta \tag{3.17}$$

When the number of PZTs in a phased array is even, Eq. 3.15 is used. When the number of PZTs is odd, Eq. 3.16 is chosen. For example, if there were 7 PZTs in the 1-D array in the

experiments conducted as part of this work, Eq. 3.16 was used, *n* being from *1* to *4*, *L* being *3*. The weighting factors are given by Eq. 3.18,

$$(AF)_{2x3+1} = \sum_{n=1}^{3+1} a_n \cos[2(n-1)u] \tag{3.18}$$

a_n is the value of the excitation coefficients. Each cosine term can be rewritten as a series of cosine functions with the fundamental frequency as argument, [Balanis 1982].

$$(AF)_7 = a_1 + a_2 \cos 2u + a_3 \cos 4u + a_4 \cos 6u \tag{3.19}$$

$$\cos 2u = 2\cos^2 u - 1$$
$$\cos 4u = 8\cos^4 u - 8\cos^2 u + 1$$
$$\cos 6u = 32\cos^6 u - 48\cos^4 u + 18\cos^2 u - 1$$

The coefficients of the weighting factor with 7 PZTs in a 1-D array form a major-to-minor lobe ratio of 26dB determined by the following Dolph-Chebyshev polynomial:

a_4=*2.9121;*

a_3=*5.2368;*

a_2=*7.5903;*

a_1=*4.2656;*

In the normalized form, the coefficients can be written as:

w_{m4}=*0.3837;*

w_{m3}=*0.6899;* (3.20)

w_{m2}=*1*

w_{m1}=*0.562;*

The weighting factors with 7 PZT, $\boldsymbol{w_m}$, is the normalized coefficients. From Eq. 3.19, the input signals with weighting factors can be obtained.

The application of the weighting factors is described in section 3.3.2, where the cross transfer function method in a nonuniform 1-D array is investigated. The effect of beamforming using weight factors is shown in the accompanying figures.

3.3 Applications of the Cross Transfer Function Method

The basic principles behind the algorithm of the cross transfer function method used in phased array are described above. This method is applied in the case of a 1-D uniform array, 1-D nonuniform array and 2-D uniform array and are described in this chapter. In all cases, an aluminium plate (1000mm x 1000mm x 2mm) is used as the structure under investigation.

As mentioned previously, a round PZT is chosen as the piezoelectric element. This element is 15mm in diameter and 0.2mm thick. It is assumed that all the PZTs are omni-directional sources of wave. In the case of 1-D array, there are 7 PZTS bonded to the middle of the aluminium plate, see Figure 3.1. In the 2-D array, there are 7 PZTs bonded in x direction and 6 PZTs bonded in y direction. Due to the form of the bonded PZTs in the 2-D array, this arrangement is called a T-array, see Figure 3.8.

The distance between the center of one PZT and the center of the next PZT is 23mm. In the experiments carried out as part of this work, the input signal was applied and measurements were logged in both undamaged and damaged states. In the damaged state, two magnets were fixed to the structure as damage. After one complete measurement, the magnets were moved one angle unit (20° in the experiment) further and then more measurements were taken until the magnets occurred in a semi-circle around the array. By using Eq. 3.10, Eq. 3.11, Eq.3.13 and Eq. 3.14, the 7x7 matrices with phase delay $\boldsymbol{T_D}$ and $\boldsymbol{T}$, vectors $\boldsymbol{v_{Out,D}}$ and $\boldsymbol{v_{Out}}$ are obtained, from which DMs are calculated, see Eq. 2.14. DMs at different steering angles are then compared in bar figures.

In the applications of the cross transfer function method, the time delay (t_j) algorithm for beamforming should be determined. Figure 3.3 shows the wave group velocities in three different modes for aluminium. The red lines are the antisymmetric modes and the blue lines symmetric modes. It can be seen that S_0 and A_0 exist at all frequencies and that the A_0 velocity is lower than that of the S_0's. As explained in section 2.3, because of A_0´s sensitivity to small damages, it is usually deployed in damage detection studies.

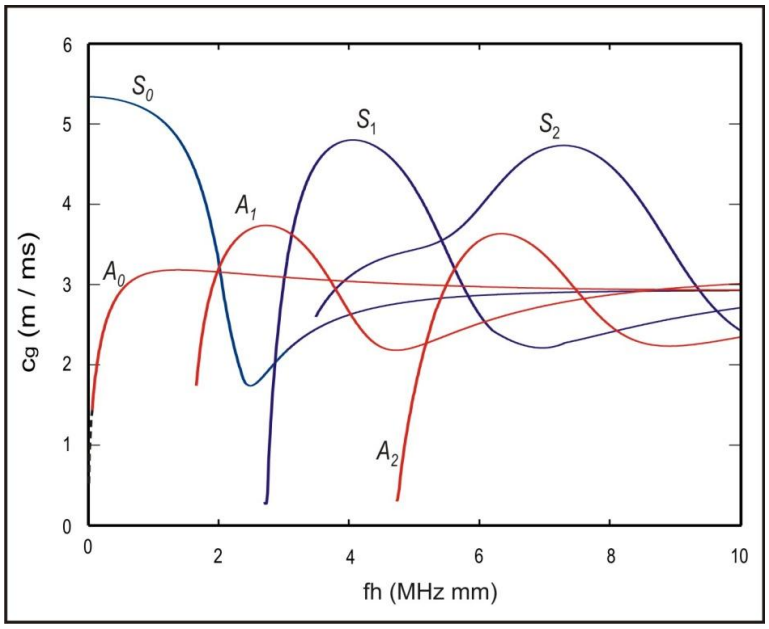

Figure 3.3 Group velocity of Lamb waves in different mode

In the simulations and experiments below, the frequency of the input signal is a sweep from 0.02 MHz to 0.03 MHz and the thickness of the aluminium plate is 2mm.

Figure 3.3 shows that the maximum velocity between 0.04 and 0.06 MHz mm is about 1.75 m/ms. Using the definitions of near-field and far-field (see Eq. 2.28 and Eq. 2.31), it can be calculated that, if the position of the damage is greater than 5.83cm, the parallel algorithm in the case of far-field is used for time delay, see Eq. 2.32 (for the 1-D array) or Eq. 2.37 and Eq. 2.39 (for the T-array). In the experiment below, only the far-field case is considered.

Before carrying out the experiments using the cross transfer function method, beamforming numerical simulations are conducted by the spectral element method (SEM) in the aluminium plate bonded with the PZT array. The snapshots of wave propagations in the 1-D array and T-array that these simulations provide are shown in figures. Such simulations give a preliminary idea of the effect that beamforming will have in both array cases.

3.3.1 Beamforming simulation with SEM

In a SHM system, simulations help to both set up the experiment and to evaluate the measured data thus obtained. As mentioned in section 2.4, the spectral element method (SEM) is chosen in this work.

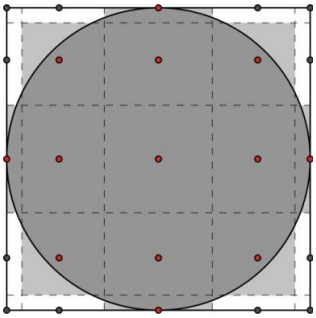

Figure 3.4 An approximation of round PZT with SEM

In the following simulation, the structural system as in Figure 3.1 is simulated using the SEM. In this simulation, the model of the plate is divided into 1521 spectral elements, with 5 Gauss-Lobatto-Legendre (GLL) nodes per element and the round PZT is approximated by small polygons that are constructed from the interior spectral nodes of an element that has exactly the same edge length as the diameter of the PZT. In the calculation of the corresponding element matrices, those element areas that are not covered by the round PZT are omitted.

The procedure is illustrated in Figure 3.4, [Schulte 2010]: The element is subdivided into light and dark gray areas according to the integration weights allocated to each node in the integration. Only if the respective sub-area is covered by more than 50% from the PZT - the dark gray area, are the relevant values taken into account at that node. Thus, the round PZT is approximated in the polygonal form.

As mentioned in section 2.4, there are two in plane displacements (x, y directions) and one out of plane displacement (z direction). These displacements are determined by the forces and moments produced by the input signal, see Eq. 2.23 and Eq. 2.24. The simulation of wave propagation comes from the superposition of the z displacements. The beamforming in the simulation is created by using the time delay t_j, see Eq. 2.32.

Snapshots of beamforming wave propagations using SEM are demonstrated in the following figures. Figure 3.5 shows the wave propagation beamformed at 20°. It can be seen that the main lobe, which is defined as the propagated wave reaching its maximum in a certain direction, is at approximately 20° and -20°. To the left of the x axis, there is a side lobe which represents an additional propagation in an undesired direction.

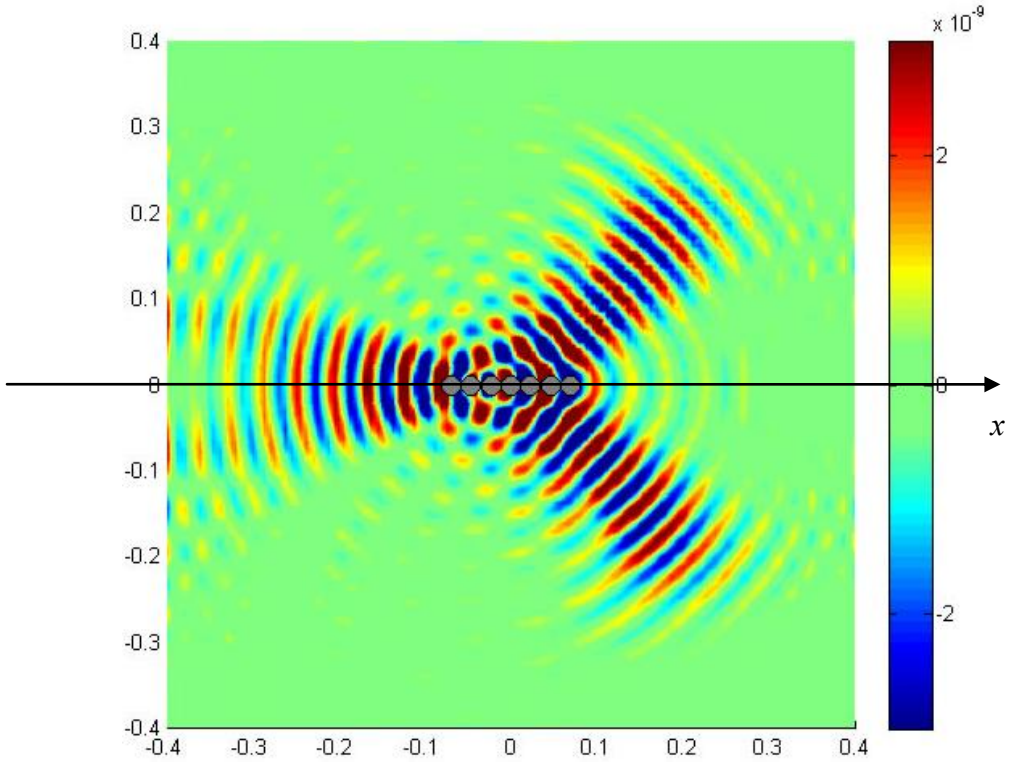

Figure 3.5 Beamforming simulation by SEM at 20° in the 1-D array

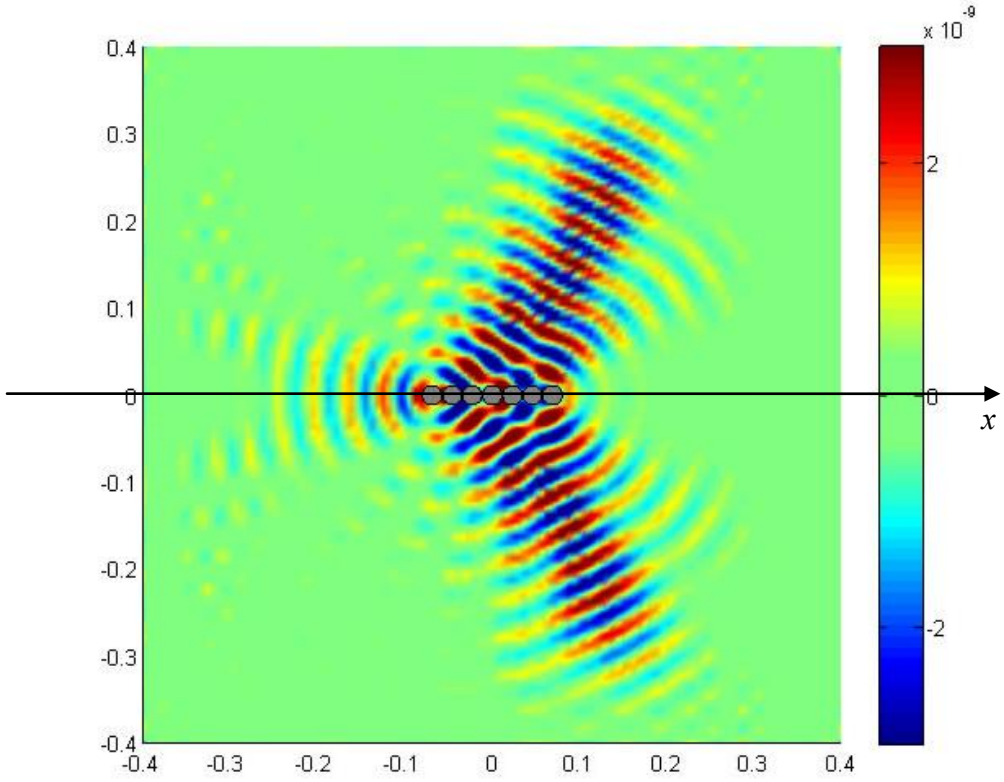

Figure 3.6 Beamforming simulation by SEM at 40° in the 1-D array

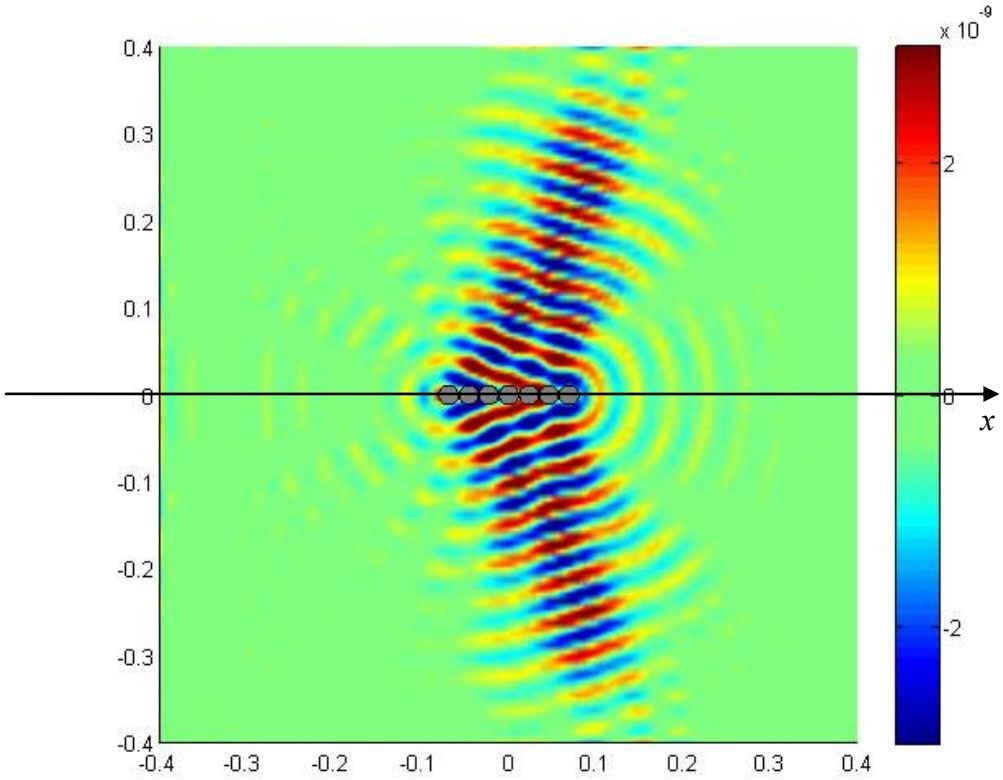

Figure 3.7 Beamforming simulation by SEM at 60° in the 1-D array

However, when the steering angle is 40° or 60°, the wave propagations become more directional, see Figure 3.6 and Figure 3.7. In both cases, the side lobes are reduced. From these three examples, it can be seen that the linear array always leads to two main lobes, one in the direction of the steering angle (20°, 40° or 60°), and the other in a symmetrical direction to the x axis. These findings can be explained by the theory of the phased array, see Eq. 2.32, $cos\theta$ and $cos(-\theta)$ having the same effect regarding the control of the time delay, t_j.

In section 2.5, it was mentioned that both a 1-D linear array and a 2-D array are used in an SHM system. Beamforming simulation by SEM is also implemented in a T-array.

Figure 3.8 shows two perpendicular linear arrays consisting of bonded PZTs. $J=7$, $N=3$.

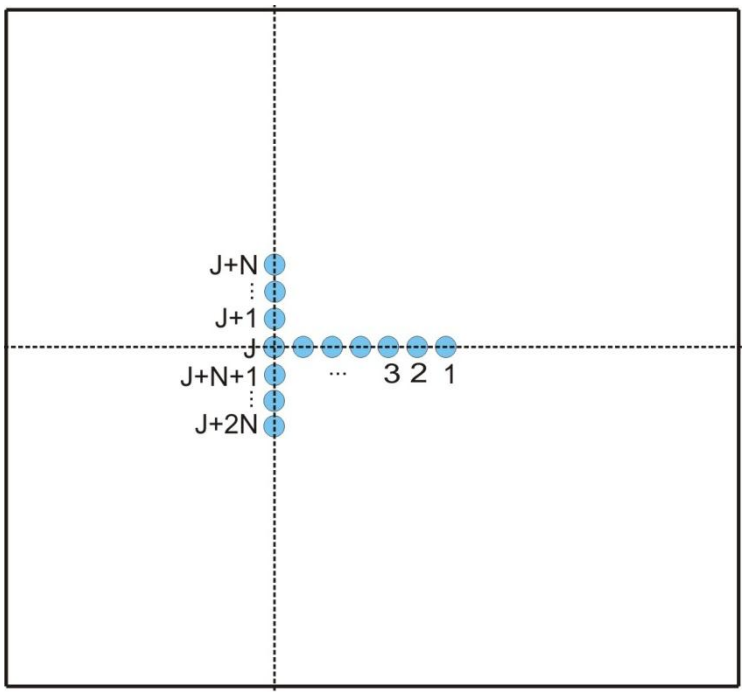

Figure 3.8 The schematic diagram of T-array

As in the 1-D array, the superposition of the z displacements of all the spectral elements in the plate result in wave propagation in the T-array. Beamforming in the simulation is decided by t_j, see Eq. 2.37 and Eq. 2.38.

Figures 3.9, 3.10 and 3.11 are snapshots of beamforming wave propagations by SEM using a T-array. The main lobes in Figure 3.9 and 3.10 cannot be distinguished from the side lobes which occur between 60° and 80°, as well as around 180°.

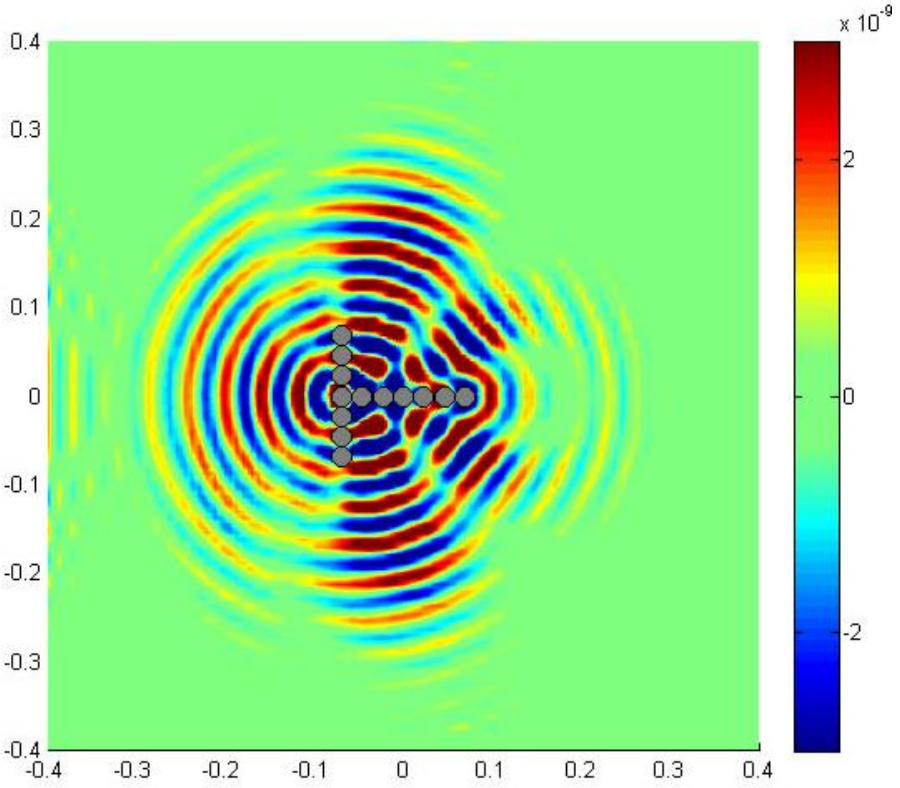

Figure 3.9 Beamforming simulation by SEM at 20° in the T-array

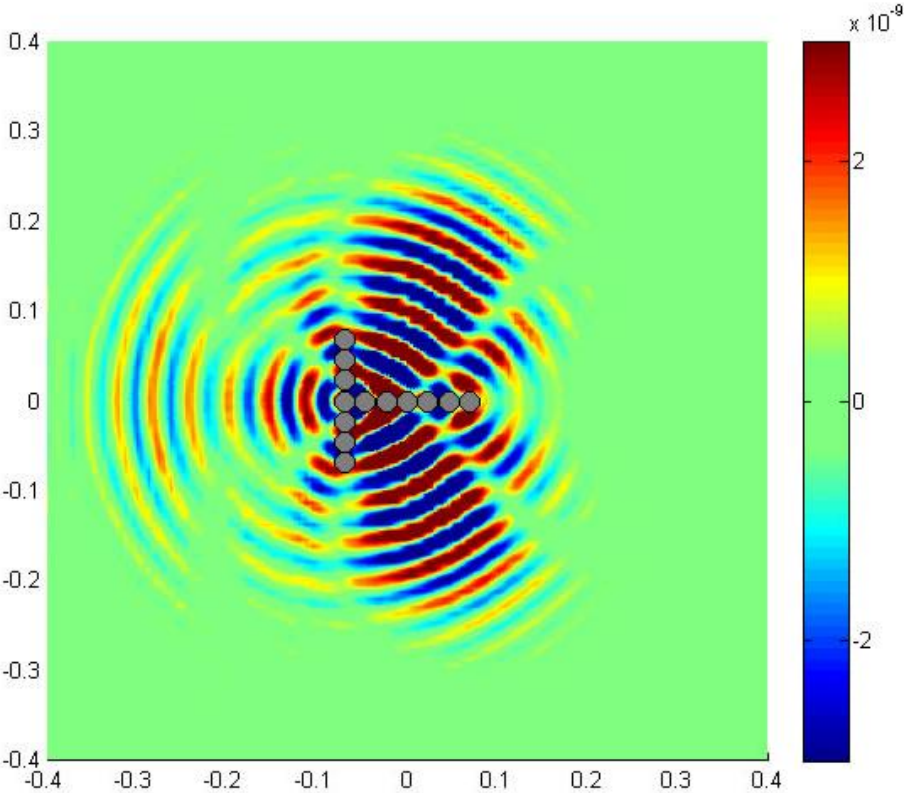

Figure 3.10 Beamforming simulation by SEM at 40° in the T-array

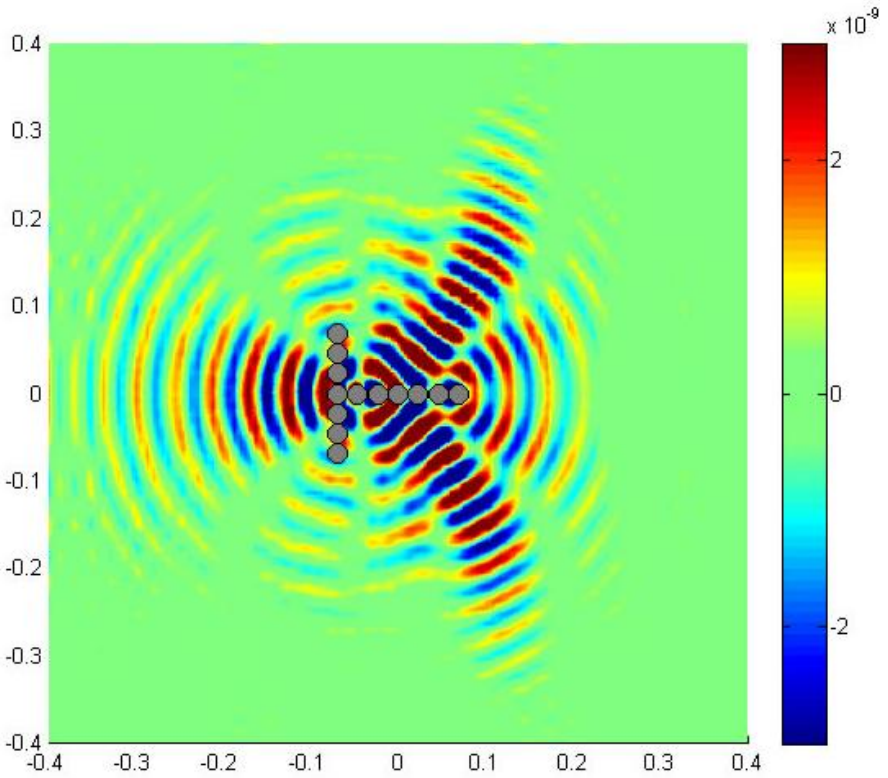

Figure 3.11 Beamforming simulation by SEM at 60° in T-array

In Figure 3.11, the main lobe can be seen at about 60°, and there are side lobes at 30° and -30°. It appears that simulated beamforming at 20°, 40° and 60° in a T-array is not as well-directed as in the 1-D array case (see Figures 3.5, 3.6 and 3.7).

In the experiments described in sections 3.3.2 and 3.3.4, the effects of beamforming in a 1-D array and a T-array are shown as DM bar figures calculated using the cross transfer function method.

3.3.2 Experiment: - the cross transfer function method in a uniform phased array

In this experiment an aluminium plate bonded with a 7 PZT 1-D array is used. To attenuate the influence of the reflected waves, in the following experiments anti-drumming material is fixed at the four edges of the plate, see Figure 3.12. In the case of the uniform phased array, it is assumed that the 7 PZTs are identical, and the exciting signals are equal.

During the measurement process one PZT acting as an actuator is excited by an input sweep signal (20-30kHz, 5 seconds) and the outputs of the other six PZTs are measured. Then, one of the seven PZTs acts as the actuator while the remaining six PZTs act as sensors, and so on.

The process is repeated until each of the PZTs has functioned as an actuator. Two magnets are used to simulate damage to the structure system. Where the two magnets were located as in Figure 3.12, the above measurements were recorded. The magnets are located around the PZT array. This assumes that there are nine different damage states (20°, 40°,60°... 160° and 180°), one for every 20° of a 180° arc.

The cross transfer functions matrices $\boldsymbol{H_D}$ and $\boldsymbol{H}$ were measured at damaged and undamaged states respectively. To implement phased array, matrix $\boldsymbol{S}$ **(**which is decided by steering angle φ) is used, transfer functions matrices $\boldsymbol{T_D}$ and $\boldsymbol{T}$ (see Eq. 3.13 and Eq. 3.10), $\boldsymbol{v_{Out,D}}$ and $\boldsymbol{v_{Out}}$ (see Eq. 3.14 and Eq. 3.11) are obtained. A steering angle θ is taken respectively as 0, $\pi/18$, $\pi/9$, $\pi/6$... $17\pi/18$ and π. In other words, 18 different angles of arc altogether. By using the Difference Damage Metrics Method (in section 2.2.3), DMs in different damaged states are obtained and compared.

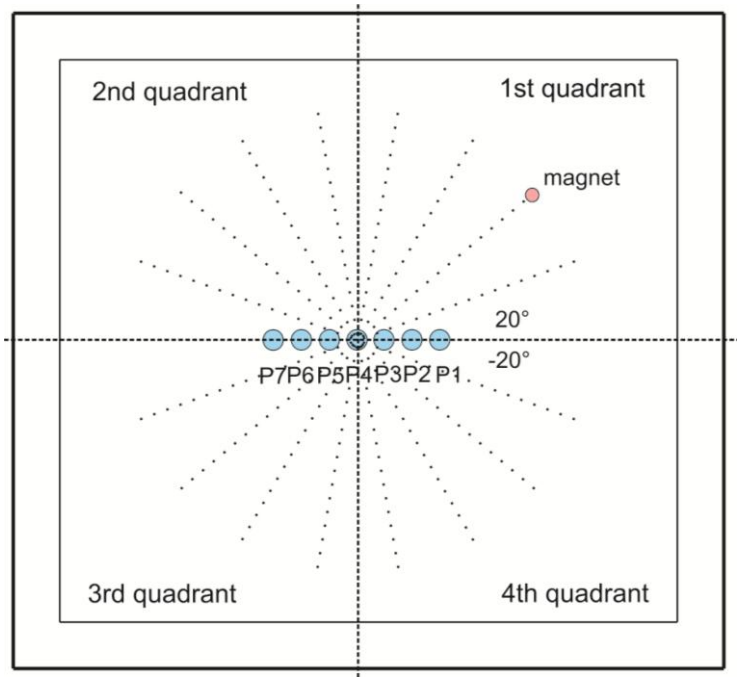

Figure 3.12 Measurements when magnets are at different locations on the plate

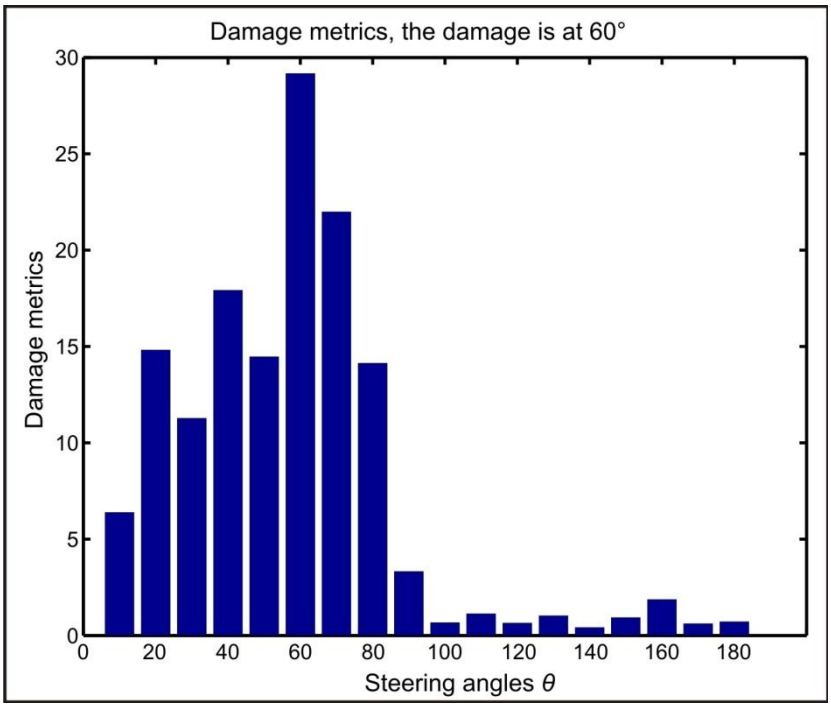

Figure 3.13 A comparison of DMs when the damage is located at 60°

Figure 3.13 illustrates the DMs with cross transfer functions in the damaged state when the magnets are located at 60°. It can be seen that the DMs at 60° and 70° are relatively large. The largest one is at 60° where the damage is located. The DMs from 90° to 180° are quite small, which means that the cross transfer functions do not change significantly before and after damage is located.

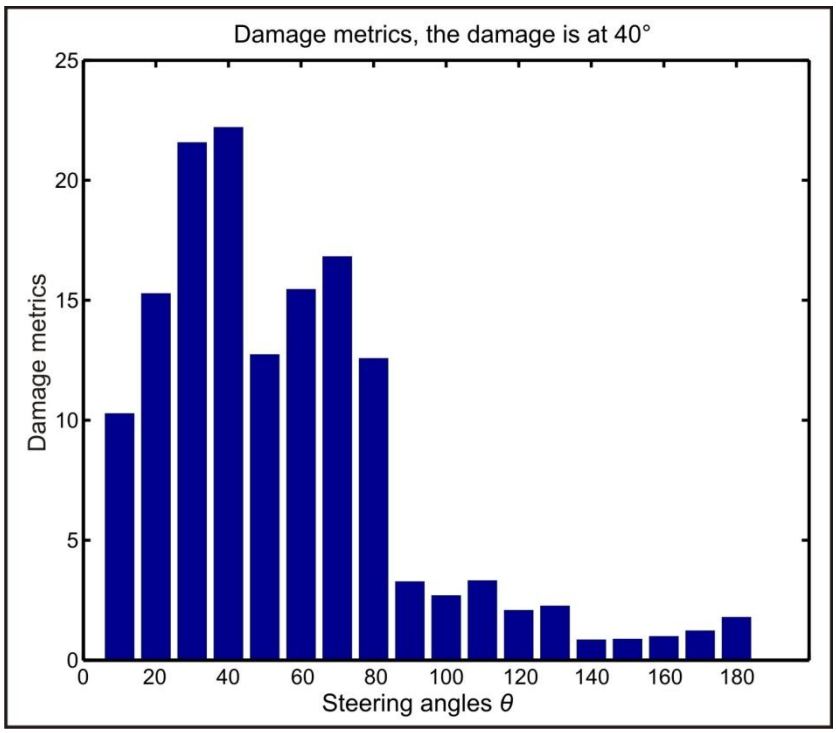

Figure 3.14 A comparison of DMs when the damage is located at 40°

Figure 3.14 is an example of DMs with cross transfer functions, when the damage is at 40°. This diagram shows that the DMs at 30° and 40° are relatively large. The largest DM is where the damage is located at 40°. The DMs from 90° to 180° are quite small. This means that the cross transfer functions do not change a great deal.

Both Figures above show that the DMs using cross transfer function method in the 1-D array are well-directed and are essentially coincident with the location of the damage. However, the DMs close to 60° in Figure 3.13 or 40° in Figure 3.14 are relatively large. This indicates that there are sidelobes, as were shown in the simulation of beamforming by SEM, see Figures 3.6 and 3.7.

3.3.3 Experiment - cross transfer function method in nonuniform phased array with Dolph-Chebyshev Distribution

In the nonuniform case, the weights of PZTs are not identical, the weighting factors are given to the inputs of each PZT, see Eq.3.19 and Eq.3.20. The Dolph-Chebyshev Distribution method (see section 3.2) is chosen to calculate the weighting factors in this application of the cross transfer method to reduce the side lobes.

In the following experiment, an aluminium plate bonded with a 1-D array, see Figure 3.12, is used. The same measurement procedure described in section 3.3.2 is implemented. However, to get $\boldsymbol{T_D}$ and $\boldsymbol{T}$ in a nonuniform phased array, the coefficients a_1, a_2, a_3 and a_4, see Eq. 3.20, form a vector with seven elements. Then the transfer function matrices with weighting factors are obtained. The comparisons of the DMs are shown in Figure 3.15 and 3.16.

Figure 3.15 indicates that the DM at 60° is the largest, while the DMs at other angles are significantly smaller. When compared with Figure 3.13, the DMs around 60° are much less than that at 60°, it seems that sidelobes in the phase array with weighting factors are much less than that without weighting factors. For the same effect where damage is present at 40°, see Figure 3.16, the DM at 40° is the largest. The DMs around 40° are much smaller than in Figure 3.14, which is calculated without weightings. In both figures, beamforming is well-directed at the location of the damage. This indicates that weighting factors have a significant effect and improve the directivity of beamforming using the cross transfer function method.

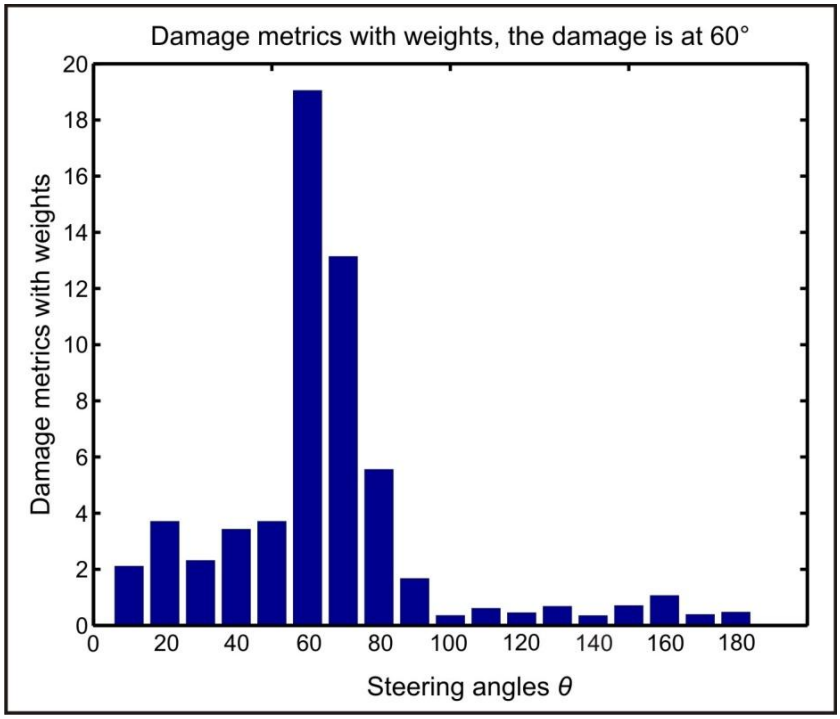

Figure 3.15 A comparison of DMs with weights when the damage is located at 60°

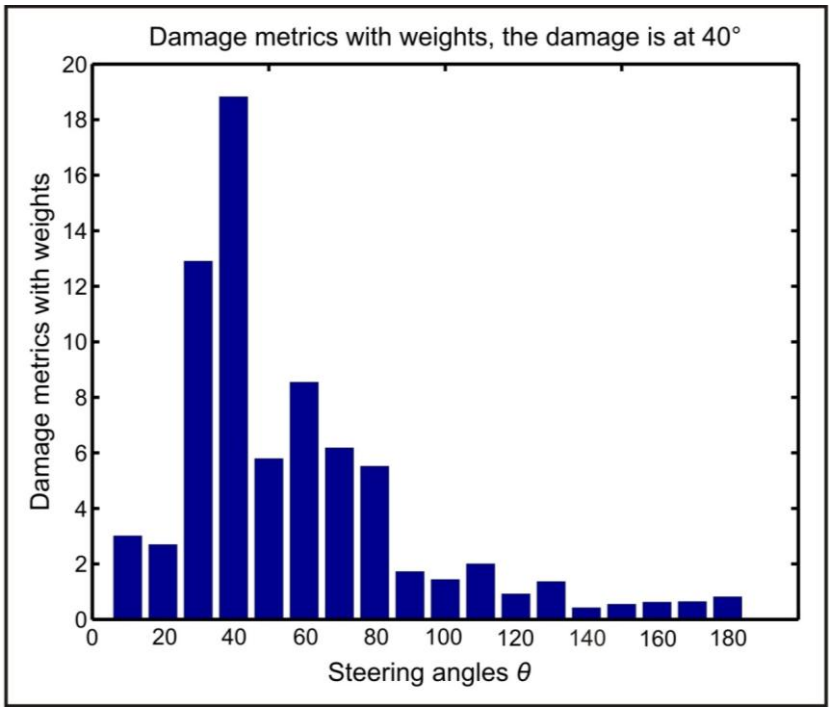

Figure 3.16 A comparison of DMs with weights when the damage is located at 40°

Using polar coordinates, the direction of beamforming when weighting factors are used can better be seen. Figure 3.17 clearly shows the direction at 40° where the damage is located. In addition, there are fewer side lobes. The DMs at the second quadrant (from 90° to 180°) are extremely small. This finding coincides well with the damage location. In addition, the

sidelobes are significantly reduced. It is evident that beamforming using the cross transfer function method, plus weighting factors, provides the advantages.

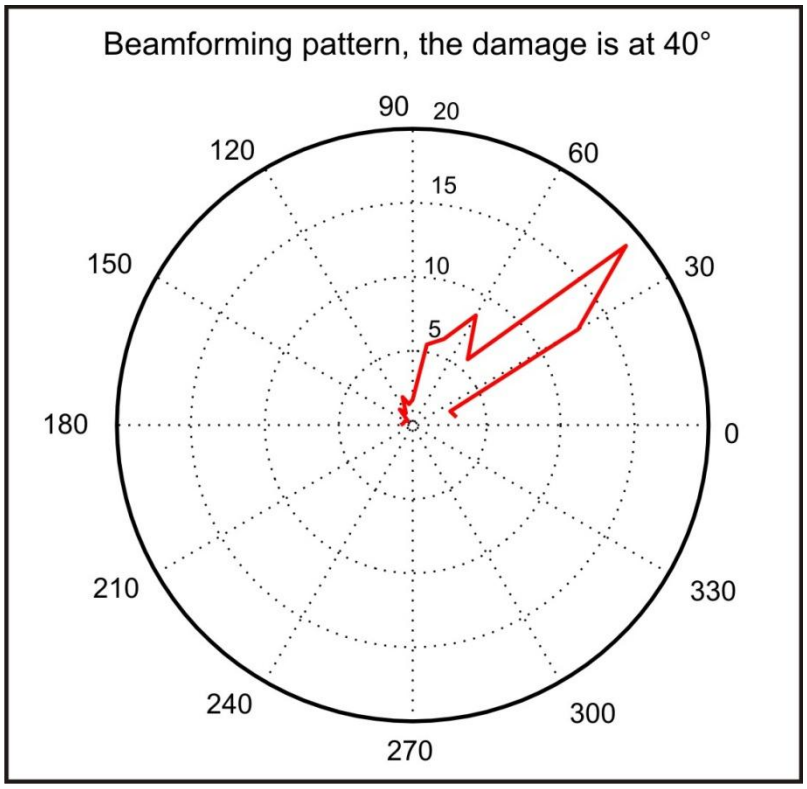

Figure 3.17 DMs with weights in polar coordinate

3.3.4 Experiment: the cross transfer function method in a uniform T- array

In the following experiment, a T-array is used in the investigation of the cross transfer function method. The same aluminium plate with anti-drumming material along the edges and to which 13 PZTs are bonded is used as in the 1-D array experiment.

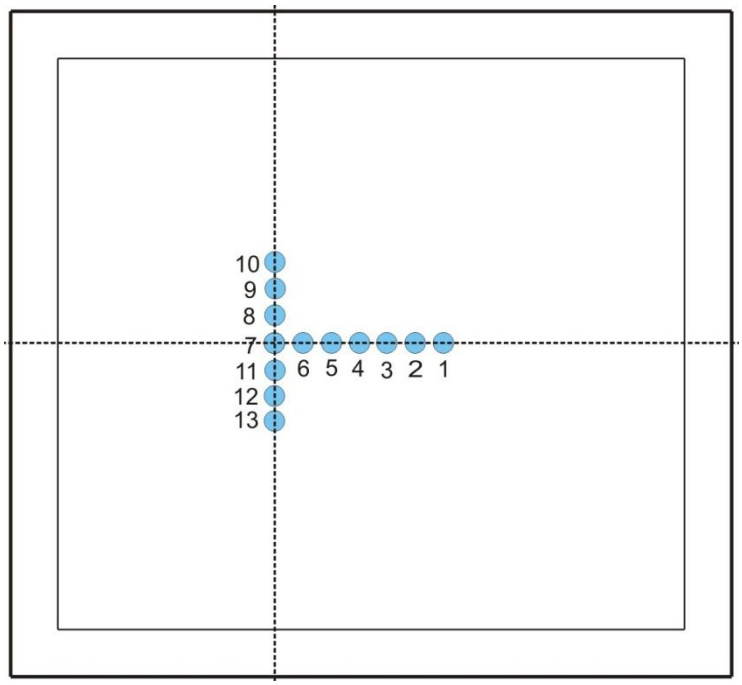

Figure 3.18 PZTs array bonded to the aluminium plate

The measurement procedure is almost the same as in the 1-D array experiment, see section 3.3.2. After compiling all the measured data, the cross transfer functions matrix $\boldsymbol{T_D}$, that is in a damaged state and $\boldsymbol{T}$ that is in an undamaged state, are obtained, see section 3.1. In both $\boldsymbol{T_D}$ and $\boldsymbol{T}$, the phase delay φ which depends on the steering angle θ is included, see Eq. 3.9. As in sections 3.3.2 and 3.3.3, θ takes the values 0, π/18, π/9, π/6... 17π/18 and π, respectively - altogether 18 different angles of arc. After the experiment, $\boldsymbol{T_D}$ and $\boldsymbol{T}$ respectively are compared at each steering angle. By using the Difference Damage Metrics Method (in section 2.2.3), DMs are obtained.

Table 3.1 shows the order in which the input signals are excited relative to each of the PZTs in the experiment. At time T_0, P7 (the reference PZT), is excited by an input signal. After time delay t_1, at time T_1, P6, P8 and P11 are excited. After time delay t_2, at time T_2, P5, P9 and P12 are excited. After time delay t_3, at time T_3, P4, P10 and P13 are excited. After time delay t_4, at time T_4, P3 is excited. Afterwards, P2 is excited at time T_5. Finally, P1 is excited at time T_6. While the PZTs are excited as actuators as described above, the outputs of the other PZTs are measured.

	T_0	T_1	T_2	T_3	T_4	T_5	T_6
x array	P7	P6	P5	P4	P3	P2	P1
y array		P8, P11	P9, P12	P10, P13			

Table 3.1 The exciting orders in T-array

The PZTs in the T-array can be excited in different orders. For example in Table 3.2, at time T_0, P7 is excited first. After time delay t_1 at time T_1, P6 and P8 are excited. After time delay t_2 at time T_2, P5 and P9 are excited. After time delay t_3 at time T_3, P4 and P10 are excited, and so on.

	T_0	T_1	T_2	T_3	T_4	T_5	T_6
x array	P7	P6	P5	P4	P3	P2	P1
y array		P8	P9	P10	P11	P12	P13

Table 3.2 Another exciting order

Table 3.1 is shown as an example in the experiment. The measurements are taken in undamaged and damaged states respectively. In the damaged states, the damage is located at both 40° and 60°. Figures 3.19 and 3.20 show the results of the experiment with DMs in polar coordinates. As in the beamforming simulation, the main and side lobes cannot be clearly distinguished.

In Figure 3.19, there are lobes at approximate 40°. However, there are also lobes at 90° and 155°. In Figure 3.20, the lobes between about 45° and 60° are distinct, while the lobes at around 90° are not distinct, as in Figure 3.19, but there are still lobes between 130° and 145°, as well as between 160° and 170°.

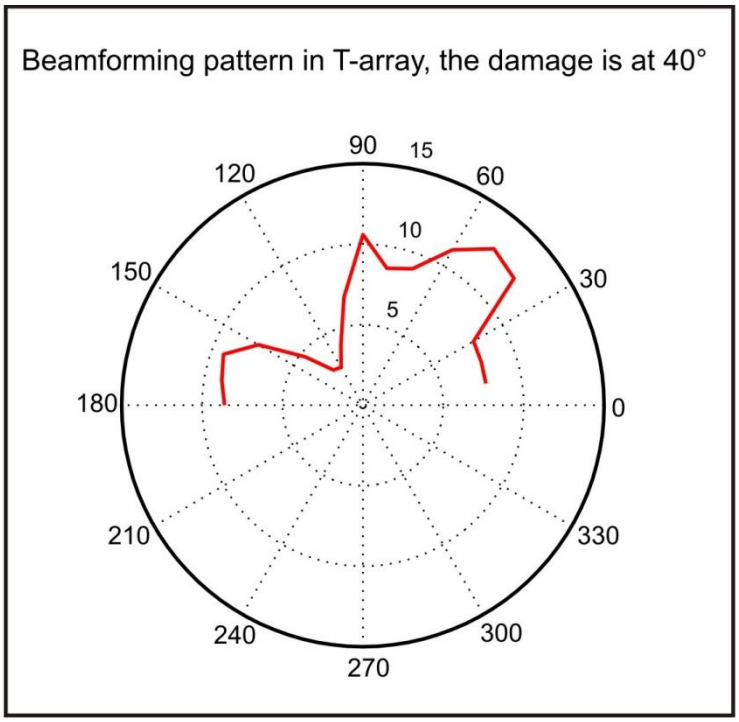

Figure 3.19 DMs in T-array in polar coordinate, when the damage is located at 40°

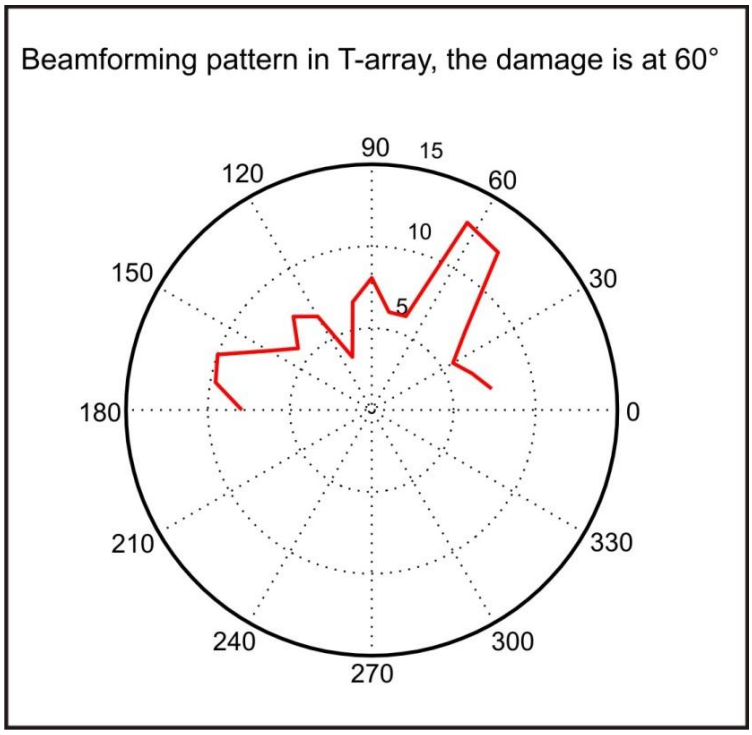

Figure 3.20 DMs in T-array in polar coordinate, when damage is located at 60°

From the simulations and experiments described above it can be seen that the cross transfer function method used in the experiments of a 1-D array supports beamforming and correctly detects the location of the damage. This supports the findings of the beamforming simulation by SEM in 1-D array. In addition, when the weighting factors are added to the cross transfer function matrix, the beamforming of the 1-D array is improved. However, in both experiments and simulations, the beamfoming in the T-array is not well directed. There are no prominent, clearly identifiable main lobes. In the T-array, the PZTs in *y* direction strongly influence the direction of wave propagation. Changing the size and number of the PZTs could be considered for future investigation.

4 Self-diagnosis of Piezoelectric Elements

In real-world applications of SHM, such as in aviation, wind power and pipe lines etc., any changes in environmental or operational conditions (temperature or loads etc.) complicate the SHM process and also make the piezoelectric elements in SHM system work less efficiently. If a SHM system can overcome changes to the environment, condition-based maintenance could replace scheduled maintenance to reduce maintenance costs. Each application of a SHM system not only implements the ability to assess damage, but is also extremely reliable. To keep false alarms to a minimum, it is important to devote further attention to the subject of diagnosing piezoelectric elements bonded to the detected structure and compensating for external influences.

If piezoelectric elements do not produce any meaningful output, or they do not reasonably respond to input signals, it is obvious that they are defunct. However, if a small fracture within a piezoelectric element occurs, or a partial debonding takes place, the piezoelectric element may still produce sufficient performance to generate distorted signals, leading to a false indication of the structure state. By comparing the current outputs of a piezoelectric element to baseline outputs and using data evaluation, it can be determined whether or not the bonded piezoelectric element is in a healthy state. This process is called self-diagnosis of piezoelectric elements. In this section of the work, self-diagnosis is presented and is implemented using the EMI method. Since temperature has a strong influence on the outputs of a piezoelectric element, a method has been found to distinguish the influence of temperature and damage to a piezoelectric element.

4.1 Fundamentals of Self-diagnosis by EMI

In a SHM system, small and thin piezoelectric elements are bonded to the structure. These permanently attached elements are used to evaluate the state of the structure. Therefore, it is important to prove that the piezoelectric patches are not degraded or damaged before they are used to monitor the health of the structure. This is the self-diagnosis process. For this purpose, in [Park 2006] and [Overly 2007] , the coupled electro-mechanical (E/M) behaviour of the bonded piezoelectric element was analysed by utilizing the slope of the imaginary part of E/M admittance (susceptance). Both investigations showed that the E/M admittance of a bonded piezoelectric element was influenced strongly by damage to the element itself or the effects of

the damage to the bonded layers. The techniques used in both papers above follow the concept of the EMI method, see section 2.2.

Self-diagnosis by EMI is a process that detects changes to the capacitive value of piezoelectric materials. These changes are manifested in the imaginary part of the E/M admittance. As described in section 2.2.1, admittance is defined as the proportion of the resulting current to energizing voltage. Under a free-free boundary condition the following relation is given, [Sirohi 2000]:

$$Y_{free} = \frac{I}{V} = i\omega \frac{w_p l_p}{h_p} (\varepsilon_{33}^T (1 - i\delta)) \tag{4.1}$$

Where V is the applied voltage, I is the current, w_p, l_p and h_p are the width, length and thickness of the piezoelectric element, δ is the dielectric loss, ε_{33}^T is the dielectric constant of the piezoelectric element.

When a piezoelectric element is surface-bonded to a structure, its admittance is a combined function of the mechanical impedances of the structure, Z_s, and the piezoelectric element, Z_p, see Eq. 2.8, Eq. 2.7 and Eq. 2.9. It can be seen that changes of the parameters (w_p, l_p, h_p, $\widehat{Y}_p^E$, ε_{33}, d_{31}) clearly influence the imaginary part of admittance, Y. These parameters decide the properties of the piezoelectric element. When breakage or degradation of a piezoelectric element occurs, these properties are changed. Therefore, the basic idea of the self-diagnosis of a bonded piezoelectric element by using EMI is to monitor the changes of the imaginary part of the E/M admittance.

As introduced in 2.1, lead-zirconate-titanate mixed ceramics (PZT) is one of the two kinds of materials which are most widely manufactured. In this investigation, PI Ceramic C255 is applied in the detected structure. In practice, the linear part of a voltage-strain curve of piezoceramic elements is used for sensing. As mentioned in [Schulz 2003], all piezoceramic materials have operating limits associated with temperature and voltage. The voltage output from the piezoceramic element declines as the temperature increases. For high voltage, the behaviour of the piezoceramic element becomes nonlinear.

In [Park 2006], the EMI method was used to investigate the behaviour of free and bonded PZT. The E/M admittances of PZTs are measured in different cases, see Figure 4.1.

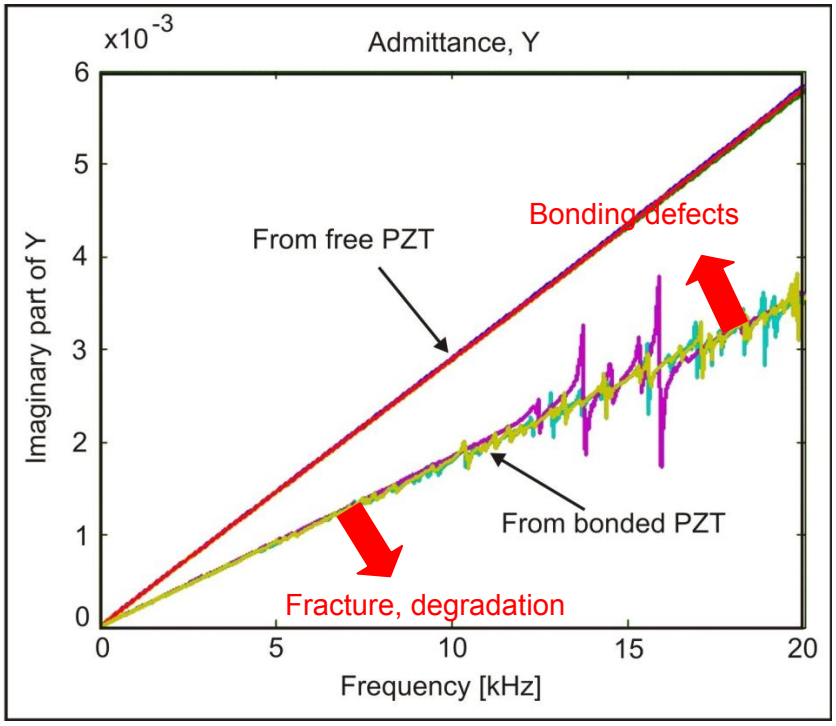

Figure 4.1 E/M Admittance measurement from PZTs under free and bonded conditions, [Park 2006]

Figure 4.1 illustrates the remarkable downward shifting effect of slope when the PZTs are bonded to the surface of a structure. The slope of the imaginary part of admittance (susceptance) from bonded PZTs is reduced compared to the slope measured from free PZTs (the red line). The figure above demonstrates that breakage, the degradation of PZT or bonding defects would all affect the measured admittance. Bonding defects would cause the upward shift of the slope, whereas the breakage or degradation of PZTs would decrease the slope, see the two red arrows in the figure. Figure 4.1 demonstrates that by monitoring the susceptance of PZTs, changes to the properties of the elements and the integrity of the bonding layer can be assessed.

In addition, changes in environmental conditions (temperature, humidity, wind, etc.) are known to have considerable effects on the output of a piezoelectric element. These changes may lead to unreliable results and mask real damage in the piezoelectric element. Therefore, the environmental changes- temperature in particular - that affect a piezoelectric element must be taken into account. For this reason, feature extraction is utilized to convert the measured E/M admittances data into new data with lower dimensions, in which the important information from the original data is still retained. As a statistical technique Principal Components

Analysis (PCA) in SHM has been extensively applied to evaluate measured data for dimensionality studies and remove the influence of environmental factors. This technique is used to find patterns in high dimension data. The goal is to re-express the original measured data in such a way that new data are arranged along directions of maximal variance and minimal redundancy, [Köhler 2005].

In PCA we are trying to find the axes with maximum variances where the data is most spread (within a class, since PCA treats the whole data set as one class). The advantage of this technique is that environmental parameters are taken into account as embedded variables, which effectively eliminates environmental factors from the process of damage detection.

The process of self-diagnosis is illustrated in Figure 4.2. The current data is measured using different temperatures. Baseline data is measured at normal temperature as reference data, when the structure system is in an undamaged state. After this, the spectra of E/M admittance in undamaged and damaged states are calculated, see Eq. 2.13. Then feature extraction is carried out.

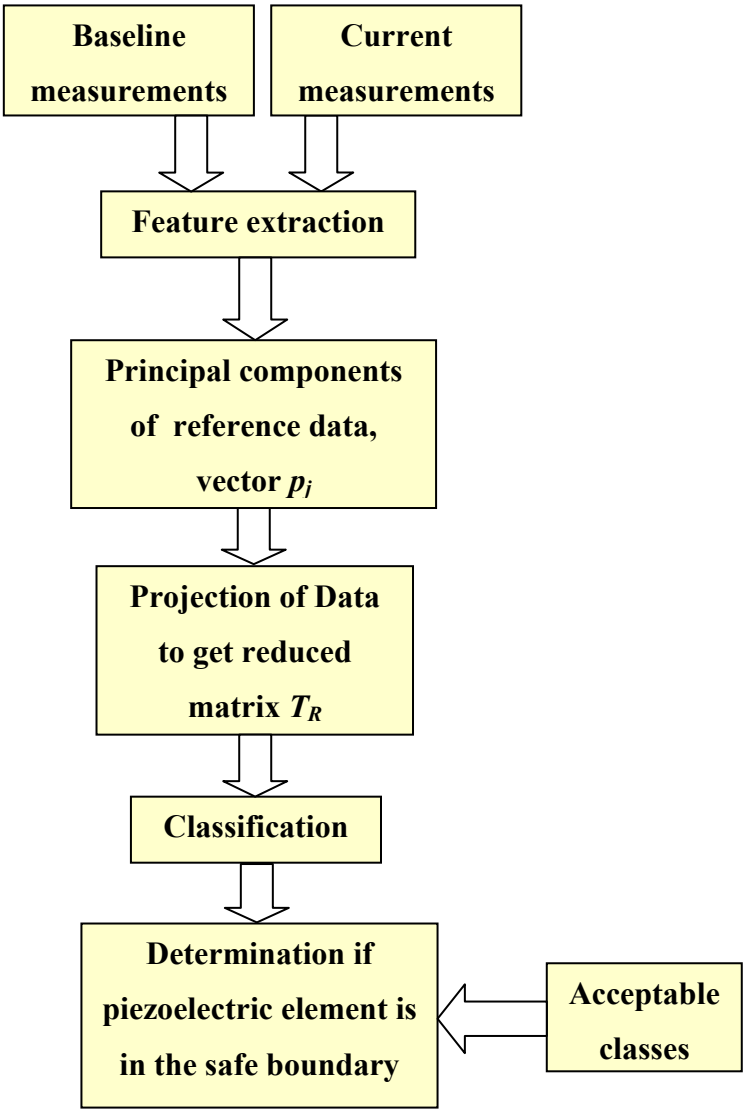

Figure 4.2 Flowchart of self-diagnosis of piezoelectric element

The matrix $\boldsymbol{X}$ (m x n) consists of features, n is the number of features and m is the number of measurements, see Eq. 4.2.

$$\boldsymbol{X} = \begin{bmatrix} x_{11} & x_{12} & . & . & . & . & x_{1n} \\ x_{21} & x_{22} & . & . & . & . & x_{2n} \\ x_{31} & x_{32} & . & . & . & . & x_{3n} \\ . & . & . & . & . & . & . \\ . & . & . & . & . & . & . \\ . & . & . & . & . & . & . \\ x_{m1} & x_{m2} & . & . & . & . & x_{mn} \end{bmatrix} \tag{4.2}$$

The *n* features are calculated from the measured E/M impedances and admittances of current data. To obtain the principal components, the covariance matrix of $\boldsymbol{X}$ (reference data) is utilized, from which the eigenvalues and corresponding eigenvectors can be obtained.

$$(\boldsymbol{X}_{\boldsymbol{COV}} - \boldsymbol{\Lambda}_j \boldsymbol{I})\boldsymbol{p}_j = 0 \tag{4.3}$$

Where $\boldsymbol{X}_{\boldsymbol{COV}}$ (*n* x *n*) is the covariance matrix of $\boldsymbol{X}$, and $\boldsymbol{\Lambda}_{\boldsymbol{j}}$ is the eigenvalue of $\boldsymbol{X}_{\boldsymbol{COV}}$. $\boldsymbol{p}_{\boldsymbol{j}}$ (n x 1) is the eigenvectors, *j=1,2,..., n*.

We started with the goal to reduce the dimensionality of our feature space, i.e., projecting the feature space via PCA onto a smaller subspace, where the eigenvectors will form the axes of this new feature subspace. However, the eigenvectors only define the directions of the new axis, since they have all the same unit length 1. Eigenvalues decide the importance. The importance of each principal component can be calculated with Eq. 4.4.

$$\boldsymbol{Im}_j = \frac{\boldsymbol{\Lambda}_j}{\sum \boldsymbol{\Lambda}_j} 100\% \tag{4.4}$$

From Eq. 4.4, it can be seen that the largest eigenvalue gets the highest importance value among all the eigenvalues. The eigenvectors from the important eigenvalues are chosen as principal components to obtain vector $\boldsymbol{p}_{\boldsymbol{r}}$ (*n* x *1*), matrix $\boldsymbol{P}$ (*n* x *r*) in order to calculate the reduced matrix, $\boldsymbol{T}_{\boldsymbol{R}}$, see Eq.4.5 and Eq. 4.6, [Köhler 2005].

$$\boldsymbol{P} = \begin{bmatrix} p_1 & p_2 & . & . & p_r \end{bmatrix} \tag{4.5}$$

$$\boldsymbol{T}_{\boldsymbol{R}} = \boldsymbol{X}\,\boldsymbol{P} \tag{4.6}$$

Eq. 4.6 transforms the $\boldsymbol{X}$ (*m* x *n*) onto a new subspace, the reduced matrix $\boldsymbol{T}_{\boldsymbol{R}}$ (*m* x *r*). Matrix $\boldsymbol{P}$ (*n* x *r*) is from eingenvectors $\boldsymbol{p}_{\boldsymbol{j}}$, it shows the data pattern along which the properties of the bonded piezoelectric element vary. In our application of self-diagnosis in 4.2.1, only one eigenvalue - the one that has the most importance- is chosen to get the eigenvector as the principal component.

Back to Figure 4.2 after the principal components are determined, classification can be implemented, in which the *k*-means algorithm can be used to differentiate among various different conditions, [Duda 2001].

In self-diagnosis, four classes can be included. They are (a) an undamaged state, (b) defects within the element itself, (c) the debonding of a bonded element from the structure and (d) the degradation of an element or bonding layer. In this work, the main task is to detect if there is a change within the element itself or within the bonding layer and to distinguish damage in the

element itself resulting from the changes of temperature. The states of the bonded elements are not classified.

In section 4.4, two of the damaged scenarios are investigated. One is a defect within a piezoelectric element, the other the degradation of the element.

To determine whether the bonded element is in the healthy state, the damage indicators (*DIs*) and thresholds need to be calculated. *DIs* result from the Euclidean distance.

$$DI = \left\| \boldsymbol{X} - \widehat{\boldsymbol{X}} \right\|^2 \tag{4.7}$$

$$\widehat{\boldsymbol{X}} = \boldsymbol{T_R P}^{\boldsymbol{T}} = \boldsymbol{X P P^T} \tag{4.8}$$

where $\widehat{\boldsymbol{X}}$ is the estimated features of current data, and $\boldsymbol{P}$ is the principal components calculated using baseline data (reference data). Therefore, Eq. 4.7 can be written:

$$DI = \left\| \boldsymbol{X}(\boldsymbol{I} - \boldsymbol{P P^T}) \right\|^2 \tag{4.9}$$

Eq. 4.10 indicates the threshold line for the *DIs*, in which TUL is the upper line threshold, *DI* is the mean value of all *DIs*, and σ is the standard deviation of *DIs*.

$$TUL = DI + 3\sigma \tag{4.10}$$

If a *DI* is beyond the threshold it can be determined that defects or degradation of the bonded piezoelectric element have occurred.

It is known that the spectra of E/M impedances and admittances are not smooth curves. Therefore, when the features are selected, curve fitting first has to be implemented. The main idea of curve fitting is to construct a curve, or a mathematical function which has the best fit to the series of data points. Curve fitting can involve interpolation, where an exact fit to the data is required. Here, polynomial interpolation is used to approximate the curves and is implemented in Matlab.

The interpolation polynomial is in the form:

$$s(x) = a_q x^q + a_{q-1} x^{q-1} + \ldots + a_2 x^2 + a_1 \tag{4.11}$$

in which the coefficients of the polynomial of degree q are chosen that best fit the original data. After a fitting curve is found in the spectra of susceptance and conductance, several

points along the curve are chosen as features. In section 4.2.1, feature definitions are described.

4.2 Self-diagnosis Application in the Experiments

In the following experiments, a SMART Layer transducer with a diameter of 6.35mm (commonly used within Airbus) and with a PI Ceramic C255 (PIC), 10mm diameter, is bonded to an aluminium plate (149mmx149mmx1.5mm), see Figure 4.3. The transducer is covered by a topcoat and an epoxy-based layer. Two frequency ranges of the input signals are applied respectively to excite the transducer, namely 200kHz to 750kHz and 200 kHz to 800kHz. The input signal is given for 500 msec. The measurement follows the EMI method, see section 2.2.2. The output voltages are measured by an oscilloscope. By using the output and input voltages, the spectra of admittances are obtained, see Eq. 2.13.

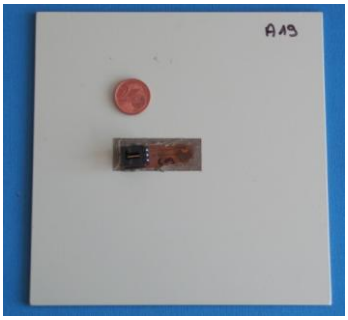

Figure 4.3 The specimen bonded with PI Ceramic C255

The spectra of conductances and susceptances are shown in Figure 4.4 and Figure 4.5. The blue line is the spectrum of conductance, the real part of the admittance. The red line is the spectrum of susceptance, the imaginary part of the admittance.

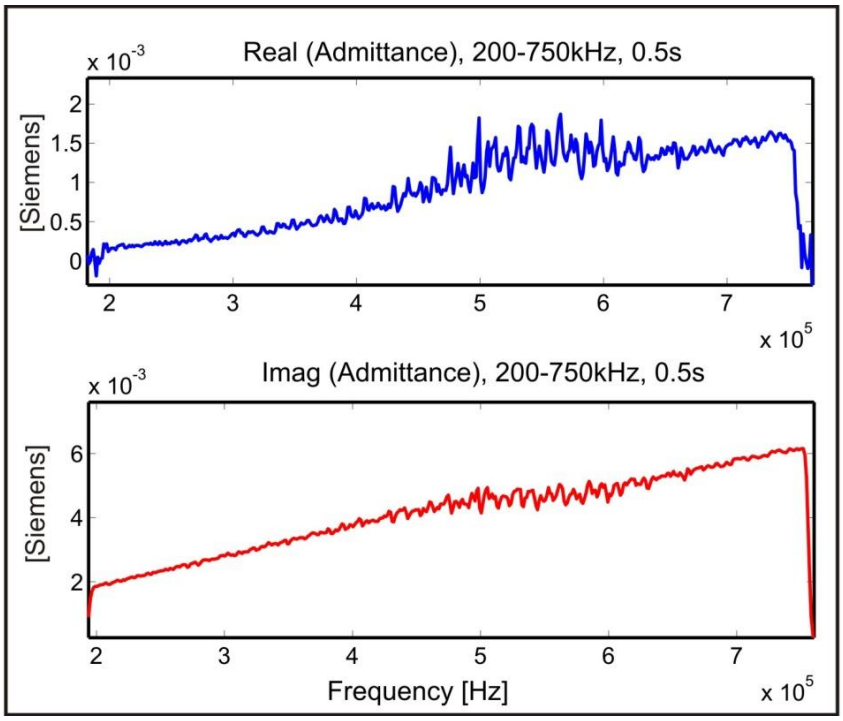

Figure 4.4 The spectra of admittance with resulting from a 200-750 kHz, 500msec input signal

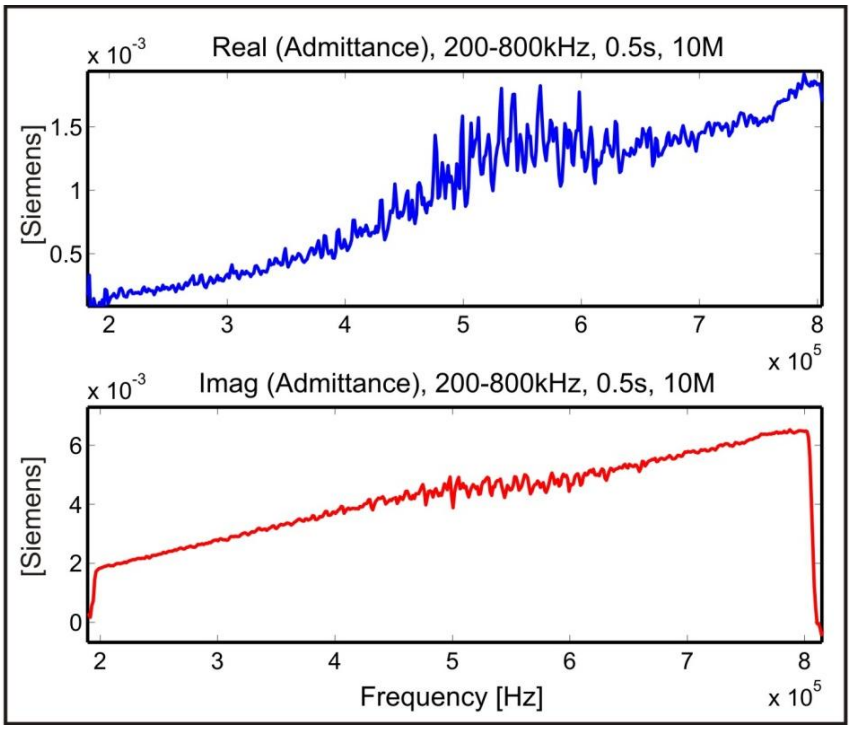

Figure 4.5 The spectra of admittance with resulting from a 200-800 kHz, 500msec input signal

Both of the above figures show that there are distinct peaks between approximately 450kHz and 650kHz, which are the resonant frequencies of the bonded piezoelectric element (PI Ceramic C255). In the following measurements, the frequency range from 200kHz to 800kHz are utilized as input signals.

Due to the strong influence of temperature on the output of a piezoelectric element, temperature as a variable is considered in the investigation of self-diagnosis. This is done in order to distinguish changes to the piezoelectric element itself from changes caused by temperature. Theoretically, the properties of a piezoelectric element, e.g. transverse and extensional strain constants, the planar coupling coefficient and the effective electro-mechanical coupling coefficient change as the temperature changes. In [Schulz 2003], it was concluded that the output of a piezoelectric element decreases, when the temperature is increased. Temperature can also cause degradation of the bonded element.

Figure 4.6 The bonded PICs in a laboratory oven

Figure 4.6 is a laboratory oven in which there are the sample plates bonded with piezoelectric element. In the following experiments, measurements are taken at different temperatures. The spectra of admittances are obtained to show the changes to the output of the bonded piezoelectric element at different temperatures.

4.2.1 Feature definitions in the spectra of EMI admittances

The outputs of piezoelectric element were measured at different temperatures - 20°C, 40°C, 60°C, 80°C and 100°C and the spectra of susceptances and conductances were determined.

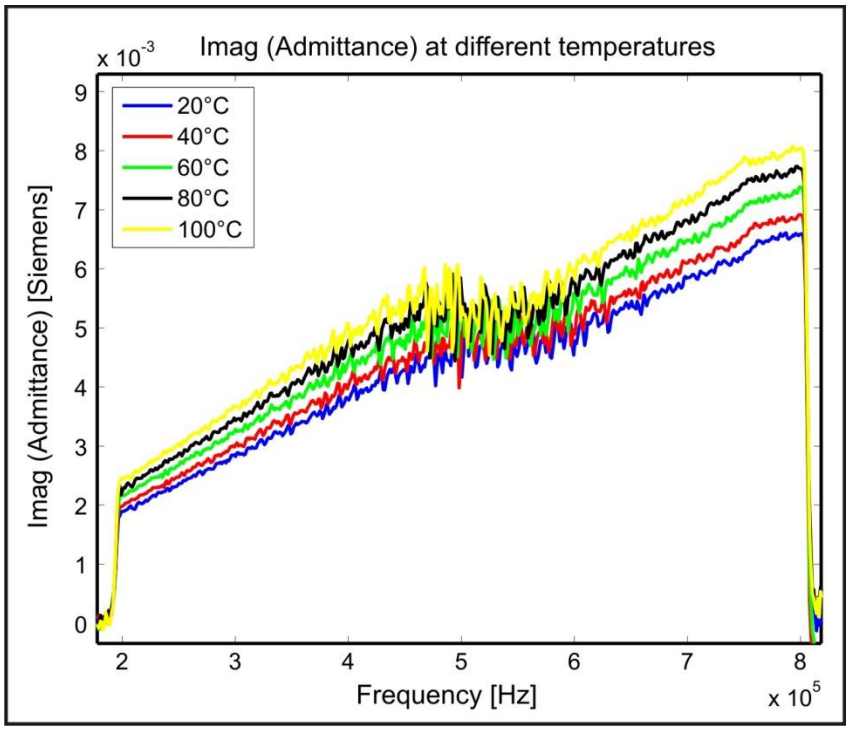

Figure 4.7 The imaginary parts of admittances at different temperatures

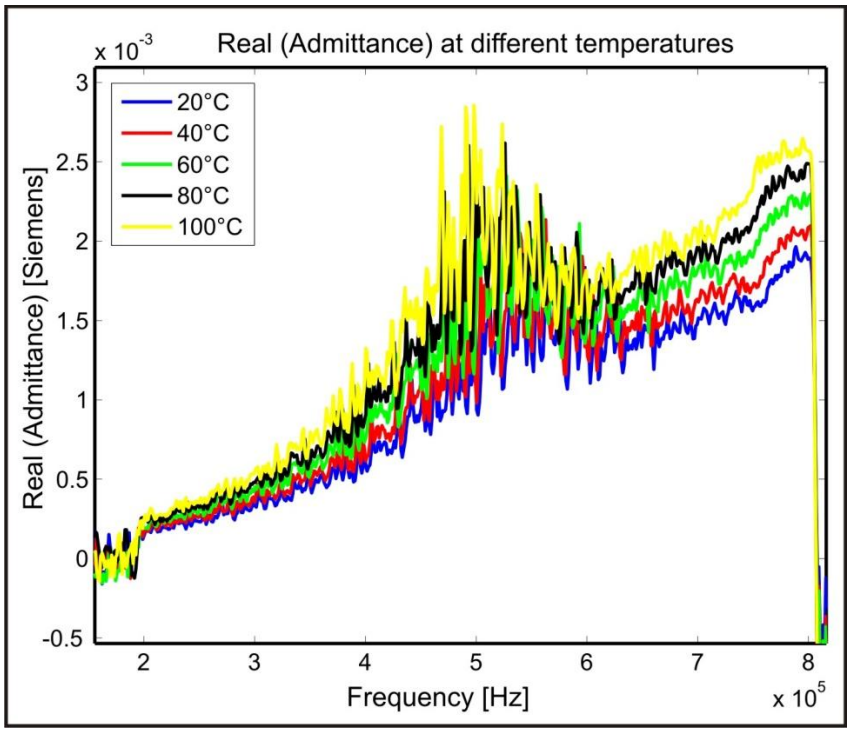

Figure 4.8 The real parts of admittances at different temperatures

In both of the above figures, the resonant frequencies of the bonded piezoelectric element are shown between 450kHz and 650kHz as in Figure 4.5. The slopes of both susceptances and conductances shift upwards as the temperature increases. In both cases, it seems that the upwards shift in the higher frequency (e.g. 650kHz to 800kHz) is greater than the shift in the

lower frequency (e.g., 200kHz to 400kHz), which we expect. It shows that the bonded piezoelectric element is more sensitive to changes of temperature when it is excited by higher frequency input signals.

After measurements were taken at 100°C, the oven was allowed to cool down to 20°C, at which point the output of the bonded PIC was again measured. Figure 4.9 shows the spectra of susceptances at the initial 20° (the blue line) and after it has cooled down to 20° (the red line). Both measurements are almost identical, which illustrates that the properties of both the PI and the bonding layer have not changed after being subjected to a temperature of 100°C high temperature. PIs do not degrade when they operate at 100°C.

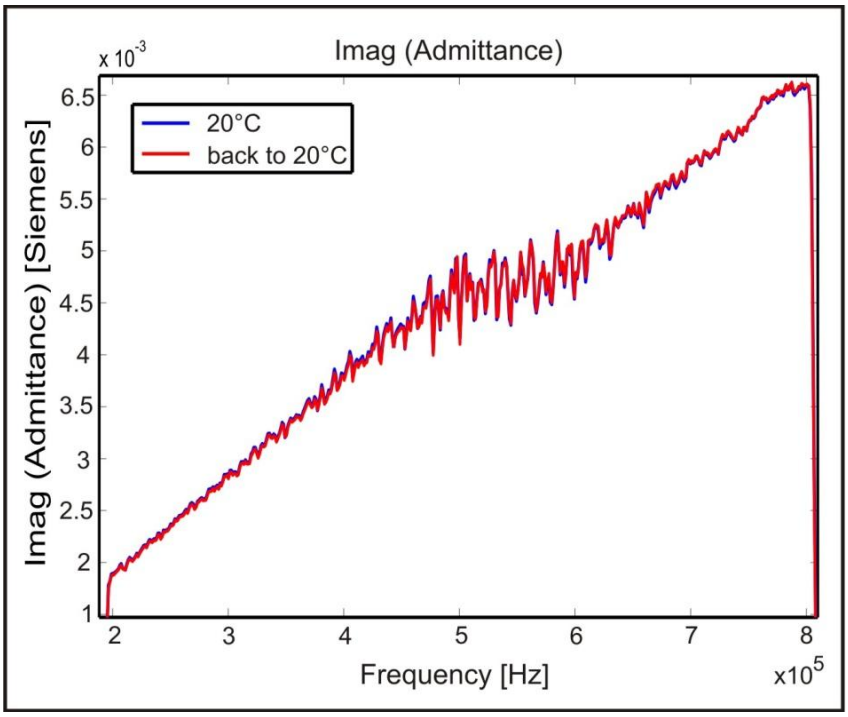

Figure 4.9 The imaginary part of admittance at 20°C and back to 20°C

To implement the feature extraction and PCA in the diagram of section 4.1, see Figure 4.2, curve fitting needs to be carried out using the interpolation polynomials, see section 4.1.

Figure 4.10 and Figure 4.11 show the fitting curves (in red) are approximated by the polynomial of degree 10 ($q=10$), see Eq. 4.11.

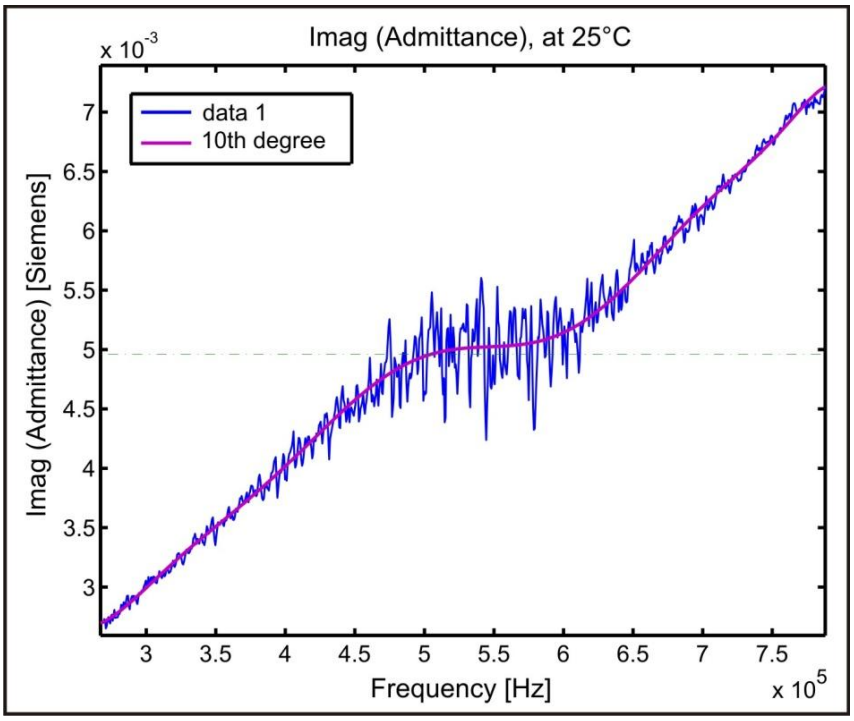

Figure 4.10 The fitting curve on the susceptance

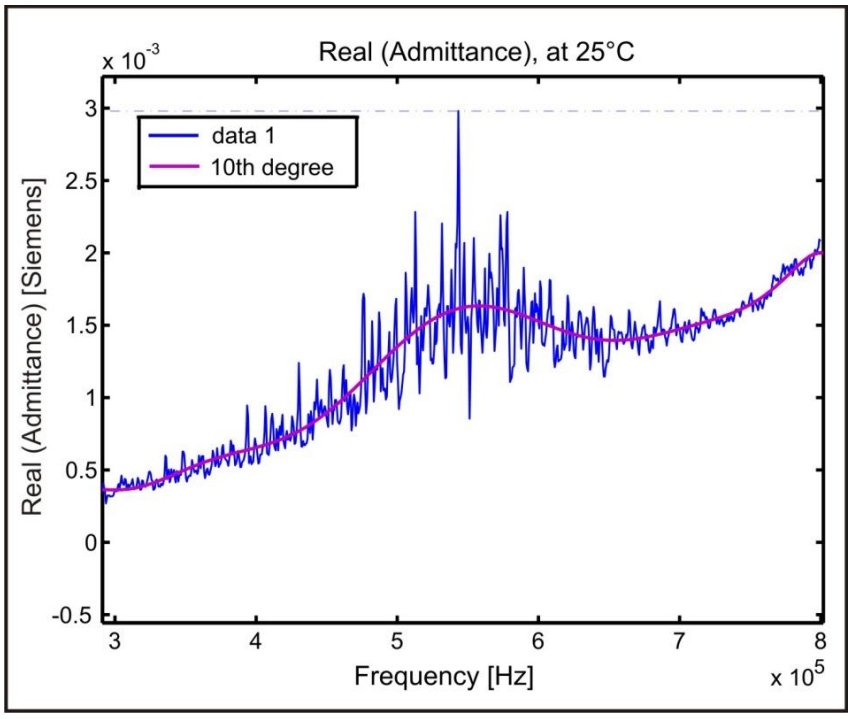

Figure 4.11 The fitting curve on the conductance

Using the fitted curves, 12 features in the spectra of admittances are chosen. These are described in Table 4.1. Figure 4.12 shows the values of the features. In the upper figure, the blue line is the spectrum of susceptance, the imaginary part of admittance, while the red and the green lines are the first and second derivatives of the susceptance respectively. The subplot in Figure 4.12 is the spectrum of the conductance, the real part of admittance. The red point in

the red line is the peak value of the conductance. The blue points are the conductance values at the frequency of inflection points of susceptances.

Feature 1	the frequency of inflection point of susceptance
Feature 2	the inflection point of susceptance
Feature 3	the conductance value at the frequency of inflection point of susceptance
Feature 4	the peak frequency of conductance
Feature 5	the peak value of conductance
Feature 6	the frequency of the inflection point of susceptance
Feature 7	the susceptance vlaue at the frequency of Feature 6
Feature 8	the conductance value at the frequency of Feature 6
Feature 9	the frequency of the other inflection point of susceptance
Feature 10	the susceptance value at the frequency of Feature 9
Feature 11	the conductance value at the frequency of Feature 9
Feature 12	the slope of susceptance

Table 4.1 Features for PCA

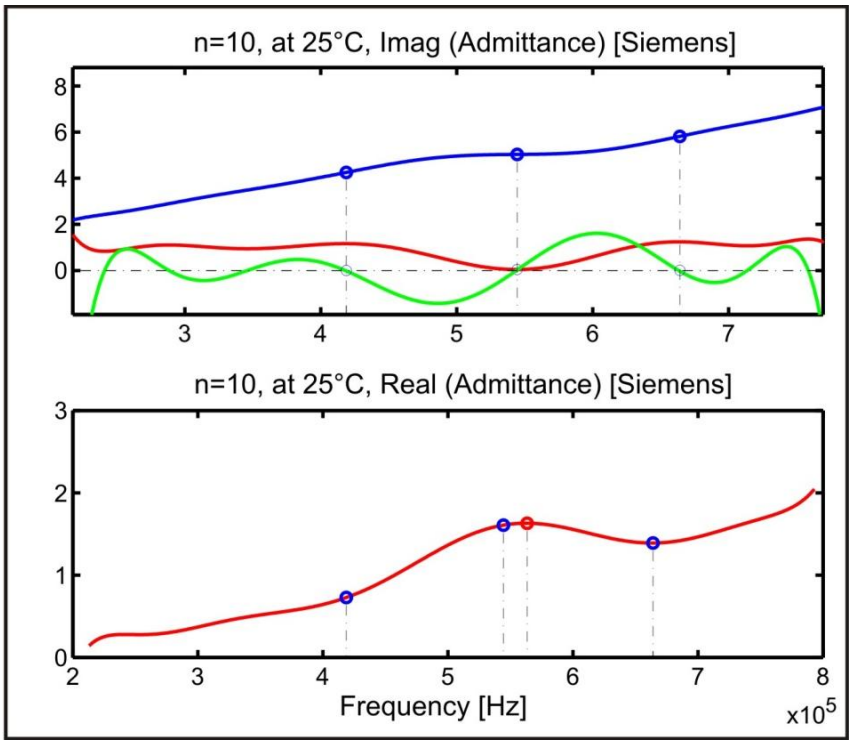

Figure 4.12 The inflections of the imaginary and real parts of admittance

4.2.2 Self-diagnosis in two damage cases

Generally, there are several possible kinds of damage that can affect a piezoelectric element, e.g.: the degradation of the piezoelectric element's properties, the debonding of a piezoelectric element from the structure, the degradation of an adhesive layer and the breakage of a piezoelectric element.

In the following experiments two cases of failure are investigated. One is the degradation of a piezoelectric element as a result of high temperature, the other is the breakage of a piezoelectric element.

Investigation of degradation

The process of degradation is described in Table 4.2. There are 136 measurements in total. Two measurements were taken at 20°C, 30°C, 40°C, 50°C, 60°C, 70°C and 80°C. These are used as reference data.

Four measurements were taken at 10°C intervals from 25°C to 85°C. Five measurements were taken when the sample plate had been kept in the oven at 130°C for 960min. Then the oven's temperature was dropped by 20°C and increased to 85°C. Three measurements were taken at each temperature. After that, five measurements were taken at 130°C. Finally, three measurements were again recorded at each temperature.

T in °C	measurements of baseline data	measurements of current data	measurements after 960min in 130°C	measurements after 1920min in 130°C	measurements after 3840min in 130°C	measurements after 4800min in 130°C
20 (RMT*)	2		5	3	5	3
25		4		3		3
30	2			3		3
35		4		3		3
40	2			3		3
45		4		3		3
50	2			3		3
55		4		3		3
60	2			3		3
65		4		3		3
70	2			3		3
75		4		3		3
80	2			3		3
85		4		3		3

*RMT: Room Temperature

Table 4.2 Measurements at high temperatures

The features of the data above are calculated to obtain the matrix the $\boldsymbol{X}$, see Eq. 4.2. The eigenvectors and eigenvalues of covariance matrix of $\boldsymbol{X}$ are calculated by Eq. 4.3, by which the principal components ($\boldsymbol{p_j}$, $j=1,2,...,\ n$) are determined. Afterwards, the importance of each principal component is calculated using Eq. 4.4 in section 4.1. Figure 4.13 shows the importance of all 12 principal components. The two yellow bars show high importance.

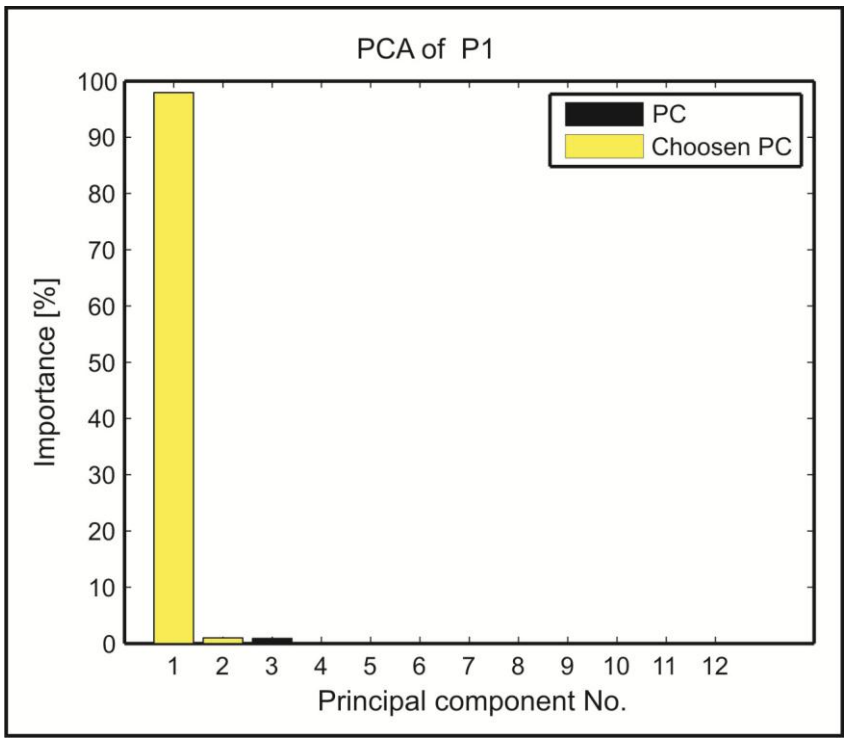

Figure 4.13 The importance of principle components

The principal component with the largest importance is chosen to obtain the matrix $\boldsymbol{P}$ (n x r), see Eq. 4.5 in section 4.1. By Eq. 4.6, the reduced matrix $\boldsymbol{T_R}$ (m x r) is calculated. To obtain Damage Indicators (*DIs*), Eq. 4.9 is utilized. The threshold is obtained using Eq. 4.10. *DIs* of each measurement as shown in Figure 4.14 and Figure 4.15. The broken red line is the threshold. The green points are obtained from reference data, the black points are from current data. Figure 4.14 shows that the *DIs* exceed the threshold after the 43rd measurement (after 960 min in 130°C). This means that the piezoelectric element is in a degraded state after the 43rd measurement due to the high temperature (130°C). Figure 4.15 is the zoom of *DIs* calculated using the first *30th* measurements.

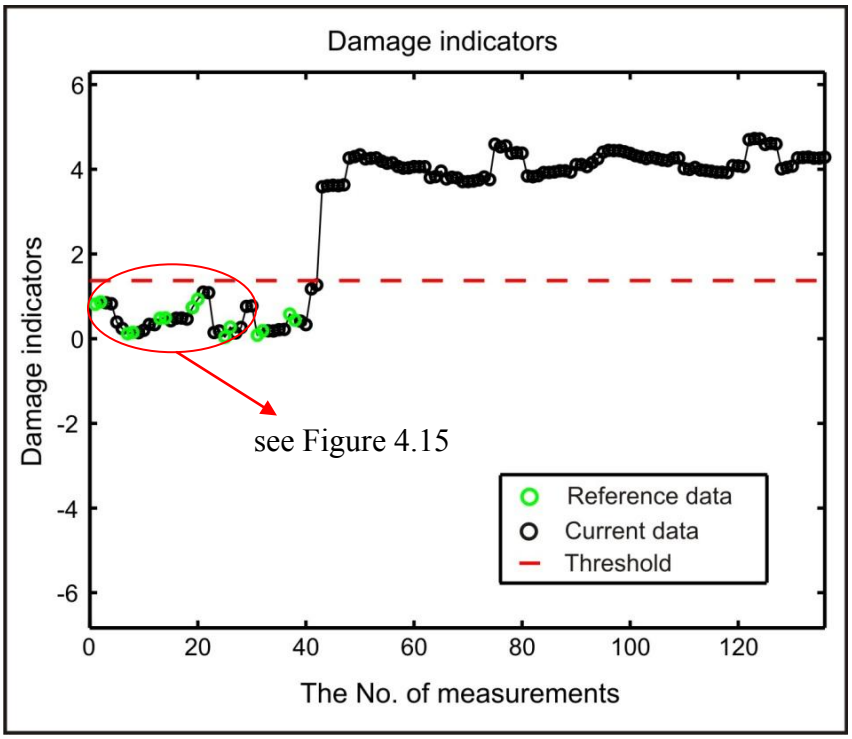

Figure 4.14 The damage indicator of degradation

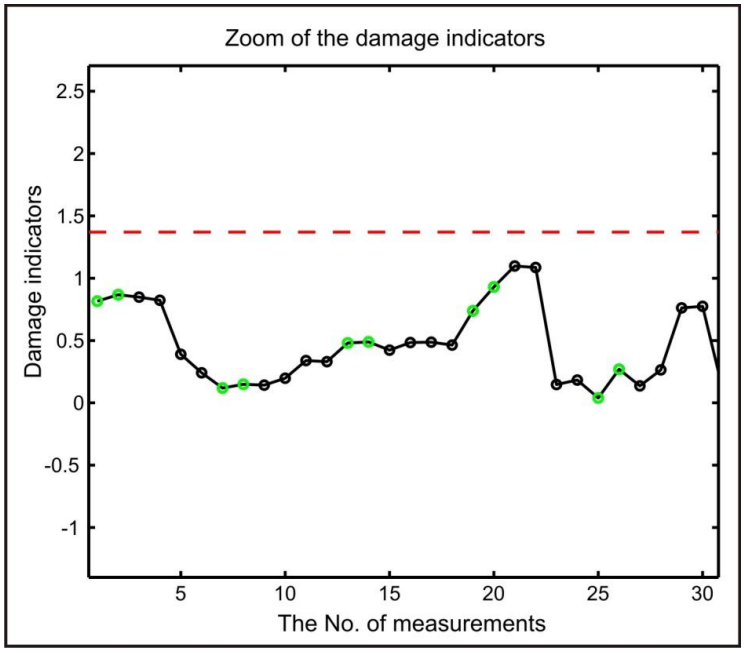

Figure 4.15 The zoom part of Figure 4.14

Investigation of breakage

Now, we come to the breakage. After the baseline data is recorded, the breakage is artificially created in the bonded piezoelectric element, see Figure 4.16. The outputs in the damaged state are measured at different temperatures, see Table 4.3.

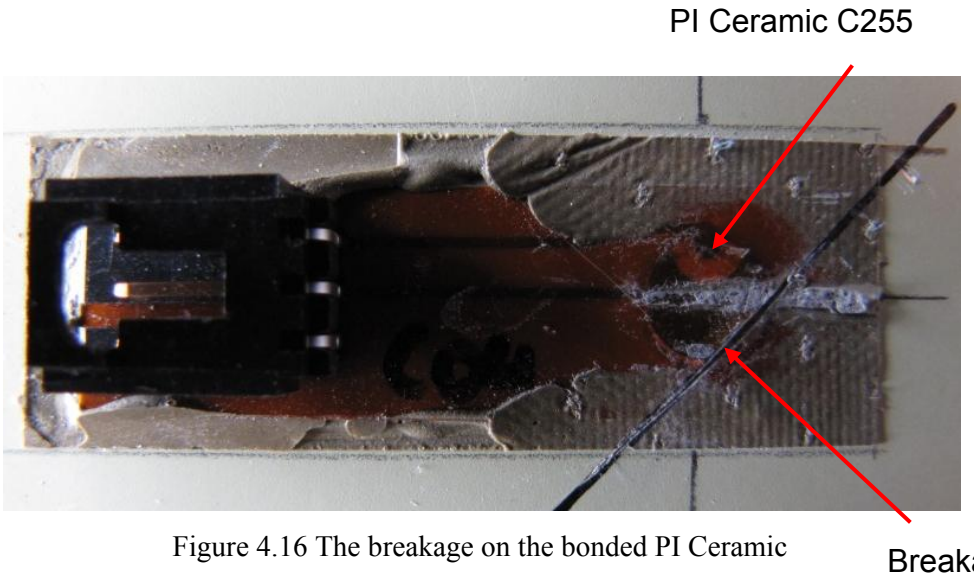

Figure 4.16 The breakage on the bonded PI Ceramic

T in °C	measurements of baseline data	measurements of current data	measurements after the artificial breakage
20 (RMT*)	2		3
25		4	3
30	2		3
35		4	3
40	2		3
45		4	3
50	2		3
55		4	3
60	2		3
65		4	3
70	2		3
75		4	3
80	2		3
85		4	3

*RMT: Room Temperature

Table 4.3 Measurement series of breakage experiment

There are 136 measurements in total. Two measurements were taken at each temperature, 20°C, 30°C, 40°C, 50°C, 60°C, 70°C and 80°C, as reference data. Four measurements were

taken at each temperature, 25°C, 35°C, 45°C, 55°C, 65°C, 75°C and 85°C, and three measurements at each temperature were taken after the breakage had occurred as current data.

As in the degradation experiment, eigenvalues and eigenvectors are calculated from the covariance matrix of $\boldsymbol{X}$. Afterwards, the principal components are determined. A matrix with reduced dimensions, $\boldsymbol{T_R}$ is produced. Using $\boldsymbol{X}$ and $\boldsymbol{T_R}$, *DIs* are calculated and the threshold is decided. The results are shown in Figure 4.17 and Figure 4.18. The *DIs* after breakage are shown in the figures. The broken red line is the threshold. The green points are the *DIs* obtained from reference data, the black points are from current data. Figure 4.18 is the zoom of the *DIs* from the first 42 measurements.

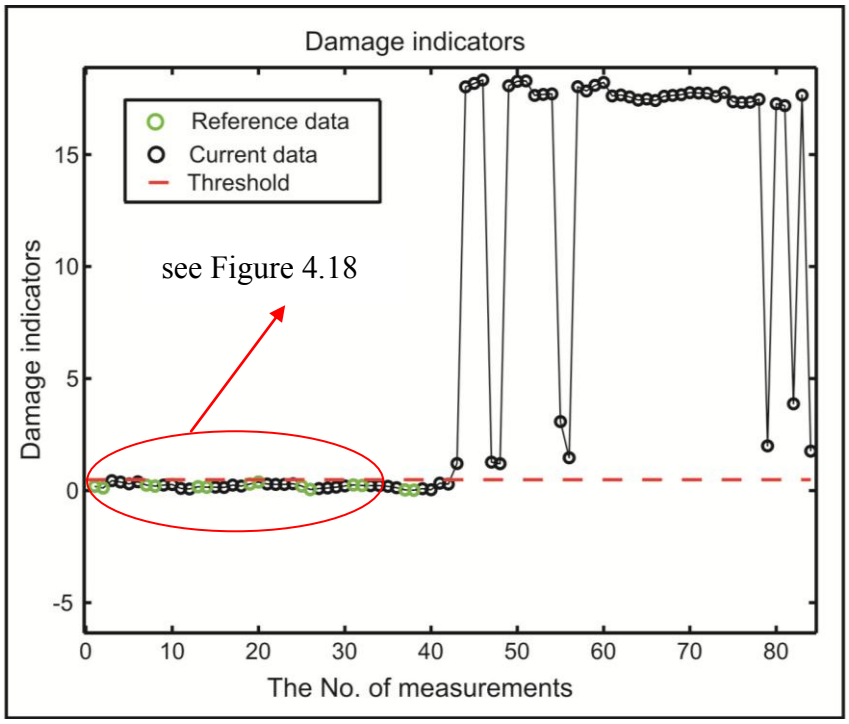

Figure 4.17 Damage indicator of breakage case

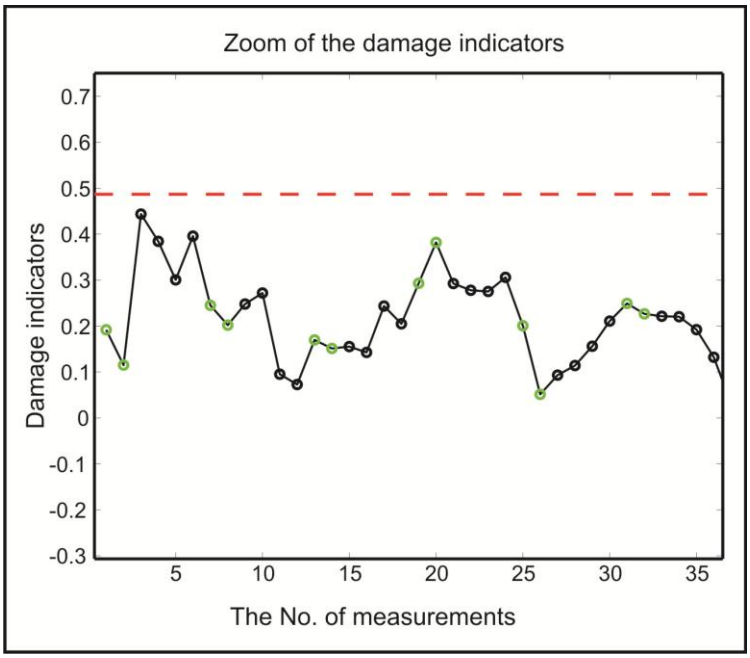

Figure 4.18 The zoom of part of Figure 4.17

Figure 4.17 indicates that the *DI* values move beyond the threshold after the 42nd measurement and fluctuate strongly, but still stay above the red line. Figure 4.17 illustrates that the changes to the bonded piezoelectric element occur after the 42nd measurement. As shown in Table 4.3, artificial breakage is made to occur at exactly the same time in the experiment. The *DIs* obtained by the self-diagnosis process coincide well with this experiment.

By using the spectra of admittances obtained by the EMI method, it is shown that the output of a piezoelectric element is influenced by changes in temperature. This results in an increase in the slopes of susceptance and conductance. Both the degradation of a piezoelectric element and a bonding layer can occur when the temperature greatly increases, e.g. goes above 100°C or 130°C. This means that it is much easier to obtain a false damage detection alarm in an SHM system. However, by using the EMI method and feature extraction, as well as PCA in data analysis, the influence of temperature is avoided, and the degradation and defect of the bonded PIs are detected successfully.

In the future, the relevant classifications need to be investigated so that the different kinds of damage that occurs in bonded piezoelectric elements or in the bonding layer can be identified. The behaviour of the admittances of a bonded piezoelectric element should be investigated at lower temperatures (0°C, -30°C, -50°C etc).

5 Investigation of the Sensing Ability of Bonded Piezoelectric Elements

Over the last decade the use of piezoelectric elements in SHM has been thoroughly explored. As a result piezoelectric elements are now the enabling technology and key components in many SHM systems used for damage detection. Piezoelectric elements possess high rigidity, are used in a high natural frequency, and provide an extremely wide range of measurement. They are also very stable. Possessing these advantages, piezoelectric elements have been successfully applied in SHM systems using the EMI technique where they work as self-sensing actuators/sensors.

One of the important advantages of piezoelectric elements is their actuation ability. In other words, the extent of their range detection and the properties inherent in the structural system under investigation which influence their ability to operate efficiently.

This chapter discusses the sensing ability of bonded piezoelectric elements using the EMI technique in both numerical and experimental methods. In [Takewaki, 2012], the identification for SHM is introduced using numerical model and experimental method.

Using the numerical method, the model by SEM is used to calculate the spectra of EMIs. In this way, the factors that influence the sensing ability of piezoelectric elements are discovered. In addition, the wave propagations simulated by SEM give an idea of their variance when higher or lower damping is applied to the structural model. The simulations of propagating waves are shown in several figures.

Using the experimental EMI method, numerical results can be verified and validated by real measurements. Additionally, these measurements are taken using different input signals and in different damage locations. Afterwards, DMs based upon varying input signals, angles or distances are compared. In this way, the sensing ability of the bonded piezoelectric element are established.

5.1 Numerical Investigation– SEM Combined with EMI Method

The E/M admittance model using two-dimensional polar coordinates was presented in [Zagrai 2002]. This model with a bonding layer and two degrees of freedom was also presented in [Xu 2002] and [Bhalla 2004]. Furthermore, [Lalande 1997] described an impedance-based model with finite element analysis using a piezoelectric element bonded to a shell structure. [Park 2000] presented an analysis of SHM by combining the impedance based method with the spectral finite element method (SHM). However the version of SEM provided by PARK based on the exact solutions in the frequency domain for harmonic excitation. Because the exact solution are required, this method is only applicable to relatively simple structures, beams or rods. Here we use the time-domain SEM as described in section 2.4.

In order to set up efficient and suitable SHM systems, physics-based models are useful for a detailed understanding of wave propagation in the structures under analysis. This is shown in the investigation of the phased array, see Chapter 3.

As described in Chapter 2, because the EMI technique is implemented using high frequency excitation, the classical finite element method is not computationally efficient. The time domain SEM is a high-order finite element technique that combines the geometrical flexibility of finite elements with the high degree of accuracy of the spectral method. This is a discretization method used to obtain an approximate solution of partial-differential equations expressed in a weak form, and based on high-order Lagrangian interpolation and certain quadrature rules.

SEM has several computational properties, such as the use of tensor products and naturally diagonal mass matrices. These properties determine that SEM is an efficient method for higher frequency excitation.

In this section SEM is utilized not only to demonstrate the wave propagation in the structure under investigation, but also to research how the spectra of EMI are influenced by the parameters of structures and piezoelectric elements. Using this process, the sensing ability of a bonded piezoelectric element in the structure system is investigated. The simulation results are verified and validated by an experimental investigation in section 5.3.

Figure 5.1 shows the simulation of an aluminium plate, *200×400×1.5mm*, with PZTs bonded to the plate. This plate is divided into 98 spectral elements, with 36 nodes per element in this model. Two PZTs are in position 45 and 54 respectively. The distances to the edge of the plate are 85mm and 84mm respectively.

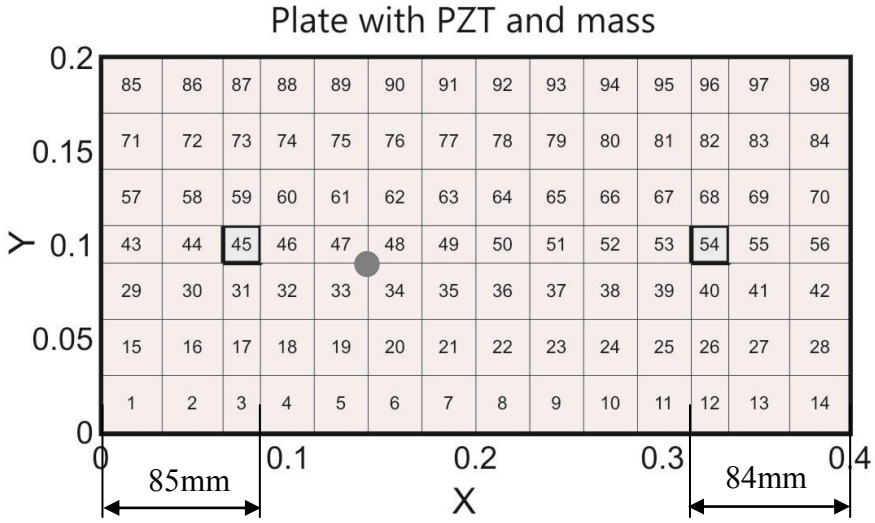

Figure 5.1 The SEM mesh of the aluminium plate

After the EMI spectrum was calculated in an undamaged state, two magnets (*10mm* diameter, *5mm* thick, weight *3.8g*) representing the structural change were positioned at the common node of elements 33, 34, 47, 48, is indicated by the gray dot in Figure 5.1.

Using the EMI technique, the bonded PZT is excited by applying an alternating voltage. The electrical field generates dynamical nodal forces and moments along the edges of the piezoelectric element, exciting the structure. In turn, this produces deformation. The modal displacements allows to calculate the strains. The strain response of this area is transferred back to the PZT in the form of output charges. Therefore, it may said that one PZT in the EMI method concurrently acts as both actuator and sensor. By using the output charges in simulation, electro-mechanical impedance (EMI), *Z*, can be calculated, see section 2.4. Any damage to the structure manifests itself as a deviation in the EMI spectrum, which serves as an indication of the damage. The spectra of real and imaginary parts of EMIs calculated with SEM are compared with the corresponding spectra of the experiments in 5.2.1.

The influence of mechanical and electrical parameters is discussed [Jiang L. 2010]. In this report, the proposed SEM model is utilized, see Section 2.4. The influence of different parameters on the sensing ability of a bonded piezoelectric element is represented as the spectra

of EMI (real part, imaginary part and their respective magnitudes). The damping and Young's modulus are investigated as important mechanical parameters.

In the above-mentioned report, damping is modelled using Rayleigh equations. The results show that the magnitudes of both real and imaginary parts are inversely proportional to the damping of the structure itself. The damping of a piezoelectric element causes a very slight effect on the EMI. In addition, when Young's modulus is increased, the stiffness increasing, the EMI spectrum shows a shift to the right side.

Therefore, it can be seen that the sensing ability of bonded piezoelectric elements depends on the properties of the structure. In the investigation of electrical parameters, resistance *R* and capacitor *C*, see Figure. 2.3, are analysed. The results show that the magnitude of the real part of EMI is increased, however, the magnitude of the imaginary part of EMI is decreased, along with the capacitance. These results, especially the analysis of mechanical parameters, proved to be beneficial in the following investigation.

5.2 Experimental Investigation

In the experiment, a rectangular aluminium plate is initially used, see Figure 5.2. The plate has the same size as that used in Figure 5.1. Two square piezoelectric elements, PIC151 [PI (Physik Instrumente) L. P.], made from lead zirconate-lead titanate piezoelectric ceramics (PZT), were bonded to the plate.

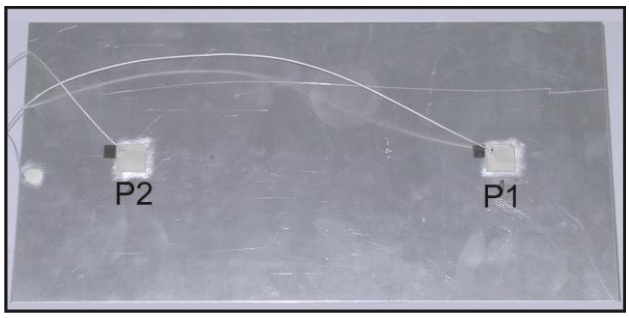

Figure 5.2 The aluminium plate in the experiment

In the EMI experiments, a wave from generator and an oscilloscope were applied to produce an input signal and to measure the outputs respectively, as mentioned in section 2.2.2. Damage was simulated by two small magnets, with a dimension of *10mm* diameter, and a thickness of *5mm* thick, *3.8g*, see Figure 5.3.

Figure 5.3 The magnet as damage

Three different types of measurements were taken at different input frequency ranges, the different angles of damage and the different distances between the PZT and the damage. The damage indicator results are shown and compared in section 5.2.2.

In addition to the experiment on the rectangular plate, there was also an experiment on a larger square aluminium plate (*400×400×1.5mm*), with a piezoelectric element in the middle of the plate, see Figure 5.4. The measurements were obtained using three different parameters described above. Comparisons of the damage indictors obtained are given in section 5.2.3.

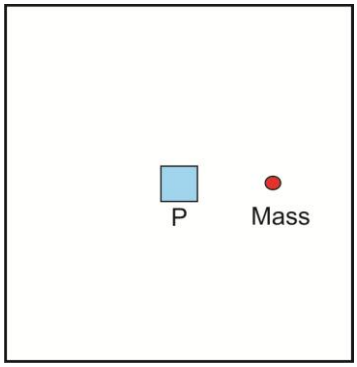

Figure 5.4 Schematic drawing of the larger square aluminium plate

5.2.1 EMI spectra comparisons between simulation and experiment

This section verifies whether the results of the numerical and experimental methods are accurate. The EMIs calculated by both the experimental method and by SEM are compared in the following figures.

Figure 5.5 shows the imaginary parts of EMIs, Imag(Z), calculated using experimentally and numerically methods. The blue-dashed spectrum is obtained by measurements, while the red-dashed spectrum by SEM simulation. These spectra show that the amplitudes of the blue-dashed spectrum are smaller than the red-dashed spectrum.

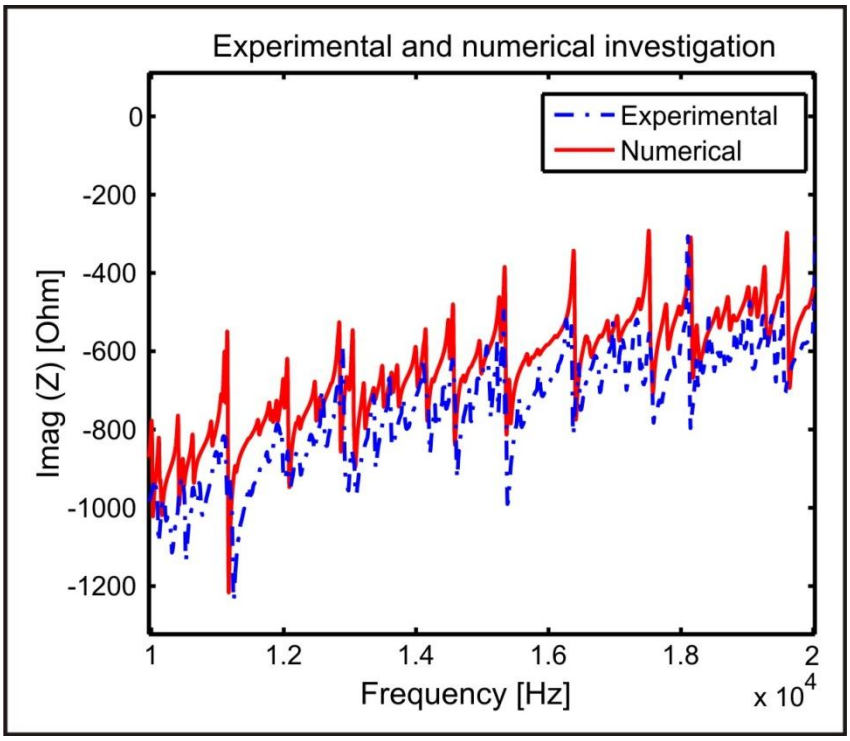

Figure 5.5 Imaginary parts of EMIs

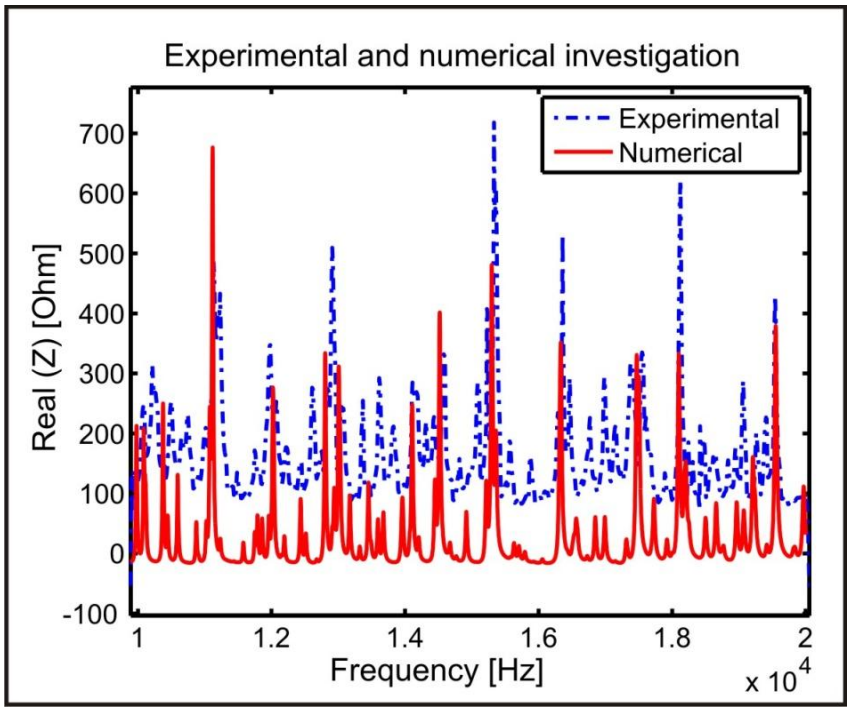

Figure 5.6 Real parts of impedances

Figure 5.6 shows the real part of EMIs, Real(Z). Contrary to Figure 5.5, the amplitudes in this experiment are larger than those in the numerical method. However, even though there are offsets in both Imag(Z) and Real(Z), the main peaks of spectra almost overlap. Overall, the EMI spectra in the experimental method correlate well with the spectra using SEM.

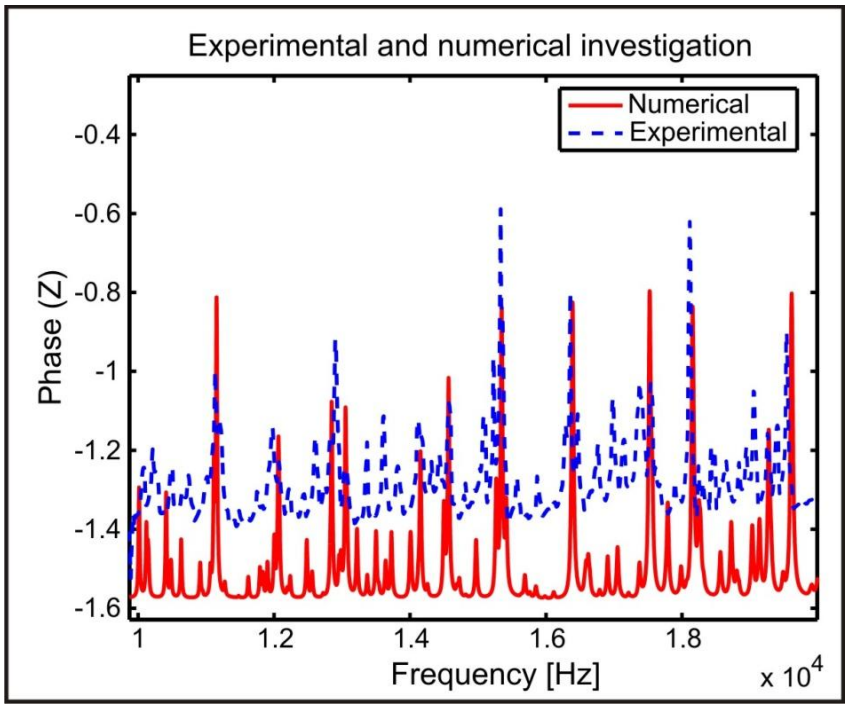

Figure 5.7 Phases of EMIs

Figure 5.7 is the phase angle of the EMIs in both the experimental method and SEM. There is a certain offset in the phase angle. The offset is more or less constant across the frequency range.

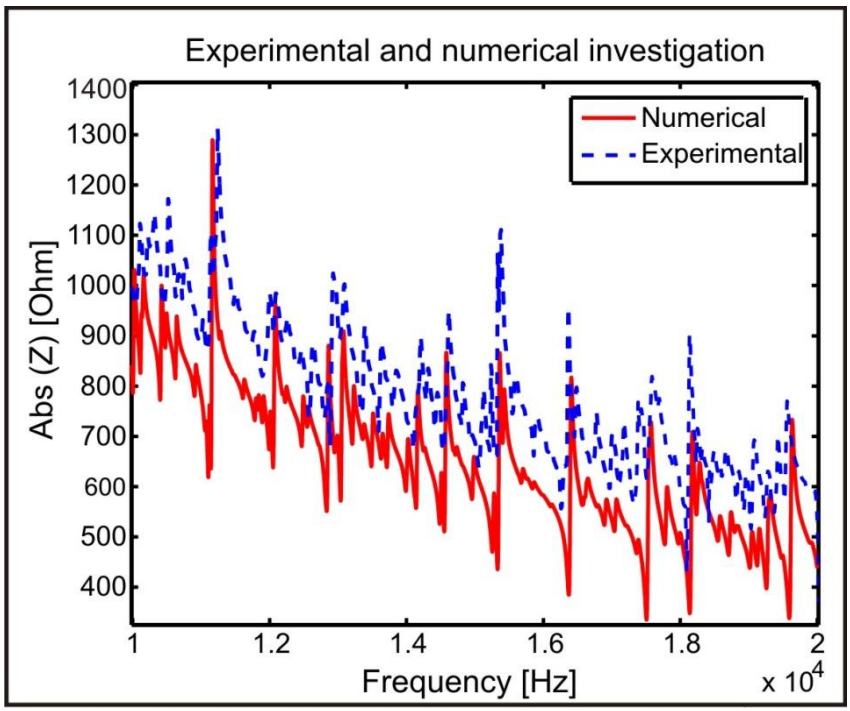

Figure 5.8 Absolute values of EMIs

Figure 5.8 shows the absolute values of the EMIs in both the experimental method and SEM. In a similar way to Figure 5.7, offset occurs. However, in both Figures 5.8 and 5.9, the main peaks correlate well.

In the four figures above, it indicates that the EMI results using the experimental method agree with the results calculated by SEM. These figures show that the SEM approach (see section 2.4) used to simulate the EMI correlates well with the real measurements in the experiment. Although the two curves do not coincide in every detail, we get a good overall agreement of the numerical and experimental results. Due to the nice properties of the SEM with the higher order approximation of the wave form, we get qualitatively good results in the high frequency range.

The reason for the offsets in the figures could be the bonding layer between the element and the plate, or if the model of the piezoelectric element includes inductance, [Arnau 2008].

One of SEM applications is to analyse the influence of the parameters of a bonded piezoelectric element and structures to the EMI spectra, [Jiang 2010] for example mechanical parameters: density, Young's modulus, and the thickness of the structure, as well as the damping, mass and stiffness of the piezoelectric element and plate. Electrical parameters include resistance and the capacitance in the electrical circuit of EMI, see Figure 2.3.

In the following experiments, masses were added to the plate to create a damaged state and the EMI is investigated. As mentioned in section 2.2, theoretically, an added mass changes its mechanical impedance, resulting in a spectrum shift in the real part of the EMI.

In this experiment, the comparisons of EMI in undamaged and damaged states are investigated experimentally and numerically. Figure 5.9 shows the spectra of the real part of the EMI, real(Z). The top figure is obtained by using the experimental method and the subplot is obtained by using the numerical method. In both figures, the blue spectrum is the real(Z) in an undamaged state, while the red spectrum is in a damaged state. These figures show that a spectral shift takes place after the damage has occurred. The shifts occur almost at the same frequency in both figures, e.g., at the frequency close to 11kHz, 14.5kHz, 15.5kHz and 18kHz, etc.

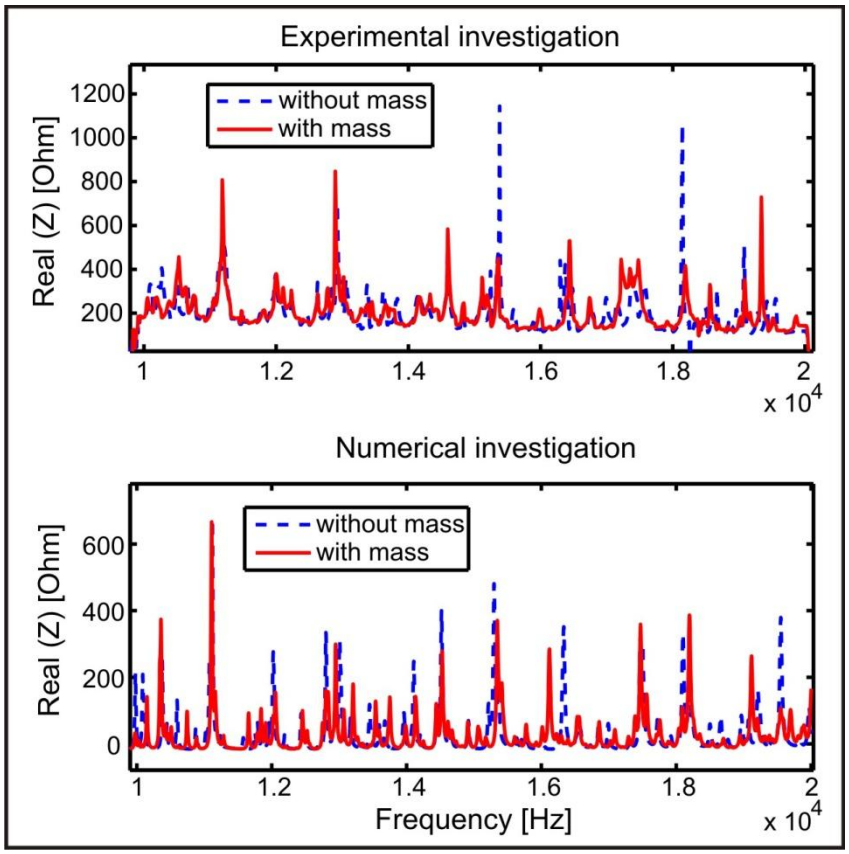

Figure 5.9 EMI with and without mass at position 47

In the EMI method, Damage metrics (DM) are used to examine the extent of the difference before and after damage occurs.

There are several definitions of DM, such as Mean Absolute Percent Deviation (MAPD), Root Mean Square Deviation (RMSD) method performed by [Park 2000] and [Peairs 2006]. Covariance Coefficient (CC) and the Difference Damage Metrics method are applied in Peairs' master thesis, [Peairs 2002]. These four DMs are described in detail in 2.2.3. The CC method is chosen to present the DMs in this work.

Figure 5.10 shows Damage Metrics (DMs) when the mass is located in two different positions (positions 47 and 51 respectively, see Figure 5.1). The yellow bars are calculated using the numerical method, SEM. The blue bars were obtained using the experimental method.

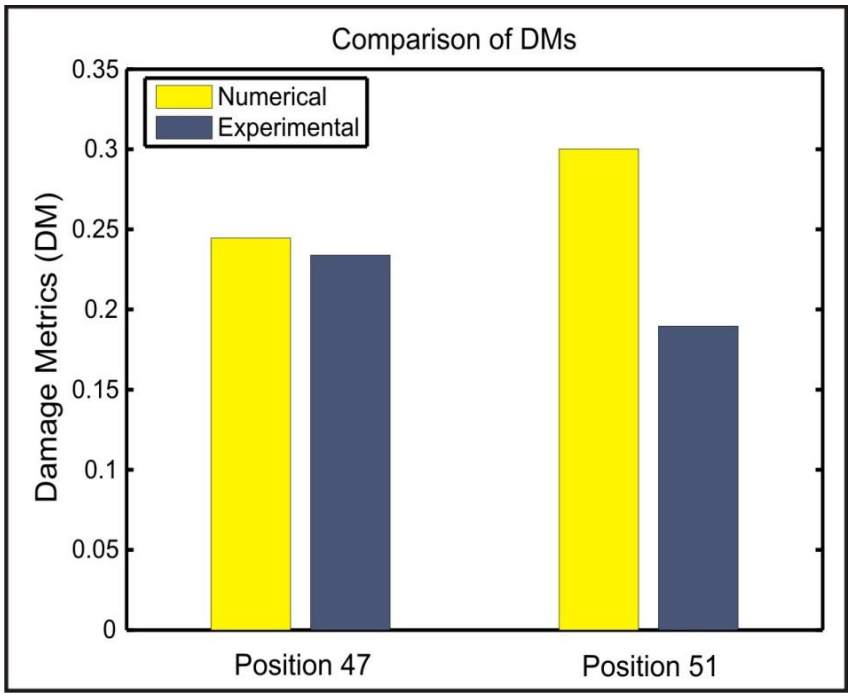

Figure 5.10 DMs by both methods, when the damage occurs at two different sites

When the mass is at position 47, the yellow bar is almost the same as the blue bar. When the mass is at position 51, there is only about 0.1 difference between the yellow and blue bars. In these examples, the extent of the damage is calculated both numerically and experimentally using EMIs. The consistency of these results illustrate once more that the SEM approach described above can be used successfully and has a large potential for more model-based applications of the EMI.

5.2.2 Experiments--- frequency and angle dependent

To investigate the sensitivity of the piezoelectric element bonded to the aluminium plate, the following experiments using varying input signal frequency ranges, differing distances and angles of damage location were carried out, see Figure 5.2 and Figure 5.11.

The measurements are obtained with input signals at 10-20kHz, 20-30kHz, 30-40kHz, 40-50kHz and 50-60kHz respectively. The mass is located at distances of 67mm, 125mm and 190mm to the bonded PZT. The mass is also put at different angles around the circle. The radius of the circle is 67mm, see Figure 5.12 and Figure 5.13.

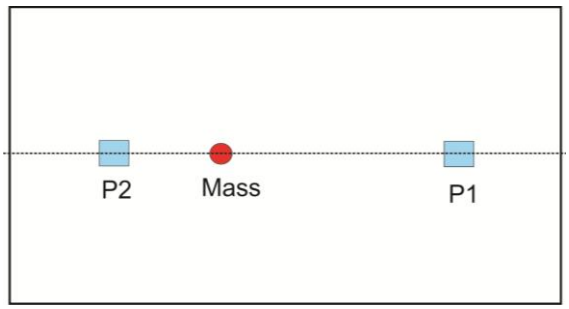

Figure 5.11 Schematic drawing of the plate

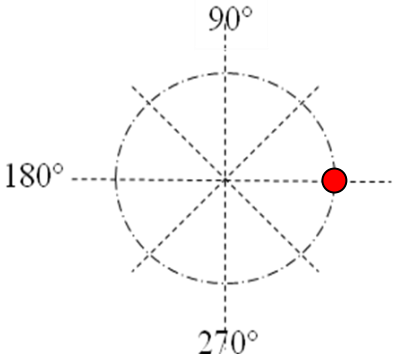

Figure 5.12 Different angles of the mass position

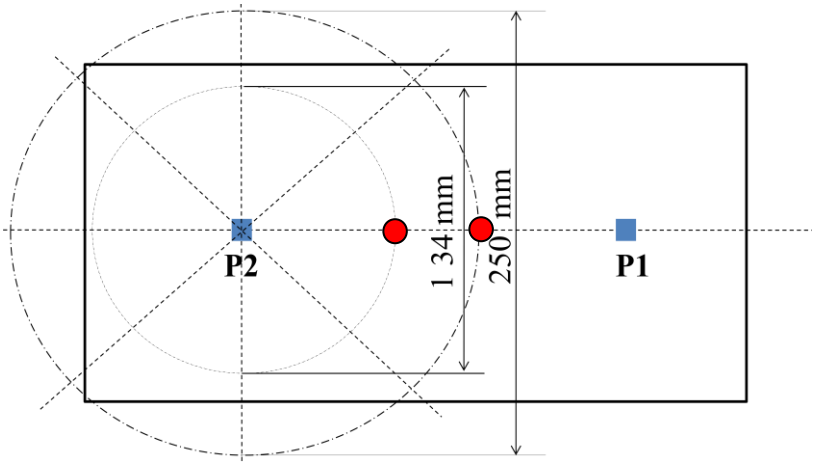

Figure 5.13 Mass locations around the radius of 67mm

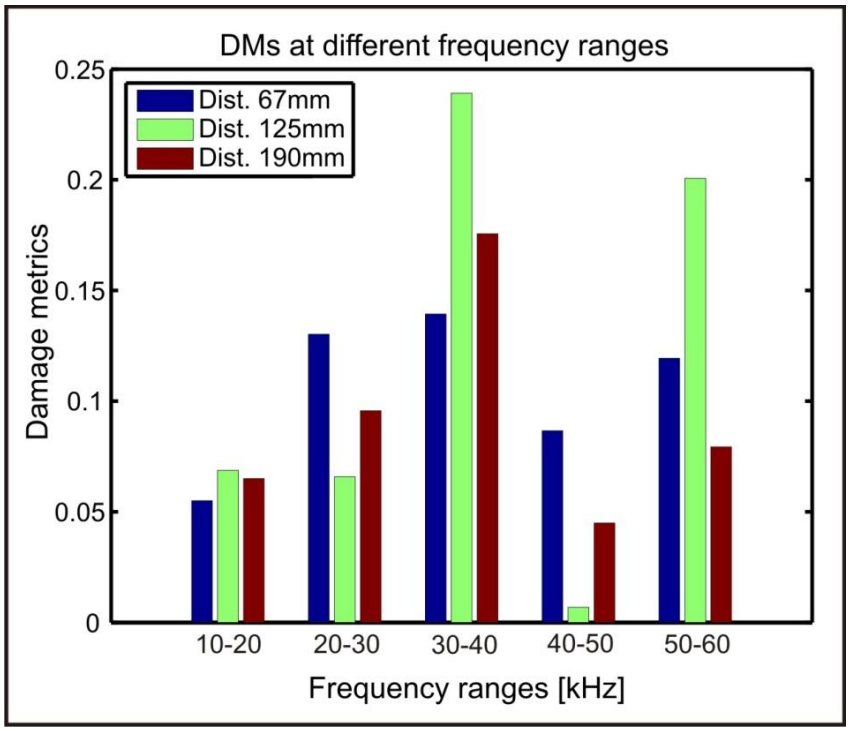

Figure 5.14 Damage metrics depending on the damage distances

In the DM bars shown in Figure 5.14, the different colours represent the DM values for different positions. These measurements, which show the greatest DMs, were taken when the frequency range of the input signals ranged from 30kHz to 40kHz, the DMs are the greatest.

When the frequency range was from 40kHz to 50kHz and from 50kHz to 60kHz, there were significant differences for the three distances. However, when the frequency range of the input signal was from 10 to 20 kHz, the values of the DMs changed evenly at the three different positions of the mass. Additionally, at none of the frequency ranges was there a clear sensing radius of bonded PZT shown in the plate.

Figure 5.15 shows the DMs when mass was at different angles around P2, as well as at different frequency ranges. The different colours represent the different frequency ranges of input signal. It illustrates that there is no regular pattern in the behaviour of a DM, even when the mass is located at symmetrical angles (for example: 45°, 135°, 225° and 315° etc). However, when the mass is at 90° and 270°, the DMs in the corresponding frequency ranges are almost symmetrical.

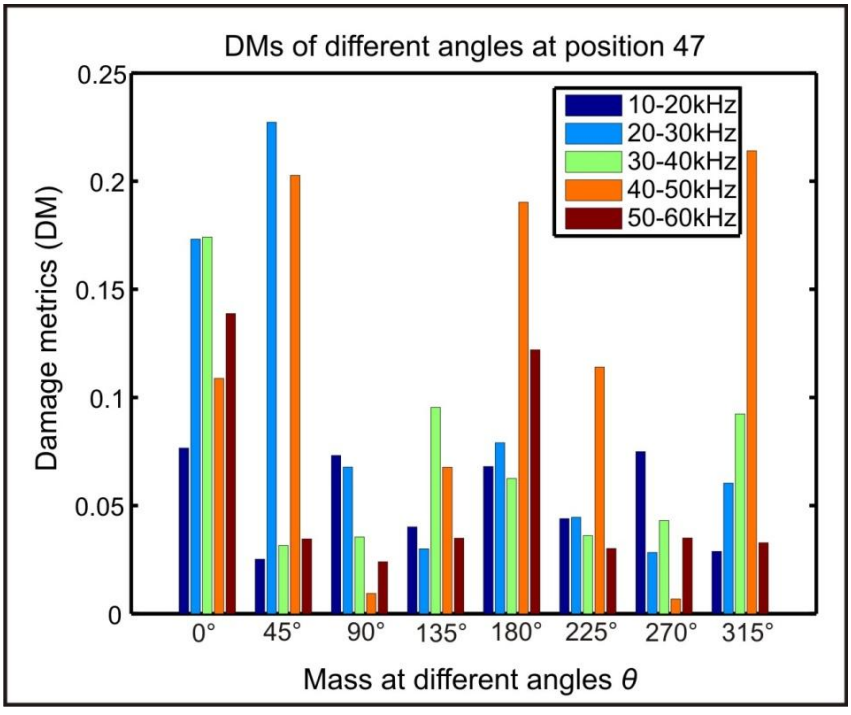

Figure 5.15 Damage metrics depending on different angles of damage in the smaller plate

The DMs in the two figures above indicate that there is no obvious sensing area of bonded PZT in the rectangular aluminium plate.

5.2.3 Results of the experiment on the larger square aluminium plate

In the larger square aluminium plate (1000mmx1000mmx2mm) experiment, see Figure 5.4, output data was collected when the mass was located at different angles and using different frequency ranges and input signals in a 100mm radius circle.

In Figure 5.16, the bars are the DM values when the mass is located at angles (0°, 45°, 90°, 135°, 180°, 225°, 270° and 315°). The different colours illustrate the different frequency ranges of the input signals. It appears that the DMs in the higher frequency ranges are smaller than the DMs in the lower frequency range.

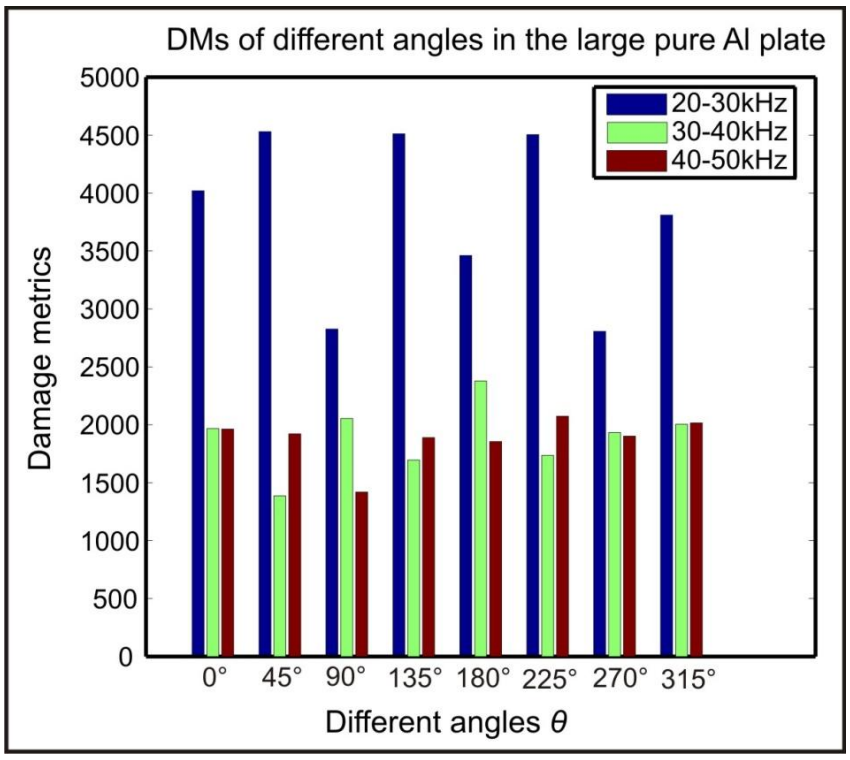

Figure 5.16 Damage metrics depending on different angles in the larger square plate

In Figure 5.17, the 16 bars represent the damage metrics when the mass is at different distances from the PZT. It shows that the DMs do not change gradually when the distance between the mass and the center of the plate is slowly increased.

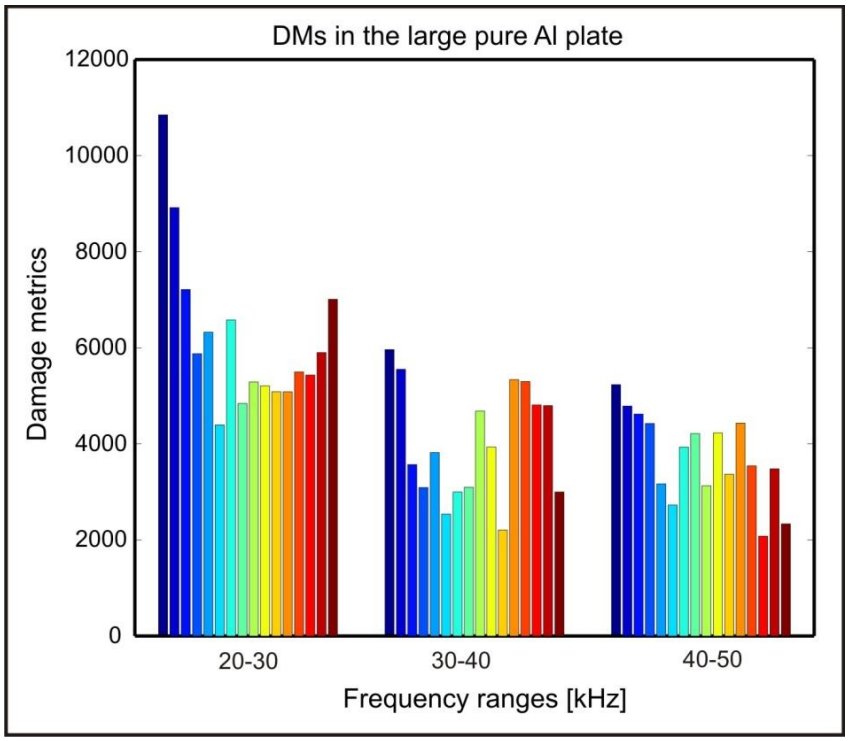

Figure 5.17 Damage metrics depending on the damage positions

To avoid noise influence, Figure 5.18 shows the DMs in both undamaged and damaged states. What we can clearly see is that the structural change caused by the mass results in a significant change of the damage indicator, so that this change can be definitely observed. The former DMs are relatively small when compared to the later ones. This means that noise has only negligible influence on the DM results.

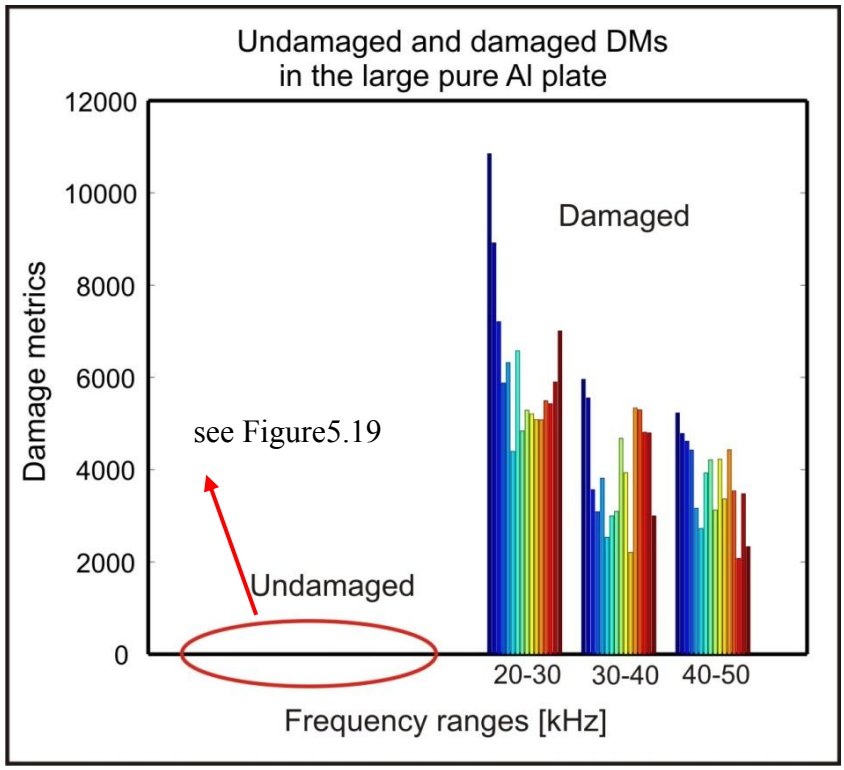

Figure 5.18 Comparison of DMs in undamaged and damaged states

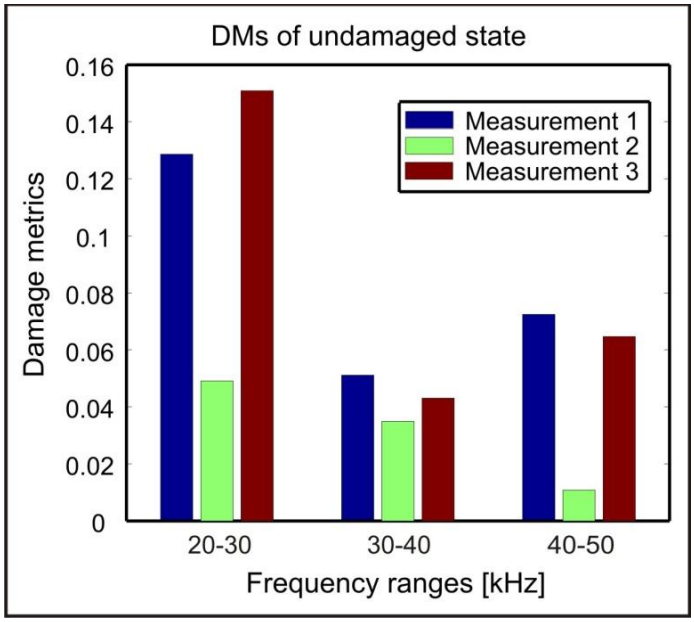

Figure 5.19 DMs of zoom

As can be seen in the experimental investigation above, the results do not indicate that the piezoelectric element bonded to the aluminium material has a clear sensing area. The sensing ability of the piezoelectric element appears uniform across the whole plate. It appears that the sensing ability of element which is bonded to the aluminium material does not depend on the location of the damage, especially the distance from the piezoelectric element.

When using simulation, the proposed SEM approach proves that EMI results obtained by SEM are consistent well with the results obtained using the experimental method, see Figure 5.5 and Figure 5.6. With the SEM we create simulated waves in the structure to investigate the parameters that have the most influence and EMI values. As shown in section 5.1, structural damping more strongly affects the sensing radius of a bonded piezoelectric element than any other parameter.

The plate shown in Figure 5.4 is divided into spectral elements and using SEM, wave propagation is simulated with a harmonic input signal. The snapshots of propagating waves are shown in Figures 5.20 and 5.21.

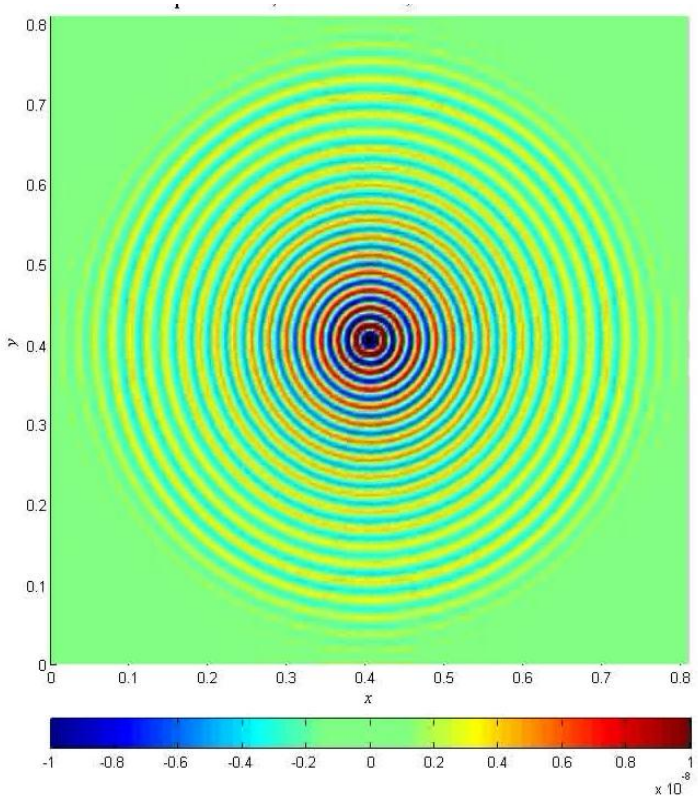

Figure 5.20 A snapshot of propagating waves in an aluminium plate with weak damping

Figure 5.20 shows the typical circular wave front in an isotropic plate. Because of the symmetrical form of the plate, waves that travel to the edges of plate, are reflected identically.

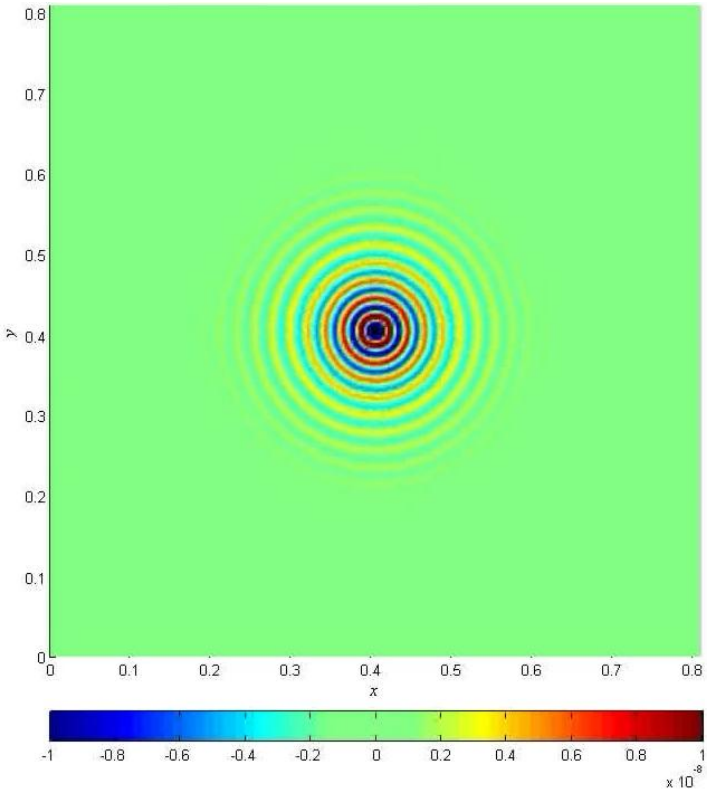

Figure 5.21 A snapshot of propagating waves in a plate with higher damping

However, when damping of the plate is increased in the simulation, the wave propagation changes, see Figure 5.21. Wave amplitudes are diminished gradually. This means that the energy is absorbed before the waves reach the edge of plate. This means that any structural change in the area, where the waves have strongly attenuated cannot be identified.

The effect of the attenuation tendency can be established using EMI in another experiment. Anti-drumming material was used to increase the damping of the plate, see Figure 5.22. The measurement process is the same as in previous experiments. Afterwards, DMs are calculated and compared.

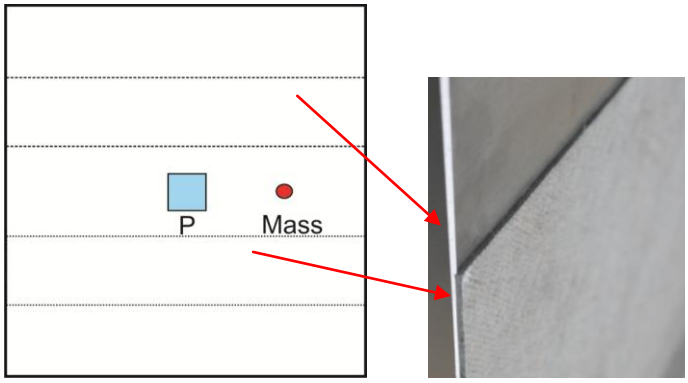

Figure 5.22 The aluminium plate with anti-drumming material

Figure 5.23 shows the DMs when the mass is at 15 different distances ranging from 2cm to 16cm from the PZT and the input signals are in different ranges. The differently coloured bars represent the DM values at different input signals with different frequency ranges of the sweep.

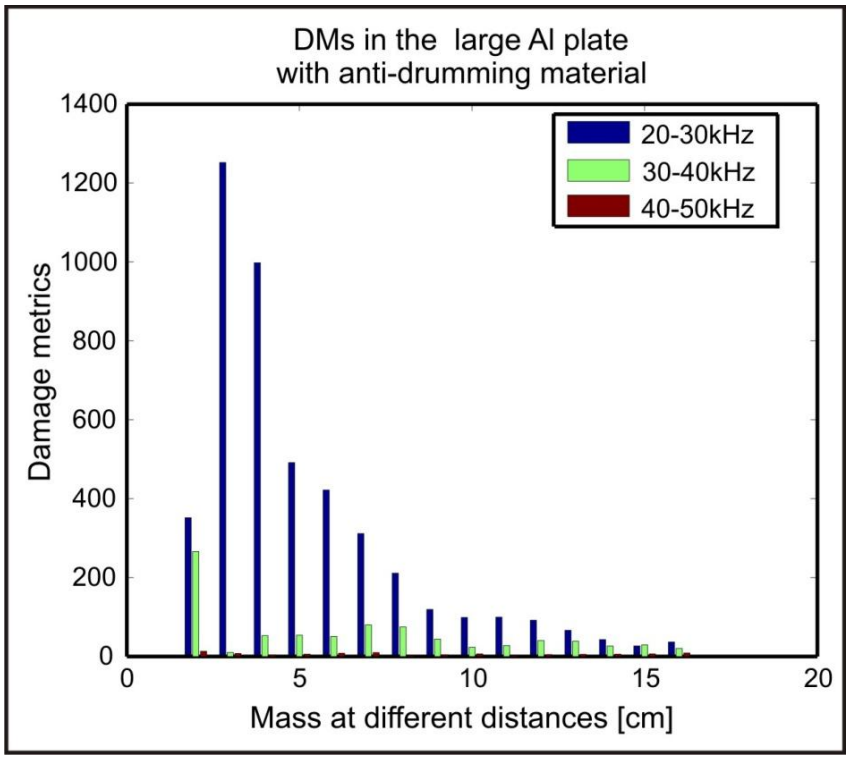

Figure 5.23 DMs depending on distances of the mass in the plate with higher damping

It can be seen that the DMs become gradually smaller when the mass is further away from the PZT, especially in the 20 to 30kHz frequency range. This means that the sensing ability of the PZT is inversely proportional to the distance between the mass (damage) and PZT within an area of 7cm. This finding coincides with the simulation of wave propagation, see Figure 5.21. However, for the input signals in 30-40kHz and 40-50kHz ranges, it seems that there is no clear inverse proportional relationship between the distance and the sensing ability.

The comparisons of the results between simulation by SEM and real measurement data in the experiment show a good correlation. This proves that the SEM model can be very useful in the investigation of the EMI method. In addition, wave propagation in the structure under investigation is simulated by SEM. This shows how the parameters in the structure system influence the sensing ability of bonded piezoelectric elements. The results show the different wave propagations in the different structure systems. Therefore, with a numerical tool such as SEM, the efficiency of the EMI method can be improved in respect of where to locate the bonded piezoelectric elements.

In the experiments, it was demonstrated that the sensing ability of a bonded piezoelectric element is influenced both by the damping of the structure and the input signal. Figures 5.16, 5.17 and 5.23 show that damage metrics do not fluctuate a great deal even when the location

of damage is changed, when the frequency is in the 40kHz to 50kHz range. There is no significant decay of the DMs when the damage is located further from the bonded element. The reason for this is most likely the fact that the modes for both structure systems (the small rectangular plate and the larger square aluminium plate) are global. These experimental results illustrate that for aluminium, the sensing ability of a bonded piezoelectric element is almost identical throughout the whole structure due to the low damping and reflection. However, when damping is increased, the sensing radius can clearly be seen in wave propagation simulation using SEM, and the bar figures for the DMs gradually decrease.

In conclusion, the proposed methodology, that is SEM combined with EMI, was applied and its effectiveness verified. By using this process it is possible to obtain a better understanding of the wave propagation phenomena in a structure and to investigate the sensing ability of bonded piezoelectric elements. As described in 5.1, the mechanical and electrical parameters in a structure system influence the sensing ability. Within these parameters, damping was investigated using both simulation and experimentation.

In simulation by SEM, wave propagation in the weakly damped aluminium plate showed the same propagation throughout the entire structure. However, wave propagation in material with a higher damping showed a clear attenuation. Under experimental conditions, the DMs calculated by EMI gradually decreased in the structure with higher damping when the distance between the damage and the bonded piezoelectric element was gradually increased. DMs were not greatly influenced by distance in the aluminium plate.

In the future, the sensing ability of piezoelectric elements bonded to composite structures should be investigated by SEM combined with the EMI method. Understanding the sensing ability helps significantly with the distribution of piezoelectric elements in structures made from different materials.

6 EMI Method Applied in Monitoring Fatigue Crack

It has been estimated that 90% of metal component failures are caused by fatigue. Aircraft are particularly susceptible to this type of damage. In large commercial aircraft, periodic inspections frequently reveal cracks, sometimes several in number. Automobile parts such as axles, transmission parts, and suspension systems may also fail due to fatigue, [Staszewski 2003]. The study of fracture cracks is of major importance in engineering because cracks occur with considerable frequency. Material fatigue is a consequence of a time-dependent stress-strain loading spectrum. In fracture mechanics three variables are used to predict the life span of components which are subject to the time-dependent crack growth mechanism. These are useful in evaluating material and the design of structures, as well as in failure analysis.

Fatigue cracks can occur at stresses below the material's yield strength, in other words where failure would not normally be expected. A fatigue failure is one that occurs under cyclic or alternating stress of an amplitude that would not cause failure if applied only once. One of the most critical tasks in fatigue analysis is to reliably identify the initial crack. The analysis and prediction of fatigue crack growth has assumed major importance for large engineered items, especially where safety is paramount, such as for commercial aircraft and components in nuclear power plants. Periodic inspections are commonly performed on large aircraft in order to prevent cracks growing to a dangerous size, [Dowling 1993]. Recently fatigue crack detection is presented by using strain sensors in [Yao 2014] and this technologies based on large area electronics are presented for crack detection and localization, see [Yao 2015].

In this part, fatigue experiments are performed in order to monitor the crack growth in a vibrating aluminium plate to which piezoelectric elements have been bonded. The plate is excited by a shaker and vibrates continuously until cracks appear. The outputs of the bonded piezoelectric elements are measured at different times. Damage Metrics are compared to determine if and when fatigue cracks occur.

6.1 Experimental Set-up

As shown in Figure 6.1, the object in the experiment was an aluminium plate with dimension 400mm x 300mm x 3mm. One side of the plate was inserted into an electromagnetic shaker, while the other side was free. There were 6 PZTs and 2 strain gauges bonded to the plate. The 6 PZTs were P1, P2, P3, P4, P5 and P6 respectively. They were used in the EMI circuit, see

Figure 2.3, to collect the dynamic and static outputs. The strain gauges were used to monitor stress and strain across the entire plate. In addition, there were three holes (10mm diameter) through the plate (close to the shaker). The crack was expected to start at the edge of the holes due to stress concentration. The two strain gauges were close to the hole in the middle of the plate where the largest stress occurs during the plate vibration. The shaker excites the plate at a frequency of 17.6 Hz which is close to the first natural bending frequency of the plate.

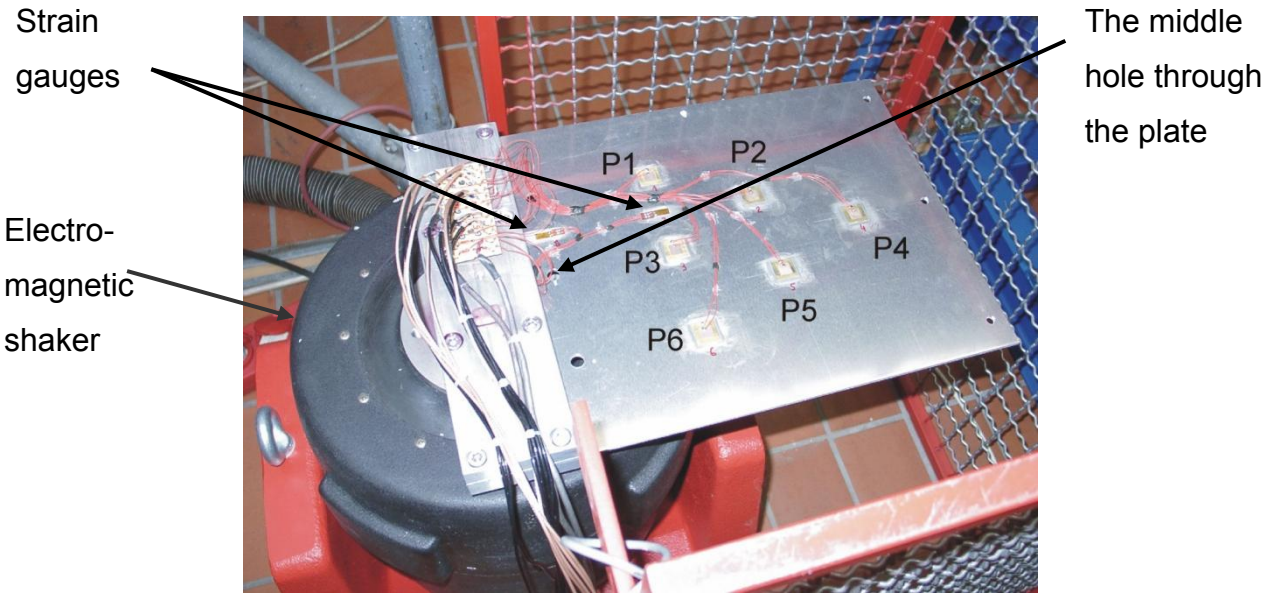

Figure 6.1 LDS electromagnetic shaker and plate

To accurately detect the crack propagation in the plate, the crack propagation gauges RDS20 produced by HBM can be chosen as well, see Figure 6.2.

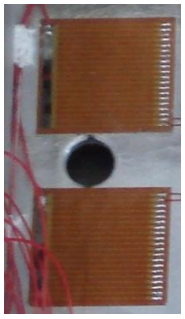

Figure 6.2 Crack propagation gauges bonded to the plate

RDS20 consists of separate electric resistors through which an individual circuit is broken when the crack grows and cuts the wire. When a crack has a certain length, plate vibration stops automatically. Therefore, in a fatigue experiment with crack propagation sensors, the data can be collected at the exact moment when changes in the plate occur. Figure 6.3 shows a

schematic of RDS20 bonded to the plate. The red line is the cracks growing on both sides of the hole.

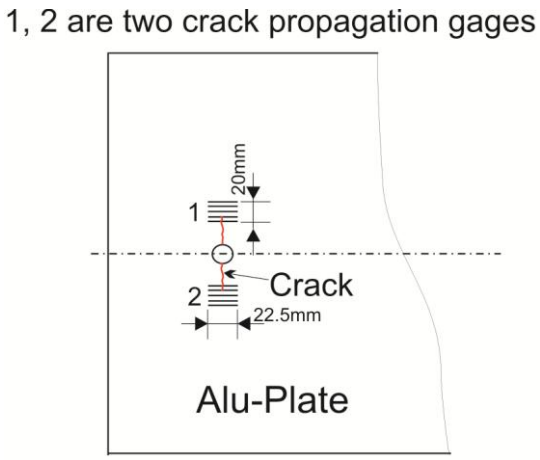

Figure 6.3 Schematic of crack propagation gauges

DIAdem is a Data Acquisition (DAQ) software for managing, analyzing and reporting data collected during data acquisition. It can also be used for data visualization. In our fatigue experiments, DIAdem was utilized to monitor the stress and strain on strain gauges. The current number of counter cycles of the vibrating plate is shown in the interface of DIAdem.

If there are crack sensors, MGCplus made by HBM is needed to monitor and control these crack sensors. When the crack appears or extends through the sensors, MGCplus Assistant controls the wave generator through a PC to automatically switch off the shaker.

In the experiment, the 6 PZTs were excited by 10 second sine sweep signals at 10 to 20 kHz, 5V amplitude. The output signals were then collected and shown on the oscilloscope, see Figure 6.4.

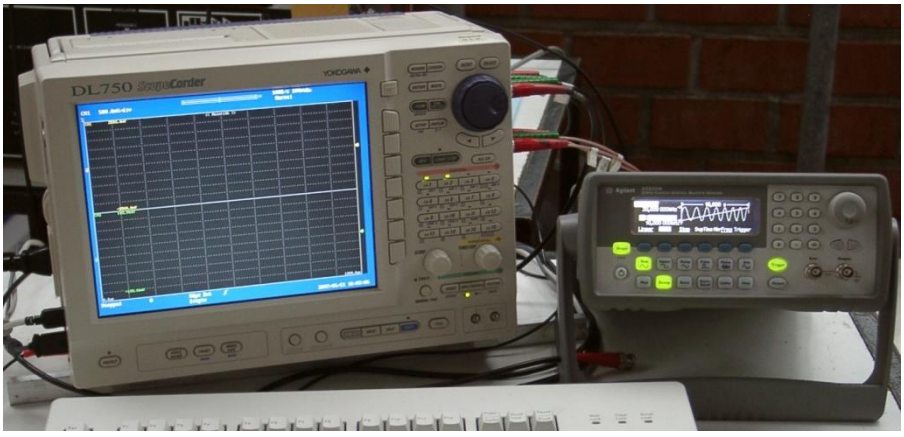

Figure 6.4 Wave generator and oscilloscope

6.2 Experimental Results

Two fatigue experiments were performed in this part of investigation. One was carried out without crack sensors bonded to the plate, the other with crack sensors. During both fatigue experiments, data was measured in static and dynamic states respectively. In the static state, measurements were taken when the shaker was switched off at regular time intervals. The time intervals were reduced before the beginning of each crack was detected, in order to identify exactly when the crack first occurred. After the cracks appeared, the time intervals were extended. In the dynamic state, the measurements were made during the vibration phase with the same time intervals as in the static measurements experiment.

The data measured in both dynamic and static states was utilized in the EMI method to obtain Damage Metrics, see Eq. 2.14. The results of experiments without crack sensors are shown in Figures 6.5 and 6.6.

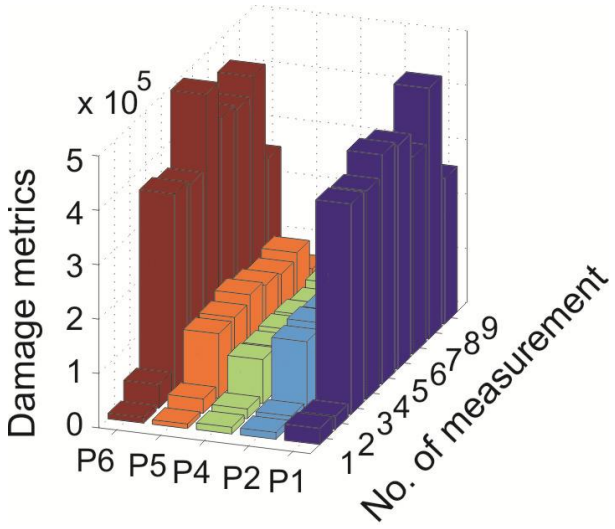

Figure 6.5 *DMs* calculated with dynamic measurements

Figure 6.5 shows the results of dynamic measurements. The number of measurements, from 1 to 9, describes the different DMs at different time intervals. They indicate that the DMs of P1 and P6, are much larger than those of P2, P4 and P5. The DM of P4 is the smallest. P3 became defective during the experiment. It seems that in the dynamic state, the PZTs closest to the cracks (P1 and P6, see Figure 6.1) are more sensitive than the PZTs placed further away (P2, P4 and P5). In addition, Figure 6.5 indicates that all the DMs started to increase from the third measurement, when the cracks on both side of the hole measured about 1.5 mm in length.

As mentioned at the beginning of this section, after the cracks are monitored, the frequency of vibration of the shaker is decreased in order to make the crack grow slowly. Between the third and the ninth vibration phase the cracks grew from 1.5 mm to 13mm.

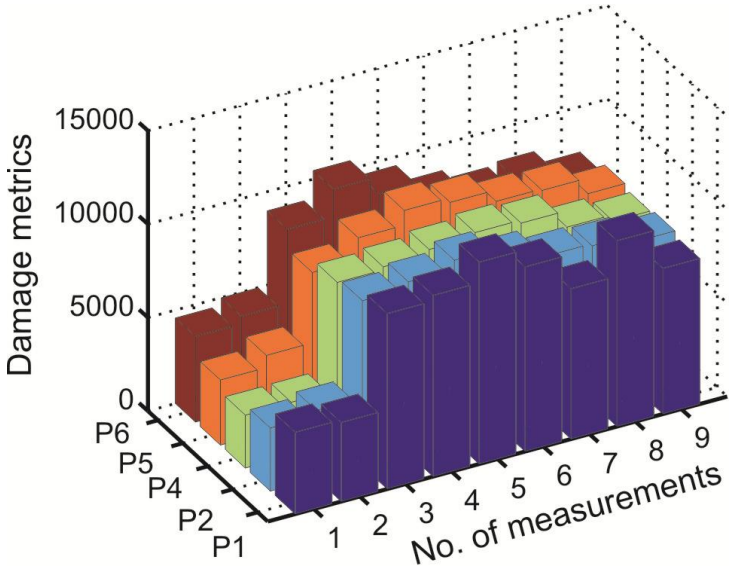

Figure 6.6 *DMs* calculated with static measurements

Figure 6.6 are the DMs calculated from the static data. The data are measured using the same time intervals when taking dynamic measurements. The figure indicates that the DMs begin to increase from the third measurement. However, there is not a marked difference among the DMs of the different PZTs. It seems that the DMs do not depend on the distance from the cracks to the PZTs. The DMs of P6 and P1 behave in the same way as P2, P4 and P5, which is consistent with the investigation of the sensing area of PZTs bonded to a pure aluminium plate as described in Chapter 5.

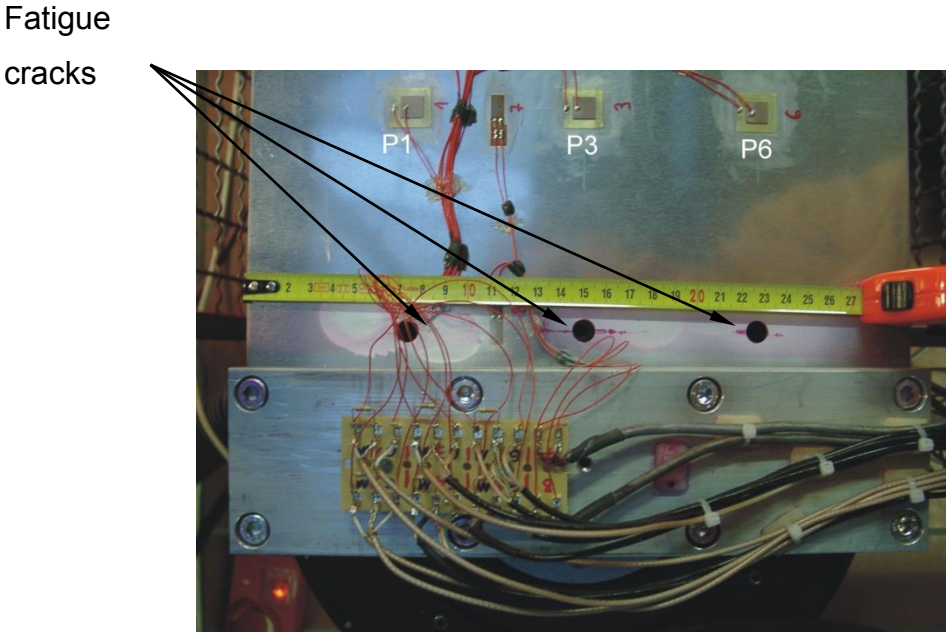

Figure 6.7 Fatigue cracks in the plate made visible using dye penetration

In the experiment without crack sensors, after about 130,000 cycles of vibration, crack could be monitored in the plate. The cracks can be seen on both sides of the middle hole, and are about 1.5mm long measured at the surface. The cracks were first observed during the third measurement. After over 300,000 cycles of vibration, the crack at the middle hole became 13mm in length. Cracks approximately 5mm long also occurred at the right hole, see Figure 6.7.

After the fatigue experiments the fatigue crack front in the cross section of the fractured plate is shown under a stereo microscope.

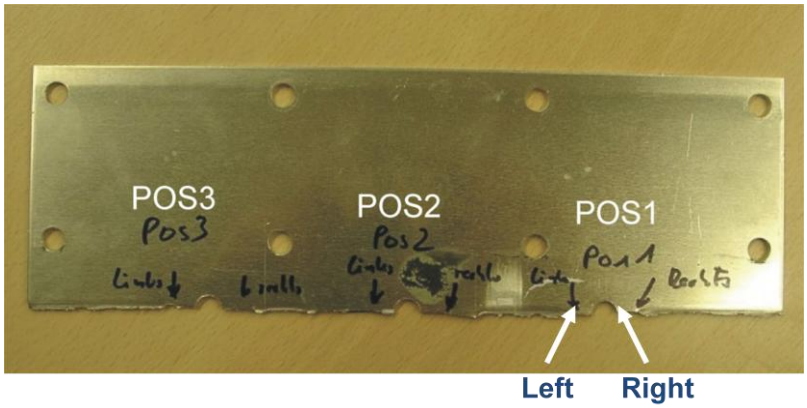

Figure 6.8 The fixed part of the plate after fracture

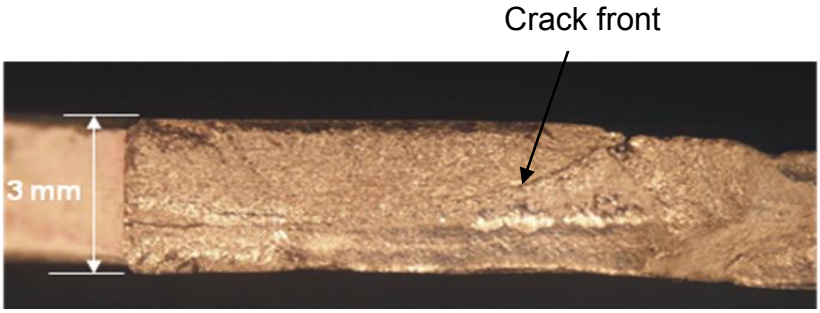

Figure 6.9 POS1 right

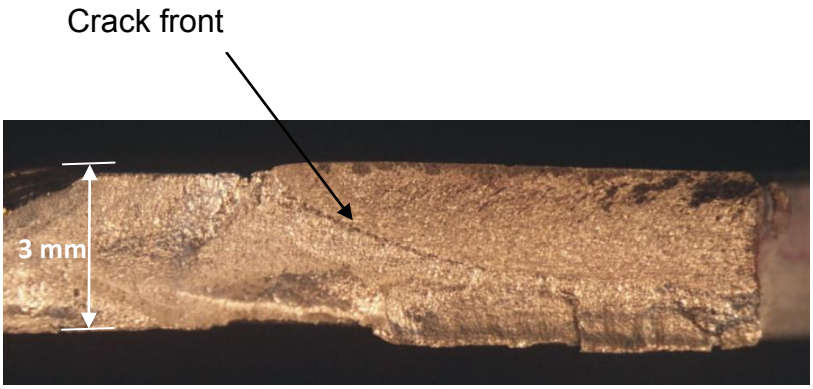

Figure 6.10 POS1 left

Figures 6.9 and 6.10 show the crack fronts on both sides of the right hole.

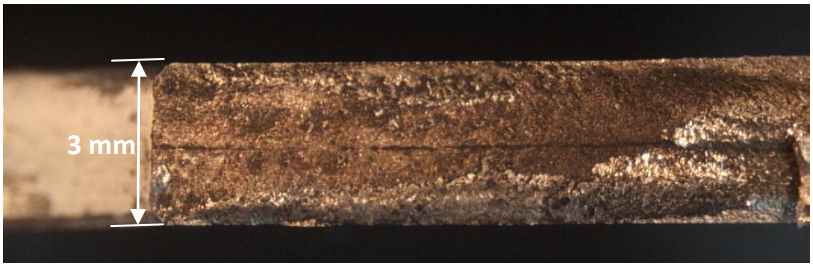

Figure 6.11 POS2 right

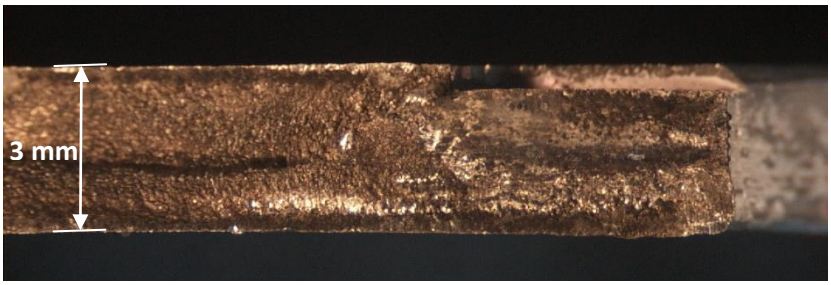

Figure 6.12 POS2 left

Figures 6.11 and 6.12 show the crack fronts on both sides of the middle hole. These cracks first appeared after the third measurement.

The DM results validate the proposition that the emergence of fatigue cracks can be monitored successfully using the EMI method. However, the results do not increase further as the cracks become larger during the fatigue experiment. The most probable reason can be that the strongest changes between two spectra of an undamaged and damaged system occur while the spectral peaks of the damaged spectra are shifting during the first phase of the damage evolution. Therefore, it is important to investigate further the sensitivity of EMI. A solution could be to store the history of the EMI spectra and compare the current spectra not only to the baseline but also the last spectra to observe the further growth of damage.

7 Conclusions and Discussion

This work investigates the process of damage detection using the EMI method, the Cross Transfer function method and SEM. The different applications of these three methods are described in detail.

The EMI method is used in investigations of sensing ability and the self-diagnosis of the bonded piezoelectric elements. Furthermore, experiments showed that the EMI provides a way of monitoring cracks during fatigue experiments. The Cross Transfer Function method has been used in the investigation of phased arrays in the frequency domain, sweeping through a defined spectrum. SEM has been used for the numerical analysis in this work.

The high degree of correlation between the results obtained from the experiments and simulations carried out as part of this research have confirmed that SEM can be regarded as a promising and effective tool in the investigation of the EMI method. SEM can also be used to define the experimental setup for SHM systems.

In Chapter 3, phased arrays, both a 1-D array and a T-array were investigated in the frequency domain using the Cross Transfer Function method. The results indicate that the direction of wave propagation can be controlled through beamforming, (the steering vectors in cross transfer functions). Damage indicators show a directional characteristic pointing out the direction of the damage location. With this method, damage could be successfully detected and located in the 1-D array under review. Furthermore, the beamforming results were even more encouraging in the case of the nonuniform array using Dolph-Chebyshev distribution. Not only does the direction of wave propagation coincide well with the real damage location but the main lobes are also more prominent. However, the beamforming with the T-array need further investigations.

The wave propagations are steered not only at the angle where the damage is located, but also in directions close to 180°. The wave propagation is not directional in T-array. In the future, other kinds of 2-D arrays can be investigated, also using Cross Transfer Function method. The size of the piezoelectric element or the distance between each element in the array can be adjusted to find the phased array that most accurately steers wave propagation.

An SHM system requires not only the ability to assess damage but also a high level of reliability. To avoid false alarms, SHM needs to start with a diagnosis of the piezoelectric elements bonded to the structure. In Chapter 4, the self-diagnosis of piezoelectric elements is implemented by the EMI method. The spectra of the E/M admittance at different temperatures show the influence of temperature on the properties of the bonded piezoelectric elements. Feature extraction and principal component analysis are applied in the self-diagnosis process thereby retaining the important information from current measured data, but environmental factors are not taken into account. Damage Indicators are further calculated and if the properties of the piezoelectric elements are affected, at the moment of change is shown above the threshold.

In section 4.2, breakage and degradation are executed in the experiments and the Damage Indicator results are shown for these cases. From the results obtained it can be seen that the breakage or degradation of the bonded piezoelectric element is detected by using E/M admittances in EMI method. During this process the changes of a piezoelectric element are distinguished successfully by changes of temperature. This shows that the EMI method can diagnose effectively the failures of bonded elements, removing the influence of changing temperatures.

The idea of self-diagnosis above is embedded into the software and applied in a device, called the PZT inspector, which has been used practically in an aircraft industry project. This device provides a convenient way of acquiring efficient and conveniently measurement data of the E/M admittance under service conditions. It detects and identifies different failure cases of piezoelectric elements under varying environmental conditions.

To set up an optimized experiment for a SHM system, the distribution of sensors/actuators bonded to the structure is of critical importance. For this reason, the sensing ability of one piezoelectric element needs to be taken into account.

In Chapter 5, the sensing ability of the bonded PZTs is investigated by using EMI experimental and simulation methods. As a result of this investigation, the following points are verified:

- The EMI spectra in experiments correlated well with the numerical method, the Spectral Element Method (SEM). This proves that SEM is an effective and promising simulation method.

- The mechanical and electrical parameters influencing the sensing ability are found by comparing EMI spectra calculated by SEM. Among these parameters, structural damping has the strongest influence on the spectra of EMI. This was shown in both experimental and simulation results.
- By defining damage metrics (DM) along with the EMI method, the sensing ability of one bonded PZT is investigated. The results show that DM values in experiments do not depend on the position (distances or angles) of the damage in a pure aluminium plate. However, in the experiments with a higher damped plate, the DM values gradually decrease, when the distance between the damage and the PZT increases. Furthermore, waves simulated by SEM propagate identically across the whole plane of the aluminium plate. However, the wave propagations attenuate in the plate with higher damping.

The conclusions above show that the EMI method can be used to significantly and successfully understand the sensing ability of one bonded piezoelectric element. It will assist greatly in determining the distribution of the piezoelectric elements on the structure.

Nowadays, in aircraft structures, carbon fiber reinforced polymer (CFRP) laminates are being used more and more because of their light weight design potential. However, the sensing ability of sensors bonded in composite laminates are different and more complicated than those in conventional metal alloys. In the future, damage detection in CFRP structures using the EMI method needs to be further investigated.

In this work, in addition to its effective application in the static structural system, the EMI method was also applied to dynamically loaded structures. Research in this area is limited. The DM results of the fatigue experiment in Chapter 6 validate the proposition that the emergence of fatigue cracks can be monitored successfully using the EMI method. However, the damage indicators do not increase further as the cracks become larger during the fatigue experiment and reach some saturation. The most probable reason is that the strongest changes between two spectra of an undamaged and damaged system occur while the spectral peaks of the damaged spectra are shifting during the first phase of the damage evolution. Therefore, an important area of future research is to investigate the sensitivity of EMI. A solution could be to store the history of the EMI spectra and compare the current spectra not only to the baseline but also the last spectra to observe the further growth of damage.

Over the last two decades, a large number of contributions have emphasized the application of the EMI method in the SHM process. However, investigations into the sensitivity of the E/M impedance method, which helps to identify the extent of damage, have not yet been presented. Consequently, the level of sensitivity of the EMI method to different types or sizes of damage is becoming an important topic of research.

References

Annamdas, V., GM (2013). "Electromechanical impedance of piezoelectric transducers for monitoring metallic and non-metallic structures." Journal of Intelligent Material Systems and Structures: 24(9)

Arnau, A. (2004). Piezoelectric Transducers and Applications, Springer: pp 4.

Ayres, J. W., Lalande, F., Chaudhry, Z. and Rogers, C.A. (1998). "Qualitative Impedance-based Health Monitoring of Civil Infrastructures." Smart Materials and Structures, **7**(5); Spinger: pp 599-605.

Balanis, C. A. (1982). Antenna Theory Analysis and Design, Wiley.

Balageas, D., Fritzen, C. -P. and Güemes, A. (2006). Structural Health Monitoring, Wiley.

Banks, H. T., Smith, R. C., Wang, Y. (1996). Modelling, Estimation and Control, Wiley.

Beral, B., Speckmann, H., (2003). "Structural Health Monitoring for Aircraft Structures: A Challenge for System Developers and Aircraft Manufactures", Structural Health Monitoring 2003, DEStech Publications: pp 12-29.

Bhalla, S. a. S., C. K. (2003). "Structural Impedance-based Damage Diagnosis by Piezo-Transducers." Earthquake Engineering and Structural Dynamics **32**(12), John Wiley & Sons, Ltd.: pp 1897-1916.

Bhalla, S. a. S., C. K. (2004). "Electromechanical Imepdance Modeling for Adhesively Bonded Piezo-transducers." Journal of Intelligent Material Systems and Structures **15**, SAGE Publications: pp 955-972.

Bohle, K. (2005). "Sensitivitätsbasierte Methoden zur Modellgestützten Schadendiagnose mit Modaldaten." Shaker.

Boychuk, A.S., Generalov, A.S., Stepanov, A.V. (2014). "CFRP Structural Health Monitoring by Ultrasonic Phased Array Technique." 7th European Workshop on Structural Health Monitoring, France. Inria, pp 2206-2211.

Cawley, P. (1984). "The Impedance Method of Non-Destructive Inspection." NDT International **17**, Elsevier: pp 59-65.

Chang, F. K. (1995). "Built-in Damage Diagnostics for Composite Structures" Proceedings of the 10th International Conference on Composite Structures, Woodhead Publishing: pp 283-289.

Dowling, N. E. (1993). Mechanical Behaviour of Materials: Engineering Methods for Deformation, Fracture and Fratigue, Prentice-Hall: pp 312, 536-540.

Dugnani, R. (2009). "Dynamic Behavior of Structure-mounted Disk-shape Piezoelectric Sensors Including the Adhesive Layer." Journal of Intelligent Material Systems and Structures **20**, SAGE Publications: pp 1553-1564.

Duda, R. O., Hart, P. E. and Stork, D. G., 2001: Pattern Classification, John Wiley& Sons. Inc.

Ehrendorfer, M. (1987). "A Regionalizaion of Austria's Precipitantion Climate Using Principal Component Analysis." International Journal of Climatology **7**, Royal Meteorological Society: pp 71-89.

Fritzen, C. -P., Kraemer, P., and Xing K. J. (2007), "Damage Detection and Localization Using Time Domain Residuals." World Forum on Smart Materials and Structures Technology, China, Taylor & Francis: p 77

Gandhi, M. V., Thomposon, B. S., (1992), Smart Materials and Structures, IOP Publishing: p 26.

Gautschi, G. (2002). Piezoelectric Sensorics, Springer: p 6.

Giurgiutiu, V., Rogers, C. A. (1997). Electro-mechanical Impedance Method for Structural Health Monitoring an Non-Destructive Evaluation. Proceedings of the International Workshop on Structrual Health Monitoring, Standford University, CA, DEStech: pp 433-444.

Giurgiutiu, V. a. Z., A.N. (2000). "Characterization of Piezoelectric Wafer Active Sensors." Journal of Intelligent Material Systems and Structures **11**(12), SAGE Publications: pp 959-976.

Giurgiutiu, V. and Bao, J., (2002). "Embedded Ultrasonic Structural Radar for the Nondestructive Evaluation of Thin-Wall Structures." Proceedings of the 2002 ASME, International Mechanical Engineering Congress, New Orleans, American Society of Mechanical Engineers: pp 17-22.

Giurgiutiu, V. a. B., J. J. (2004). "Embedded-ultrasonics Structural Radar for In-Situ Structural Health Monitoring of Thin-Wall Structures." Structural Health Monitoring **3**(2), SAGE Publications: pp 121-139.

Giurgiutiu, V. (2008). Structural Health Monitoring with Piezoelectric Wafer Active Sensors, Elsevier.

Gyekenyesi, A. L., Martin, R.E., Sawicki, J. T., Baaklini, G.Y. (2005). Damage Assessment of Aerospace Structural Components by Impedance Based Health Monitoring. NASA, Technical Memorandum, NASA Scientific and Technical Information (STI).

Hahn, H. G. (1992). Teschnische Mechanik, Springer: pp 80-81.

IEEE (1987). IEEE Standard on Piezoelectricity: p 10.

Ihn J. -B., Chang, F. -K. (2008). Structural Health Monitoring **7**(1), DEStech Publications: pp 5-19.

Jiang Luhua (2010). Studienarbeit Report.

Junior., V. L., Park, G., Cudney H.H. and Inman, D.J. (2000). "Impedance-based Structural Health Monitoring with Artificial Neural Networks." Journal of Intelligent Material Systems and Structures **11**, SAGE Publications: pp 206-214.

Köhler, B. -U., (2005). Konzepte der Statischen Signalverarbeitung, Springer.

Kraemer, P. and Fritzen, C. P., (2007). "Concept for Structural Damage Identification of Offshore Wind Energy Plants." Proceedings of the 6th International Workshop on Structural Health Monitoring, DEStech Publications.

Kudela, P., Zak, A., Krawczuk, M. and Ostachowicz, W. (2007). " Modelling of Wave Propagation in Composite Plates Using the Time Domain Spectral Element Method." Journal of Sound and Vibration **302**(4-5), Elsevier: pp 728-745.

Lalande, F., Chaudhry, Z., Rogers, C. A. (1997). "Impedance-based Modelling of Induced Strain Actuators Bonded on Ring Structures." Journal of Sound and Vibration **201**(2), Elsevier: pp 169-187.

Lamb, H., 1917: On Waves in an Elastic Plate. Proceeding of the Royal Society of London. Series A, Containing Papers of a Mathematical and Physical Character, **93**, Royal Society Publishing: pp114-128.

Lange, Y. V. (1978). "Characteristics of the Impedance Method of Inspection and of Impedance Inspection Transducers." Sov J NDT, : pp 958-966.

Lee, C. K. (1990). "Theory of Laminated Piezoelectric Plates for the Design of Distributed Sensors/Actuators. Part I: Governing Equations and Reciprocal Relationships." Journal of the Acoustical Society of America **87**(3), ASA Publications: pp 1144-1158.

Liang, C., Sun, F. P, Rogers, C.A. (1993a). "An Impedance Method for Dynamic Analysis of Active Material Systems." Proceedings, ASME 34th Structures, Structural Dynamics, and Materials (SDM) Conference, LaJolla, CA, : pp 3587-3599.

Liang, C., Sun, F. P, Rogers, C.A. (1993b). "Dynamic Output Characteristics of Piezoceramic Actuators." SPIE's 1993 North American Conference on Smart Structures and Materials.

Liang, C., Sun, F. P, Rogers, C.A. (1994). "Coupled Electro-Mechanical Analysis of Adaptive Material Systems-- Determination of the Actuator Power Consumption and System

Energy Transfer." Journal of Intelligent Material Systems and Structures **5**, Sage Publications: pp 12-20.

Liang, C., Sun, F. P., Rogers, C. A., (1996). "Electro-Mechanical Impedance Modeling of Active Material Systems." Smart Materials and Structures **5**, IOP Publishing: pp171-186.

Macherauch, E., Zoch, H.W. (1992). Praktikum in Werkstoffkunde, Vieweg+Teubner Verlag.

Malinowski, P., Wandowski, T., Trendafilova, I. and Ostachowicz, W. (2007). "Multi-phased Array for Damage Localisation." Key Engineering Materials **347**, Trans Tech Publications: pp 77-82.

Mengelkamp, G. (2006). Entwicklung Einer Intelligenten Struktur - Eine Kombination Globaler und Lokaler Verfahren zur Schadensdiagnose. Siegen, University of Siegen.

NDT (2001) "Fatigue crack growth rate properties." NDT Resource Center, Education Resources, NDT Course Material, Materials and Processes.

Ostermann, F. (2007). Anwendungstechnologie Aluminium, Springer: pp 15.

Ostachowicz, W. and Güemes, J. A. (2013). New Trends in Structural Health Monitoring, Springer.

Overly, T. G. S., Park G. and Farrar, C. R. (2007). "Development of Signal Processing Tools and Hardware for Piezoelectric Sensor Diagnostic Process." Proceeding of the SPIE **6530**, Sensor Systems and Networks.

Paris, P., Erdogan, F. (1963). "A critical analysis of crack propagation laws." Journal of Basic Engineering, ASME: pp 528-534.

Park, J., and Chang, F. K., (2003). "Built-in Detection of Impact Damage in Multi-Layered Thick Composite Structures" Proceedings of the 4th International Workshop on Structural Health Monitoring, DEStech Publications: pp 1391-1398.

Park, G., Cudney, H. H. and Inman, D.J. (2000). "An Integrated Health Monitoring Technique Using Structural Impedance Sensors." Journal of Intelligent Material Systems and Structures **11**, Sage Publications: pp 448-455.

Park, G., Cudney, H.H. and Inman, D.J. (2000). "Impedance-based Health Monitoring of Civil Structural Components." Journal of Infrastructure Systems **6**(4), ASCE: pp 153-160.

Park, G., Cudney, H.H. and Inman, D.J. (2001). "Feasibility of Using Imepdance-based Damage Assessment for Pipeline Structures." Earthquake Engineering and Structural Dynamics **30**(10), Wiley: pp 1463-1474.

Park, G., Farrar, C. R., di Scalea, F. L. and Coccia, S. (2006). "Performance Assessment and Validation of Piezoelectric Active-sensors in Structural Health Monitoring." Smart Materials and Structures **15**(6), IOP Publishing.

Park, G., Sohn, H., Farrar, C. R. and Inman, D.J. (2003). "Overview of Piezoelectric Impedance-Based Health Monitoring and Path Forward." The Shock and Vibration Digest **35**(6), IOS Press: pp 451-463.

Peairs, D. M. (2002). "Development of a Self-sensing and Self-healing Bolted Joint." Mechanical Engineering, Blacksburg, Virginia Polytechnic Institute and State University. **Master**.

Peairs, D. M. (2006). "High Frequency Modeling and Experimental Analysis for Implementaion of Impedance-based Structural Health Monitoring." Virginia Polystechnic Institute and State University, Blackburg. **Dissertation**.

Peairs, D. M., Inmann, D. J. and Park, G (2007). "Circuit Analysis of Impedance-based Health Monitoring of Beams Using Spectral Elements." Structural Health Monitoring **6**(1), Sage Publications: pp 81-94.

Patera, A. T. (1984). "A Spectral Element Method for Fluid Dynamics: Laminar Flow in a Channel Expansion." Journal of Computational Physics **54**(3), Elsevier: pp 468-488.

Rytter, A., (1993). "Vibrational Based Inspection of Civil Engineering Structures". Aalborg University. **Dissertation**.

Schulz, M. J., Sundaresan, M. J., Mcmichael, J., Clayton, D., Sadler, R. and Nagel, B. (2003). "Piezoelectric Materials at Elevated Temperature." Journal of Intelligent Material Systems and Structures **14**, Sage Publications: pp 693-705.

Schulte, T. R., Xing K. J. and Fritzen C. P. (2009). "Spectral Element Modelling of Wave Propagation and Impedance Based SHM Systems". Key Engineering Materials **413 - 414**, Trans Tech Publications: pp 683-690.

Schulte, T. R. (2010). "Modellierung Und Simulation von Wellenbasierten Structural Health Monitoring Systemen mit der Spektral-Elemente Methode". Siegen, Universität Siegen. **Dissertation**.

Sirohi, J. a. C., I. (2000). "Fundamental Behavior of Piezoceramic Sheet Actuators." Journal of Intelligent Material Systems and Structures **11**, Sage Publications: pp 47-61.

Staszewski, W., Boller, C., Tomlinson, G. (2003). Health Monitoring of Aerospace Structures, Wiley: pp 8, 130.

Stepinski, T., Uhl T. and Staszewski W.(2013). Chapter 6 Electromechanical Impedance Method. Advanced Structural Damage Detection, Wiley: pp141-173.

Sun, F. P., Chaudhry, Z., Liang, C. and Rogers, A. (1995). "Truss Structure Integrity Identification Using PZT Sensor-Actuator." Journal of Intelligent Material Systems and Structures **6**, Sage Publications: pp 134-139.

Takewaki, I., Nakamura, M. and Yoshitomi, S. (2012) System Identification for Structural Health Monitoring, WIT Press

Timoshenko, S., Young, D.H. and Weaver, W. (1928). Vibration Problems in Engineering, D.Van Nostrand Company INC: pp 408-420, 426.

Todoroki, A., Mizutani, Y., Suzuki, Y. and Haruyama, D. (2013). "Fatigue Damage Detection of CFRP Using the Electrical Resistance Change Method." International Journal of Aeronautical and Space Sciences, **14**(4), The Korean Society for Aeronautical & Space Sciences: pp 350-355.

Venu GM. Annamdas, (2013). "Electromechanical Impedance of Piezoelectric Transducers for monitoring metallic and non-metallic structures: A review of wired, wireless and energy harvesting methods." Journal of Intelligent Material Systems and Structures **24** (9), Sage Publications: pp 1021-1042.

Worden, K. and Dulieu-Barton, J. M., (2004). "An Overview of Intelligent Fault Detection in Systems and Structures." Structural Health Monitoring **3**, Sage Publications: pp 85-98

Xing, K. J. (2006). "Structural Health Monitoring with the Impedance Method." Siegen, University of Siegen. **Master**: p 123.

Xing, K. J. and Fritzen C. -P., (2007). " Structural Health Monitoring of Aircraft Components with the Impedance Method". World Forum on Smart Materials and Structures Technology, China, Taylor & Francis: pp160-164

Xing, K. J. and Fritzen C. -P. (2007). "Monitoring of Growing Fatigue Damage Using the E/M Impedance Method". Key Engineering Materials **347**, Trans Tech Publications: pp 153-158

Xing, K. J., Schulte, R. T. and Fritzen, C. -P. (2009). "Numerical and Experimental Investigation of the Sensing Area of Piezoelectric Elements for Damage Detection with the E/M Impedance Method." Key Engineering Materials **413-414**, Trans Tech Publications: pp 253-260.

Xu, Y. G., Liu, G. R. (2002). "A Modified Electro-mechanical Impedance Model of Piezoelectric Actuator sensors for Debonding Dectection of Composite Patches." Journal of Intelligent Material Systems and Structures **13**, Sage Publications: pp 389-396.

Yang, S. a. N., B. (1999). "General Sensor Equation and Actuator Equation for The Theory of Laminated Piezoelectric Plates." Smart Materials and Structures **8**, IOP Publications: pp 411-415.

Yao, Y., and Glisic, B. (2015). "Detection of Steel Fatigue Cracks with Strain Sensing Sheets Based on Large Area Electronics." Sensors **15** (4), MDPI AG: pp 8088-8108.

Yao, Y., Tung, S.T. and Glisic. B (2014). " Crack Detection and Characterization Techniques", Structural Control and Health Monitoring, **21** (12), Wiley: pp 1387- 1413.

Zagrai, A. N., Giurgiutiu, V. (2001). "Eletro-Mechanical Impedance Method for Crack Detection in Thin Plates." Journal of Intelligent Material Systems and Structures **12**, Sage Publications: pp 709-718.

Zhou, S., Liang, C. and Rogers, C. A. (1995). "Integration and Design of Piezoelectric Patch Actuators." Journal of Intelligent Material Systems and Structures **6**, Sage Publications: pp 125-132.